Maria Celeste Tirelli

Supervisor: Dr.hab Marco Costantini

MICROFLUIDIC–ASSISTED 3D PRINTING OF FUNCTIONALLY GRADED POROUS BIOMATERIALS

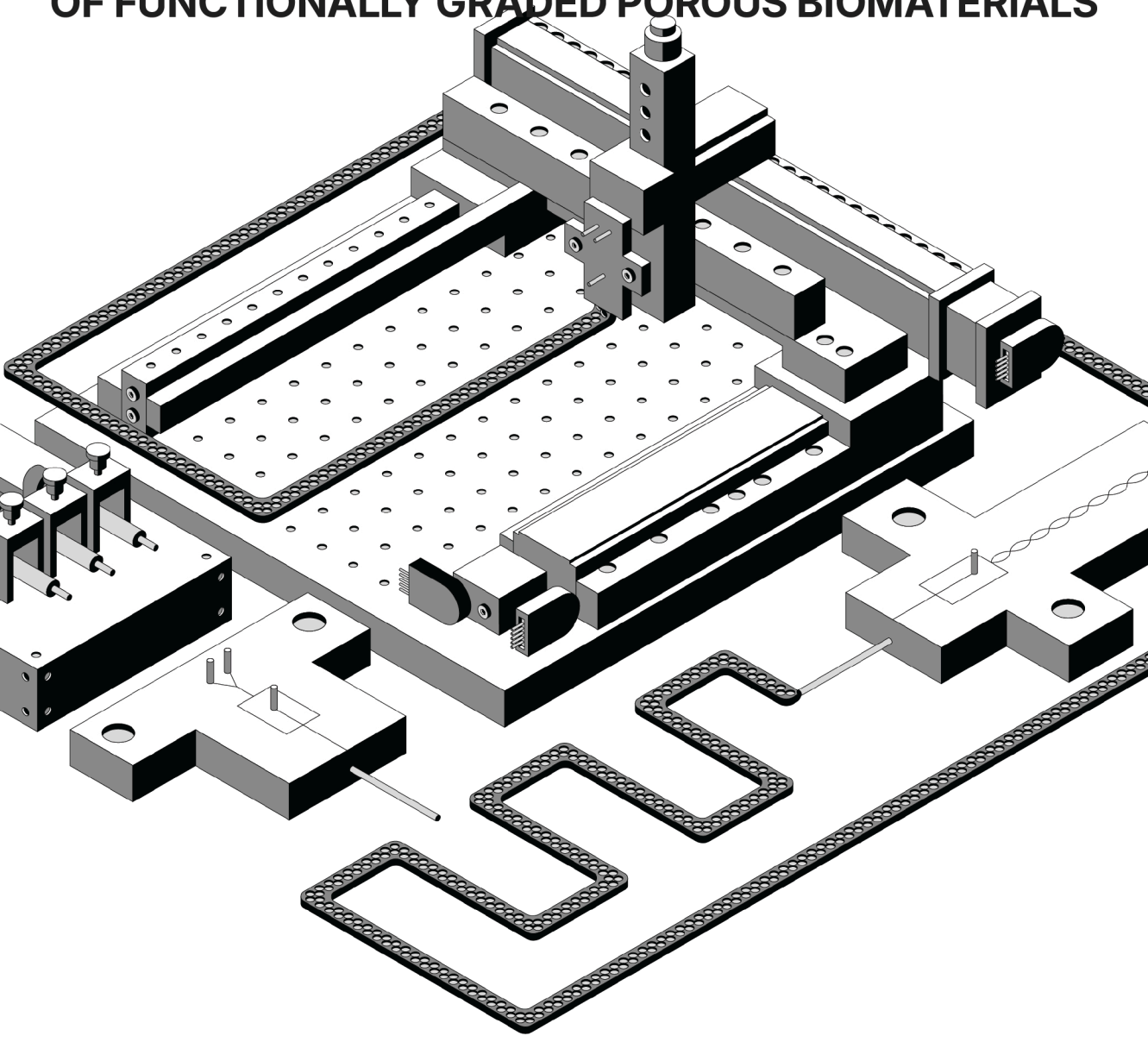

IChF
Institute of Physical Chemistry PAS

Ph.D. thesis within the Warsaw-4-PhD Doctoral School at the

Institute of Physical Chemistry
Polish Academy of Sciences

Kasprzaka 44/52, 01-224 Warsaw

Microfluidic-Assisted 3D Printing of Functionally Graded Porous Biomaterials

Supervisor:
Dr.hab Marco Costantini

Ph.D. Candidate:
M.Sc. Maria Celeste Tirelli

Warsaw, March 2026

Funding acknowledgment

This doctoral thesis was carried out within a project funded by the National Science Centre, Poland (NCN), under the OPUS 19 programme (project No. 2020/37/B/ST8/02167).

The research was conducted within the Warsaw PhD School in Natural and BioMedical Sciences (Warsaw-4-PhD Doctoral School) at the Institute of Physical Chemistry of the Polish Academy of Sciences.

List of publications

Publication related to the thesis:

1. Marcotulli M., Tirelli M.C., Volpi M., Jaroszewicz J., Scognamiglio C., Kasprzycki P., Karnowski K., Święszkowski W., Ruocco G., Costantini M., Cidonio G., Barbetta A. "Microfluidic 3D Printing of Emulsion Ink for Engineering Porous Functionally Graded Materials" **Adv Materials Technologies** 8, 2201244 (2023).
2. Tirelli M.C., Nalin F., Celikkin N., Górecka Ż., Posabella P., Święszkowski W., Costantini M. "Microfluidic-mixer assisted 3D printing of functionally graded multimaterial hydrogels for engineering complex tissue interfaces" **Mater. Adv.** 7, 2641–2651 (2026).

Other publications:

3. Weber P., Cai L., Aguilar Rojas F. J., Garciamendez-Mijares C. E., Tirelli M. C., Nalin F., Jaroszewicz J., Święszkowski W., Costantini M., Zhang Y. S., "Microfluidic Bubble-Generator Enables Digital Light Processing 3D Printing of Porous Structures" **Aggregate**, 00, e409 (2023).
4. Agarwal T., Chiesa I., Costantini M., Lopamarda A., Tirelli M.C., Borra O. P., Sai Varshapally S.V., Vijay Kumar Y.A., Koteswara Reddy G., De Maria C., Zhang L.G., Maiti T.K., "Chitosan and its derivatives in 3D/4D (bio) printing for tissue engineering and drug delivery applications" ***International Journal of Biological Macromolecules*** **246**, 125669 (2023).
5. Nalin F., Tirelli M.C., Garstecki P., Postek W., Costantini M., "Tuna-step: Tunable Parallelized Step Emulsification for the Generation of

Droplets with Dynamic Volume Control to 3D Print Functionally Graded Porous Materials" **Lab on a Chip** 10.1039.D3LC00658A (2024) doi:10.1039/D3LC00658A.

6. Serpe F., Nalin F., Tirelli M.C., Posabella P., Celikkin N., Jaroszewicz J., Swieszkowski W., Barbetta A., Senturk E., Casciola C.M., Ruocco G., Cidonio G., Scognamiglio C., Costantini M. "Microfluidic 3D Bioprinting of Foamed Fibers with Controlled Micromorphology" **ACS Appl. Mater. Interfaces** 17, 13632–13645 (2025).
7. Celikkin N., Tirelli M.C., Maiullari F., Gutiérrez Cisneros C., Kaushik V., Volpi M., Aerts A., Mohren R., Vandenbosch M., Cardinaels R.,Mignon A., Costantini M. "Methacrylated pulmonary dECM-enriched GelMA bioinks promote endothelialization and angiogenesis in 3D printed tubular constructs" **Mater. Adv.** 7, 2195–2206 (2026).

Other public presentation:

1. Biofabrication, September 2025, Warsaw, Poland. Oral presentation: Microfluidic-Assisted 3D Printing of Functionally Graded Ceramic Scaffolds for Bone Tissue Engineering."
2. World Biomaterial Congress 2024, May 2024, Daegu, Korea. Oral presentation: "Microfluidic-assisted digital manufacturing of functionally graded porous materials with transient physical and biological properties."
3. MicroTAS, October 2023, Katowice, Poland. Poster presentation: "Microfluidic-assisted digital manufacturing of functionally graded porous materials with transient physical and biological properties."

Abstract

Engineering spherical-based porous metamaterials in a cost-effective manner with controlled architecture across multiple length scales remains a central challenge in advanced additive manufacturing, including in biofabrication. Conventional scaffold fabrication methods typically rely on stochastic templating strategies that can only ensure limited control over pore size distribution, spatial organization, and compositional gradients, making it difficult to replicate the structural complexity of hierarchical biological materials. To overcome these limitations, this doctoral thesis presents a microfluidic-assisted 3D printing platform for the on-demand fabrication of porous functionally graded biomaterials.

A microfluidic flow-focusing droplet generator was designed to generate highly monodisperse emulsions that determine the resulting pore architecture. By precisely regulating the flow rates of the continuous and dispersed phases, droplet size was finely tuned, enabling controlled pore-size distributions in the resulting materials. Building on this concept, the droplet generator was integrated with an extrusion-based 3D printing system, allowing the direct deposition of emulsion-based inks into predefined architecture, enabling simultaneous control over macroscopic scaffold geometry and microscopic pore architecture while accommodating relatively low-viscosity material inks. Beyond hydrogel systems, the platform's versatility was further demonstrated by the fabrication of porous ceramic constructs via templated printing, followed by sintering, preserving the designed pore architecture. Finally, the system was expanded by integrating a passive microfluidic micromixer, which enables real-time modulation of the matrix composition during extrusion, enabling the fabrication of functionally graded soft biomaterials with spatially

controlled physicochemical and mechanical properties within a single printing process.

Together, these technological developments establish a microfluidic-integrated manufacturing strategy capable of programming porosity, composition, and architecture within a single fabrication workflow, enabling structural control from microscale pore templating to macroscale scaffold design and providing a scalable route to the fabrication of hierarchical, functionally graded porous materials for future biomedical applications.

Streszczenie

Inżynieria metamateriałów porowatych opartych na strukturach sferycznych, w sposób ekonomiczny oraz z kontrolowaną architekturą w wielu skalach długości, pozostaje jednym z głównych wyzwań w zaawansowanym wytwarzaniu addytywnym, w tym w biofabrykacji. Konwencjonalne metody wytwarzania rusztowań zazwyczaj opierają się na stochastycznych strategiach tworzenia szablonów, które zapewniają jedynie ograniczoną kontrolę nad rozkładem wielkości porów, organizacją przestrzenną oraz gradientami składu, co utrudnia odtworzenie złożonej struktury hierarchicznych materiałów biologicznych. Aby przezwyciężyć te ograniczenia, niniejsza rozprawa doktorska przedstawia platformę druku 3D wspomaganą mikrofluidyką do wytwarzania na żądanie porowatych biomateriałów funkcjonalnie gradientowych.

Zaprojektowano mikrofluidyczny generator kropli typu flow-focusing, zdolny do generowania wysoce monodyspersyjnych emulsji, które determinują powstającą architekturę porów. Poprzez precyzyjną regulację natężeń przepływu fazy ciągłej i rozproszonej wielkość kropli była dokładnie dostrajana, co umożliwiało kontrolę rozkładu wielkości porów w otrzymywanych materiałach. W oparciu o tę koncepcję generator kropli został zintegrowany z systemem druku 3D opartym na ekstruzji, umożliwiając bezpośrednie osadzanie tuszy emulsyjnych w zdefiniowanej architekturze oraz jednoczesną kontrolę makroskopowej geometrii rusztowania i mikroskopowej architektury porów, przy jednoczesnym umożliwieniu przetwarzania materiałów o stosunkowo niskiej lepkości. Poza systemami hydrożelowymi, wszechstronność platformy została dodatkowo wykazana poprzez wytwarzanie porowatych struktur ceramicznych metodą druku

templowanego, a następnie ich spiekania, z zachowaniem zaprojektowanej architektury porów. Na koniec system został rozszerzony poprzez integrację pasywnego mikrofluidycznego miksera, który umożliwia modulację składu matrycy w czasie rzeczywistym podczas ekstruzji, co pozwala na wytwarzanie miękkich biomateriałów funkcjonalnie gradientowych o przestrzennie kontrolowanych właściwościach fizykochemicznych i mechanicznych w ramach jednego procesu druku.

Wszystkie te rozwiązania technologiczne składają się na zintegrowaną mikrofluidycznie strategię wytwarzania, zdolną do programowania porowatości, składu i architektury w ramach jednego procesu technologicznego, umożliwiając kontrolę strukturalną od tworzenia szablonów porów w skali mikro po projektowanie rusztowań w skali makro oraz zapewniając skalowalną drogę do wytwarzania hierarchicznych, porowatych materiałów funkcjonalnie gradientowych dla przyszłych zastosowań biomedycznych.

Table of contents

Funding acknowledgment 3

List of publications 5

Abstract 7

Streszczenie (Abstract in polish) 9

List of figures 17

List of abbreviations 20

Chapter 1 - Introduction 24

1.1. The importance of being porous 24

1.1.1. From Natural Porosity to Engineered Systems 24

1.1.2. Functionally Graded Porous Materials 26

1.2. Microfluidic Approaches for the Fabrication of Porous FGMs 29

1.3. Digital Manufacturing Strategies for pFGMs 34

1.3.1. AM Techniques for pFGMs 35

1.4. Microfluidics-enhanced Extrusion-based 3D printing for Reproducible, Scalable, and Customizable pFGM 41

1.5. Biomedical Applications of Porous Functionally Graded Biomaterials 42

1.5.1. pFGMs for Bone Tissue Engineering 44

1.5.2. pFGMs for Interfacial Tissue Regeneration 46

1.6. Scope and Structure of the Thesis 48

1.6.1. Research Objectives and Hypotheses 48

1.6.2. Overview of the Thesis Chapters 52

Chapter 2 - Microfluidic 3D printing of emulsion ink for engineering porous functionally graded materials 53

2.1. Introduction 53

2.2. Materials and methods 55

2.2.1. Materials 55

2.2.2. Synthesis of Dextran Methacrylate 55

2.2.3. Synthesis of Gelatin Methacryloyl 56

2.2.4. Supporting bath for 3D printing 56

2.2.5. Fabrication of polycarbonate microfluidic chip 56

2.2.6. Microfluidic emulsion 57

2.2.7. Image analysis (FastCAM) and emulsion characterization 58

2.2.8. Emulsion 3D printing of cylindrical porous scaffolds and complex geometries 58

2.2.9. Scaffolds cross-linking and purification 59

2.2.10. Scanning Electron Microscopy 59

2.2.11. Microcomputed Tomography 60

2.2.12. Optical coherence microscopy 60

2.2.13. Bright-field imaging 61

2.2.14. Rheological measurements of emulsion inks 62

2.2.15. Mechanical testing of 3D printed emulsion scaffolds 62

2.2.16. *In vitro* degradation test 63

2.2.17. Mass swelling ratio 63

2.2.18. Statistical analysis 64
2.3. Results and Discussion 64
2.3.2. Exploring operational ranges and rheological properties of microfluidic emulsion inks 64
2.3.3. Emulsion ink printing in an agarose fluid-gel 69
2.3.4. 3D printing complex FGM architectures in agarose fluid-gel 76
2.4. Conclusions 82
Chapter 3 - Microfluidic-Assisted Digital Manufacturing of Functionally Graded Porous Ceramics 84
3.1. Introduction 84
3.2. Materials and Methods 87
3.2.1. Materials 87
3.2.2. Synthesis of Doubly Methacrylated Gelatin 87
3.2.3. Preparation of 3D printing Supporting bath 88
3.2.4. Fabrication of Polycarbonate Microfluidic Chip 89
3.2.5. Microfluidic Emulsion 89
3.2.6. Image analysis (FastCAM) and emulsion characterization 90
3.2.7. Emulsion 3D printing of cubic porous scaffolds and complex geometries 91
3.2.8. Scaffold cross-linking and sintering 92
3.2.9. Microcomputed Tomography 92
3.2.10. Scanning Electron Microscopy 93
3.2.11. Rheological Measurement 93

3.2.12. Mechanical testing of 3D printed ceramic scaffolds..... 94
3.2.13. Thermogravimetric analysis..... 94
3.2.14. Evaluation of the osteogenic properties of the nHA scaffolds 94
3.2.15. Immunofluorescence (IF) staining..... 95
3.2.16. Alamar Blue..... 96
3.2.17. Quantitative real-time polymerase chain reaction 96
3.2.18. Statistical Analysis..... 98
3.3. Results and Discussion..... 99
3.3.1. Microfluidic generation of emulsion templates and control over pore architecture 99
3.3.2. Rheological characterization and embedded printing strategy ……...101
3.3.3. Material conversion, sintering behaviour, and mechanical response ……...104
3.3.4. Bioactivity and Osteoinductive Capacity of Porous Ceramic Scaffolds toward Stem Cells..... 110
3.4. Conclusion..... 116
Chapter 4 - Microfluidic-Mixer Assisted 3D Printing of Functionally Graded Multimaterial Hydrogels for Engineering Complex Tissue Interfaces 118
4.1. Introduction 118
4.2. Materials and Methods 120
4.2.1. Materials 120

4.2.2. Synthesis of Dextran-Methacrylate 120
4.2.3. Synthesis of Gelatin-Methacryloyl 121
4.2.4. Preparation of 3D printing Supporting bath 121
4.2.5. Fabrication of Polycarbonate Microfluidic Chip 121
4.2.6. Rheological Measurement 122
4.2.7. Microfluidic mixing and emulsion generation 122
4.2.8. Mixing Index 123
4.2.9. Emulsion 3D printing of Cubic Porous Scaffold and Complex Geometries 125
4.2.10. Scaffold cross-linking and purification 126
4.2.11. Fourier Transform Infrared Analysis 126
4.2.12. X-ray computed tomography analysis 127
4.2.13. Mechanical testing 127
4.2.14. Culture of 3T3-fibroblast and cytocompatibility testing 128
4.2.15. Live/dead assay 128
4.2.16. Immunofluorescence (IF) staining 129
4.2.17. Cell density determination 129
4.2.18. Statistical Analysis 129
4.3. Result and discussion 130
4.3.1. Micromixer and flow-focusing microfluidic printhead 130
4.3.2. 3D printing 136
4.3.3. Cell viability on the heterogeneous scaffold 141
4.4. Conclusions 145

Chapter 5 – Conclusions..... 148

References..... 151

List of figures

Figure 1.1 Overview of natural porous materials 26

Figure 1.2 Functionally graded materials (FGMs) 27

Figure 1.3 Porosity and interconnections within the scaffold 28

Figure 1.4 Overview of three microfluidic droplet generator geometries: 32

Figure 1.5 Schematic representation of the manufacturing workflow 35

Figure 1.6 Representative AM techniques 37

Figure 1.7 Embedded 3D printing of hydrogel structures within FRESH support bath. 40

Figure 1.8 Conceptual illustration of a microfluidic-integrated 3D bioprinting platform. 42

Figure 1.9 Overview of the tissue engineering paradigm 44

Figure 1.10 Schematic representation of the femur 45

Figure 1.11 Schematic representation of the osteochondral unit 47

Figure 2.1 Sequence of steps illustrating the process of scaffold fabrication and purification. 65

Figure 2.2 Operational range exploration for emulsion ink production. 68

Figure 2.3 3D printing of porous FGMs 70

Figure 2.4 Morphological characterization of 3D printed porous FGMs 72

Figure 2.5 Compression mechanical characterization of 3D printed porous FGMs. 74

Figure 2.6 Internal topographic analysis via microCT and OCM. 75

Figure 2.7 3D printing of complex FGM in fluid-gel 77

Figure 2.8 3D printing of complex architecture in fluid-gel. 78

Figure 2.9 Operational range exploration for GelMA emulsion ink production..... 79

Figure 2.10 Printing a gradient mix of multiple materials 80

Figure 3.1 Operational range exploration for emulsion ink production. 101

Figure 3.2 Microfluidic-assisted embedded printing and rheology of GelMOD-nHA emulsions 104

Figure 3.3 Structural evolution and mechanical properties of the microfluidic-templated ceramic scaffolds 108

Figure 3.4 pFGMs internal topographic analysis via microCT 110

Figure 3.5 Biological evaluation of porous ceramic scaffol 115

Figure 3.6 Immunofluorescence analysis of hMSC osteogenic differentiation on porous scaffolds 116

Figure 4.1 Schematic representation of different microfluidic micromixer geometries composed of two superimposed layers 124

Figure 4.2 mix-ff-MPH bearing a passive micromixer. 134

Figure 4.3 Analysis of MI and average Intensity for 4 different geometries of microfluidic micromixer. 135

Figure 4.4 Analysis of MI and average Intensity 136

Figure 4.5 Operational set-up..... 139

Figure 4.6 FTIR spectra of GelMA/DexMA pFGMs 140

Figure 4.7 3T3 fibroblast adhesion on a functionally graded hydrogel, 30% porosity. 144

Figure 4.8 3T3-fibroblast cell adherence study on GelMA:DexMA scaffold..... 145

List of abbreviations

AEMA·HCl - 2-Aminoethyl Methacrylate Hydrochloride

AM - Additive Manufacturing

BSA - Bovine Serum Albumin

CAD - Computer-Aided Design

cDNA - Complementary DNA

CNC - Computerized Numerical Control

CV - Coefficient of Variation

DAPI - 4′,6-Diamidino-2-Phenylindole

DDW - Double-Distilled Water

DexMA - Dextran Methacrylate

DIW - Direct Ink Writing

DMA - Dynamic Mechanical Analysis

DMAP - 4-Dimethylaminopyridine

DMEM - Dulbecco's Modified Eagle Medium

DMSO - Dimethyl Sulfoxide

DS - Degree of Substitution

EDC - 1-Ethyl-3-(3-dimethylaminopropyl)carbodiimide

FBS - Fetal Bovine Serum

FDM - Fused deposition modeling

FGM - Functionally Graded Material

FITC - Fluorescein Isothiocyanate

ff-MPH - flow-focusing microfluidic printing head

FTIR - Fourier Transform Infrared Spectroscopy

GelMA - Gelatin Methacryloyl

GelMOD - Gelatin Double Metacrylate

GM - Growth Medium

GMA - Glycidyl Methacrylate

HBSS - Hanks' Balanced Salt Solution

HCl - Hydrochloric Acid

HMDS - Hexamethyldisilazane

hMSCs - Human Mesenchymal Stem Cells

IF - Immunofluorescence

LAP - Lithium Phenyl-2,4,6-trimethylbenzoylphosphinate

LSCM - Laser Scanning Confocal Microscopy

MA - Methacrylic Anhydride

microCT - Microcomputed Tomography

MI - Mixing Index

MPH - Microfluidic Printhead

mix-ff-MPH - Micromixer–Flow-Focusing Microfluidic Printhead

MWCO - Molecular Weight Cut-Off

nHA - Nanohydroxyapatite

NHS - N-Hydroxysuccinimide

OCN - Osteocalcin

OCM - Optical Coherence Microscopy

OM - Osteogenic Medium

OPN - Osteopontin

O/W - Oil-in-Water

PBS - Phosphate Buffered Saline

PED - Precision Extrusion Deposition

pFGHs - Porous Functionally Graded Hydrogels

polyHIPEs - polymerized high internal phase emulsions

P/S - Penicillin/Streptomycin

PCR - Polymerase Chain Reaction

pFGMs - Porous Functionally Graded Materials

PFA - Paraformaldehyde

qRT-PCR - Quantitative Polymerase Chain Reaction

rpm - Revolutions per Minute

RT - Room Temperature

SEM - Scanning Electron Microscopy

SLA - Stereolithography

SLS - Selective Laser Sintering

$SnCl_2$ - Tin(II) Chloride

STL - Stereolithography interface format

TGA - Thermogravimetric Analysis

UV - Ultraviolet

Chapter 1 - Introduction

1.1.The importance of being porous

Porous materials are everywhere around us, spread across natural and engineered environments[1]. Natural systems such as bone, wood, coral reefs, and plant tissues exhibit interconnected pore networks whose architecture is tightly coupled to function. In these contexts, porosity serves as an optimized design parameter rather than a structural imperfection, enabling integration of mechanical performance with mass transport and biological activity. These architectures are not random; instead, they arise through prolonged optimization processes that reconcile structural efficiency, transport capability, and functional robustness[2]. Relying on these principles, materials scientists have engineered porous materials that replicate aspects of similar multifunctional behavior. Hence, porous architecture attracts significant attention for applications such as acoustic damping, filtration, thermal insulation, catalysis, and biomedical technologies[1,3,4]. The outstanding challenge, nevertheless, is the rational control of both composition and the three-dimensional pore-network architecture, such that structural, transport, and functional properties can be tailored in a predictable manner.

1.1.1. From Natural Porosity to Engineered Systems

Natural porous materials provide some of the most sophisticated examples of functional architecture. Bone, wood, coral, sponges, and plant tissues exhibit interconnected pore networks that enable the transport of fluids, nutrients, and signaling molecules while maintaining mechanical stability[5]. Skeletal tissues, for example, demonstrate how high porosity can coexist with significant load-

bearing capability, challenging the traditional engineering assumption that density and strength are directly correlated[6,7]. A defining characteristic of natural porous structures is their hierarchical organization across multiple length scales, from nanoscale molecular arrangements to macroscopic architectures (**Figure 1.1**)[8,9]. Each structural level fulfills a distinct function: molecular interactions at the nanoscale, cellular accommodation and fluid transport at the microscale, and mechanical support at the macroscale. The integration of these levels generates emergent properties that cannot be reproduced by homogeneous architecture. These principles establish hierarchy and gradation as fundamental design rules for advanced biomaterials. Moreover, natural porous systems are characterized by gradual spatial transitions rather than abrupt interfaces. Such smooth transitions minimize stress concentration and enhance durability. Therefore, gradient-based design emerges as a fundamental principle to ensure mechanical continuity and functional robustness across interfaces[7].

When translated into synthetic systems, these hierarchical and graded porous architectures acquire particular relevance in contexts where materials can operate within complex and dynamic environments. In biological tissues, for instance, porosity governs not only structural behavior but also transport phenomena and cellular organization. The ability to reproduce such multiscale and graded features, therefore, represents a critical step toward engineering materials intended to interact with living systems in a controlled and functional manner.

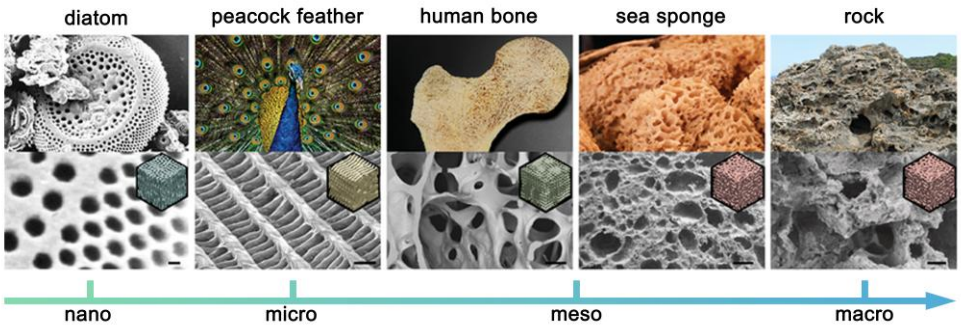

Figure 1.1 Overview of natural porous materials organized across length scales from nano- to macro-dimensions based on their characteristic features. Scanning Electron Microscopy (SEM) or optical microscopy (OM) images of the structures are shown from left to right: diatom, peacock feather, human bone, sea sponge, and rock. Insets highlight spinodoid architectures with similar topologies, including columnar, lamellar, cubic, and isotropic forms. Image adapted from [8].

1.1.2. Functionally Graded Porous Materials

In the 80s, a significant advancement in materials engineering was achieved through the introduction of compositional and micro-architectural gradients within a single material system[10]. By varying properties such as composition, porosity, or pore size along at least one spatial direction, researchers developed what are now known as functionally graded materials (FGMs) (**Figure 1.2**)[10]. FGMs were originally conceived in Japan to meet the demanding requirements of aerospace applications[11,12], where materials needed to combine high thermal resistance on the external surface with superior mechanical toughness internally, for instance, in thermal barrier coatings for space vehicles. Since then, significant effort has been devoted to exploring the potential of this class of materials from a manufacturing and materials modeling perspective.

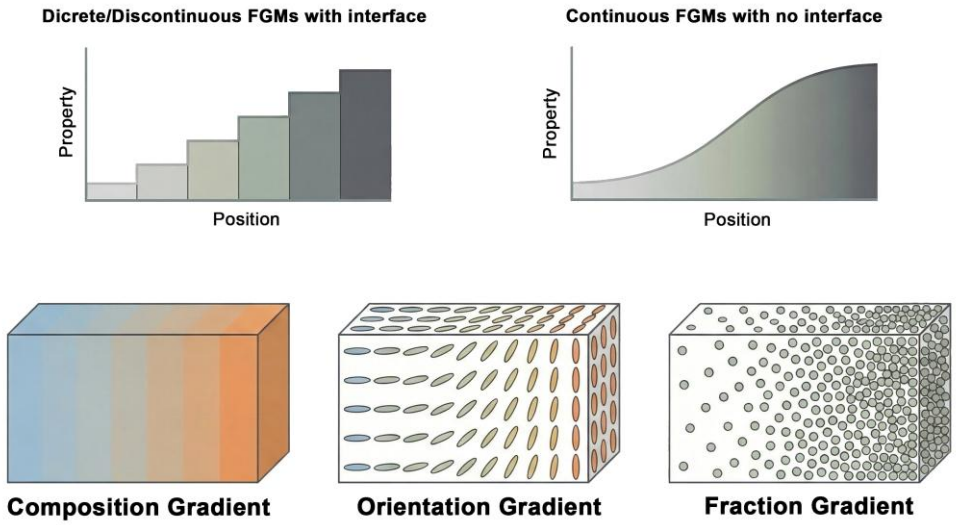

Figure 1.2 Functionally graded materials (FGMs) exhibiting different types of gradients. Top: schematic representation of discrete/discontinuous FGMs with distinct interfaces and continuous FGMs with smooth property variation. Bottom: examples of gradient types, including composition gradient, orientation gradient, and fraction gradient.

The emergence of FGMs marked a conceptual shift from homogeneous material design toward spatially programmed functionality[12,13]. Despite significant advances in controlling pore morphology and microstructure, most early engineered porous materials remained macroscopically homogeneous, exhibiting uniform properties throughout the construct. Inspired by natural paradigms, the engineering of porous materials has evolved substantially over the last century. The growing demand for high-performance porous materials in both industry and the biomedical field has driven the development of synthetic systems. Porous materials now span a wide range of chemistries, including polymers, ceramics, metals, and composites[13]. In engineered materials, functional properties depend not only on the intrinsic characteristics of the base material, but also on the 3D arrangement of the pore network. Critical parameters include pore size and distribution, interconnectivity (open vs. closed cells), spatial arrangement, and overall porosity (**Figure 1.3**). Controlling these interdependent variables is essential, as different

combinations of porosity, composition, and architecture can yield competing effects on mechanical strength, mass transport, and biological response[14]. The complexity arising from these coupled parameters has motivated the development of advanced manufacturing strategies capable of tailoring both material formulation and porous microarchitecture with high precision[15–17]. The emergence of FGMs introduced the possibility of embedding spatial heterogeneity directly into the material architecture, thereby enabling position-dependent functionality within a single integrated system[18].

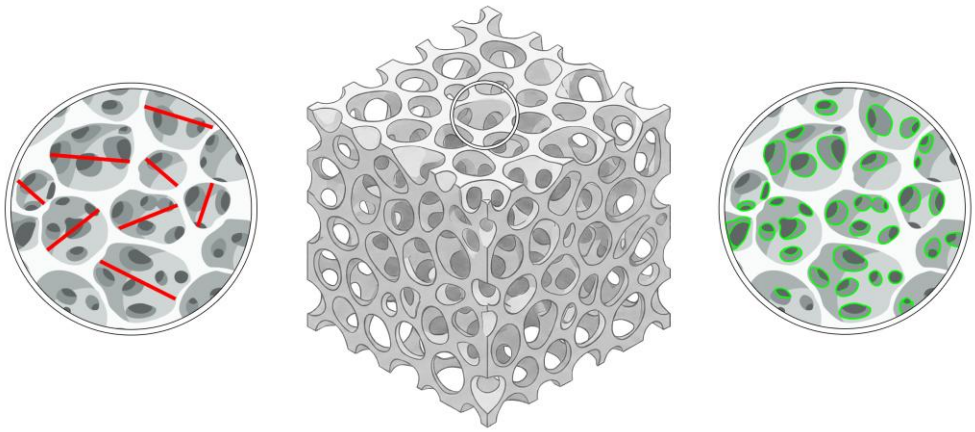

Figure 1.3 Porosity and interconnections within the scaffold. Porous scaffold with (left) dimensions of the pores in red and (right) dimensions of the interconnections in green.

Among FGMs, a specific subclass has emerged: porous functionally graded materials (pFGMs)[19]. These materials integrate controlled porosity with spatial gradients in composition or mechanical properties, enabling a closer emulation of the structural complexity found in native biological tissues. By combining compositional and microarchitectural gradients within a single construct, pFGMs expand the design space, enabling the development of materials with highly tailored, potentially unprecedented structural and functional properties.

While initially developed for structural and thermal applications, the intrinsic ability of pFGMs to couple mechanical modulation with controlled transport properties has progressively attracted attention in fields characterized by spatial heterogeneity and multifunctional requirements. This is particularly evident in the biomedical field[20,21], where porous functional graded scaffolds offer a strategy to reconcile mechanical compatibility, stress distribution, and biochemical transport within a single construct. Their graded architecture can facilitate improved mechanical compatibility with host tissues, promote more uniform stress distribution, and support controlled transport or release of bioactive molecules. Such features make them attractive candidates for the regeneration of complex tissues and organs.

Despite their significant potential, the fabrication of pFGMs, remains challenging. Manufacturing processes are often complex and costly, and achieving precise control over critical parameters, such as density, pore size, and material distribution, remains difficult[22]. Various fabrication techniques have been explored for pFGM production, including centrifugal casting[23], sedimentation, spark plasma sintering[24], and, more recently, multiphase fluid-based approaches and rapid prototyping technologies, which have demonstrated promising results[25,26]. However, further advancements are required to enable scalable, reproducible, and finely tunable manufacturing strategies.

1.2.Microfluidic Approaches for the Fabrication of Porous FGMs

The fabrication of porous materials through multiphase fluid templating has been widely explored due to its versatility and relatively simple processing routes[27–29]. Conventional strategies such as polymerized high internal phase

emulsions (polyHIPEs)[30] and gas foaming[31] techniques have demonstrated the feasibility of producing highly porous structures with high throughput and broad material compatibility. In these approaches, pore formation relies on the generation of droplets or bubbles[32] within a continuous phase, which are subsequently solidified, while the dispersed phase serves as a sacrificial template. However, droplet and bubble formation in bulk systems is typically governed by mechanical stirring or by uncontrolled nucleation. As a consequence, the size of the dispersed domains cannot be precisely controlled, leading to broad pore-size distributions and a random spatial organization in the final material[33]. Such structural heterogeneity can negatively affect mechanical reliability, transport properties, and, more critically, the possibility of engineering spatially defined porosity gradients. The lack of deterministic control over droplet size and arrangement, therefore, represents a major limitation in the design of pFGMs, where microstructural precision is essential[34].

To overcome these limitations, increasing attention has been directed toward microscale fluid manipulation strategies. In this context, microfluidics has emerged as a powerful platform for engineering multiphase systems with unprecedented accuracy[35]. Microfluidics refers to the manipulation of fluids within channels with dimensions typically ranging from tens to hundreds of micrometers[36]. At this scale, fluid behavior is dominated by laminar flow, and transport phenomena such as diffusion, interfacial tension, and viscous forces are highly controllable. Beyond droplet generation, microfluidic systems also enable precise control over fluid mixing at the microscale. Due to the laminar flow regime that dominates microchannels, fluids tend to flow in parallel streams with limited spontaneous mixing[37]. To enhance interfacial contact between phases, passive microfluidic mixers are often employed[38]. These

devices rely on geometrical features, such as serpentine channels, staggered herringbone structures, or split-and-recombine architectures[37,39], to promote chaotic advection and accelerate mixing by repeatedly stretching and folding fluid interfaces. Controlled microfluidic mixing is particularly relevant when multiple precursor solutions must be combined with spatial or temporal precision. In the context of FGM, this capability enables the dynamic modulation of material composition during processing[40]. In parallel with compositional control, microfluidic platforms also provide precise regulation of droplet formation through different microchannel geometries, such as T-junction[41], flow-focusing[42], and co-flow configurations[43] (**Figure 1.4**), enabling accurate control over droplet size, uniformity, and spatial distribution. The generation of highly monodisperse droplets is particularly relevant for porous material fabrication, as each droplet serves as a template for pore formation. As a result, microfluidic systems enable the creation of scaffolds with spherical pore architectures, characterized by well-defined size, uniformity, and isotropy. This templating strategy provides a level of structural control that is difficult to achieve with conventional bulk emulsification methods, where droplet size distributions are typically broader and less predictable.

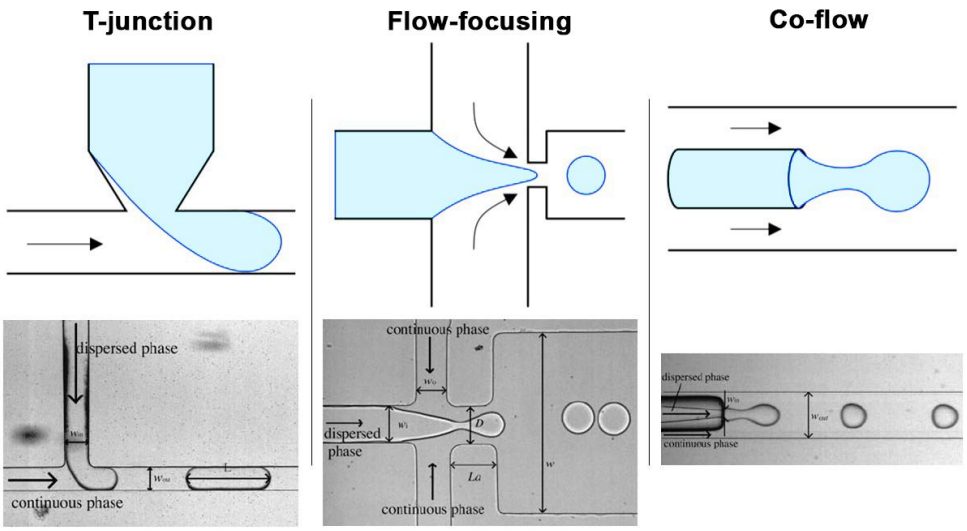

Figure 1.4 Overview of the three most widely used microfluidic droplet generator geometries: T-junction, flow-focusing, and co-flow. Top: schematic illustrations of droplet formation mechanisms. Bottom: corresponding experimental images, highlighting differences in droplet breakup and flow regimes.

Unlike bulk emulsification, where droplet formation results from turbulent mixing, microfluidic systems enable the controlled interaction of immiscible phases, typically aqueous and organic, within channels under well-defined hydrodynamic regimes, allowing architecture to be programmed rather than statistically distributed[44]. In addition to mixing control, microfluidic platforms enable deterministic droplet generation. Droplet size can be precisely tuned by regulating flow rate, typically achieving diameters in the 10–1000 μm range and a polydispersity index below 5%[41]. Pore templating thus transitions from a statistical outcome to a programmable process.

The dispersed phase volume fraction (φ), defined as the volumetric ratio between the dispersed phase and the total emulsion volume, plays a crucial role in determining droplet packing density and, consequently, the resulting pore architecture. As φ increases, droplets become densely packed; above the close-packing threshold ($\varphi \approx 0.74$ for monodisperse spheres[45]), droplets

deform into polyhedral geometries, reducing the thickness of the continuous phase films separating adjacent droplets. The value of φ, therefore, plays a crucial role in determining the final pore architecture after removal of the dispersed phase, directly influencing porosity, interconnectivity, and mechanical stability. Lower φ values lead to fewer and narrower interconnections, which may hinder cellular infiltration and proliferation within scaffold structures. Despite their structural advantages, emulsions are thermodynamically unstable systems. Instability mechanisms such as coalescence[46], which droplets merge to form larger domains, and Ostwald ripening[47], in which larger droplets grow at the expense of smaller ones, can compromise droplet uniformity over time. Surfactants are commonly employed to reduce interfacial tension and kinetically stabilize the system, although they cannot entirely prevent long-term degradation[40]. Among the different emulsion types, oil-in-water (O/W) emulsions are particularly relevant for the fabrication of porous scaffolds[48,49]. In O/W systems, the organic phase is dispersed within an aqueous continuous phase. These systems are especially attractive in microfluidic regimes due to their higher interfacial tension, which enables robust droplet formation and enhanced size control[40]. Furthermore, the presence of an organic dispersed phase allows the processing of hydrophobic polymers and facilitates solidification strategies such as solvent evaporation or photo-crosslinking, resulting in mechanically stable porous matrices. However, incorporating an organic dispersed phase may raise compatibility concerns in biological contexts, as residual solvents, unreacted monomers, or surfactants can affect cytocompatibility and compromise structural integrity if not properly removed[50].

The precise tuning of microfluidic flow parameters enables the fabrication of monodisperse, bi-disperse, or continuously graded droplet assemblies, which,

upon removal of the dispersed phase, yield controlled pore-size distributions and porosity gradients suitable for the production of pFGMs[18]. While microfluidics enables precise control over microscale pore templating and compositional modulation, it does not inherently define the global three-dimensional geometry of the final construct. Droplet organization at the microscale does not automatically translate into architected macroscale structures. Consequently, the fabrication of pFGMs requires integration between microfluidic material control and complementary manufacturing strategies capable of defining spatial architecture at the construct level.

1.3.Digital Manufacturing Strategies for pFGMs

While microfluidic systems enable precise control over droplet generation and resulting microscale pore architecture, they do not inherently provide control over the overall three-dimensional geometry of the resulting construct. The fabrication of pFGMs, therefore, requires an additional strategy capable of defining macroscopic shape, spatial organization, and architectural hierarchy. In this context, digital manufacturing, particularly additive manufacturing (AM), represents a complementary and enabling technology[51]. AM has revolutionized the fabrication of complex 3D structures by translating digitally defined architecture into physical constructs with high spatial fidelity[52]. By building structures in a layer-by-layer process, AM offers unprecedented control over geometry, internal architecture, and material distribution. These capabilities are particularly valuable in the context of pFGMs, where spatial modulation of porosity, composition, and mechanical properties must be precisely engineered rather than approximated.

The integration of computer-aided design (CAD)[53,54] and computational modeling (**Figure 1.5**) with process parameter control enables the rational design of architectures tailored to specific mechanical and biological requirements. Structural features such as infill density, pore architecture, and gradient transitions can be systematically programmed and reproducibly fabricated, ensuring consistency between the digital model and the physical construct.

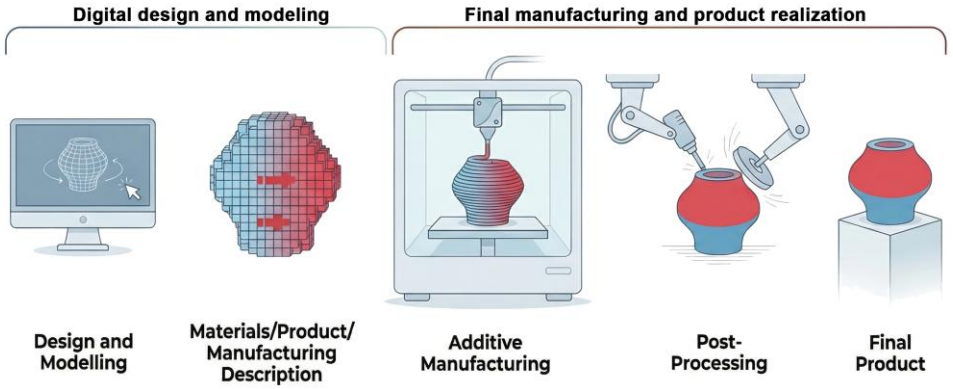

Figure 1.5 Schematic representation of the manufacturing workflow, from digital design and material definition to AM, post-processing, and final product realization.

1.3.1. AM Techniques for pFGMs

From a technological point of view, AM systems – as the name suggests – have introduced the innovative concept of building objects by adding successive layers of material, in contrast with conventional subtractive manufacturing processes such as milling, turning, drilling, or grinding[55]. This paradigm shift enables the fabrication of 3D complex architectures – with almost no design limits – that could not be produced using traditional manufacturing techniques.

Unlike subtractive processes, AM provides precise control over internal architecture and spatial material distribution, which is particularly advantageous for pFGM design[56]. Among the broad spectrum of AM technologies, four modalities have gained prominence for the fabrication of porous and architected materials: fused deposition modeling (FDM)[57], precision extrusion deposition (PED)[58], stereolithography (SLA)[59], and selective laser sintering (SLS)[60] (**Figure 1.6**). However, these technologies differ substantially in terms of resolution, material compatibility, processing constraints, and suitability for graded porous architectures. A critical comparison is therefore necessary when evaluating their relevance for pFGM fabrication. FDM and PED rely on the extrusion of thermoplastic polymers or highly filled pastes through a heated nozzle, enabling straightforward fabrication of lattices, infill structures, and deterministic pore architectures. Nevertheless, their resolution is typically limited by nozzle diameter and filament spreading, and gradient implementation often remains stepwise rather than continuous. SLA, based on photopolymerization of liquid resins, enables high resolution and smooth surface definition but is restricted to photocurable systems and may present challenges when processing multiphase or highly loaded formulations. SLS employs laser-induced sintering of polymeric or composite powders, producing mechanically robust structures with tunable microporosity, although powder handling and thermal gradients introduce process complexities and limit control over compositional gradients.

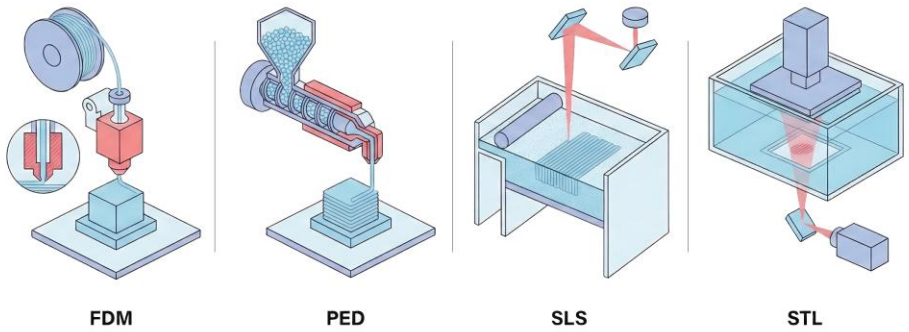

Figure 1.6 Representative AM techniques for scaffold fabrication FDM, PED, SLS, and SLA. Each technique relies on distinct material processing mechanisms, including thermoplastic extrusion, direct ink writing, powder sintering, and photo-induced polymerization, respectively.

From a structural perspective, these techniques allow the fabrication of scaffolds with predefined lattice geometries, controlled interconnectivity, and anisotropic architectures. Such control is essential for tailoring mechanical stiffness, permeability, and mass transport behavior in porous systems. However, most of these methods primarily control architected macroporosity[61] and provide limited intrinsic capability to couple pore templating at the microscale with spatially graded composition within a single continuous process.

Despite these advantages, no single additive manufacturing technique currently provides a "one-for-all" solution for the fabrication of trabecular-like porous architectures, simultaneously enabling full control over structural resolution, material composition, and spatial organization within a single process[62]. Light-based approaches, including advanced volumetric[63] and two-photon polymerization techniques[64], represent the state of the art in terms of resolution and geometric complexity. However, their application remains constrained by limited multi-material capability, high equipment costs, and reduced throughput, particularly when scaling to larger constructs[65]. Among

AM techniques, extrusion-based strategies are particularly versatile and accessible platforms for fabricating pFGMs[66]. In extrusion-based processes, material is continuously deposited through a nozzle under controlled pressure, forming filaments that stabilize after deposition. The final architecture is defined by toolpath design, extrusion parameters, and inter-filament spacing. Although typically characterized by lower resolution compared to SLA, extrusion-based approaches offer broader material compatibility and greater flexibility in processing viscous, composite, and multiphase formulations. This versatility enables the processing of thermoplastic polymers, hydrogels, ceramic pastes, composites, and highly filled suspensions. For pFGMs that require spatial control over composition and architecture within a single process, extrusion-based systems therefore represent a particularly versatile platform.

From a structural perspective, extrusion-based printing enables control over pore size, porosity, interconnectivity, and anisotropy through parameters such as nozzle diameter, extrusion rate, layer height, and filament spacing[67]. This allows the fabrication of hierarchical porous structures with tailored mechanical and transport properties. Despite this high degree of control over macroscopic architecture, the regulation of pore structure at the microscale remains limited[68,69]. In many cases, porosity arises from filament spacing or process-induced effects, resulting in architectures that are not fully programmable in terms of pore size, shape, and spatial distribution[67]. This limitation becomes particularly relevant in applications requiring precise control over both composition and pore architecture across multiple length scales[15,16]. From a processing perspective, extrusion-based technologies generally operate under relatively mild conditions[70] compared to high-energy AM techniques, i.e. SLS, STL, PED and, FDM. They often avoid intense

radiation and can operate at moderate or near-room temperatures, which is advantageous for temperature-sensitive materials and systems incorporating bioactive components.

However, conventional extrusion-based printing imposes strict rheological requirements on printable formulations. To ensure filament stability and shape fidelity upon deposition in air, materials must exhibit sufficiently high viscosity, shear-thinning behavior, or rapid solidification kinetics[71]. This requirement can restrict the range of printable multiphase systems and compromise the preservation of microscale structures generated upstream, particularly in emulsion-based formulations. To overcome this limitation, support bath printing strategies[72,73] have been developed, enabling material deposition within a yield-stress support medium. In this approach, the surrounding support matrix, typically based on agarose or granular hydrogel, temporarily stabilizes the extruded filament during layer-by-layer fabrication. By mechanically confining the deposited filament, the support bath decouples structural fidelity from strict rheological constraints, enabling the processing of low-viscosity, multiphase, or weakly crosslinked formulations that would otherwise collapse.

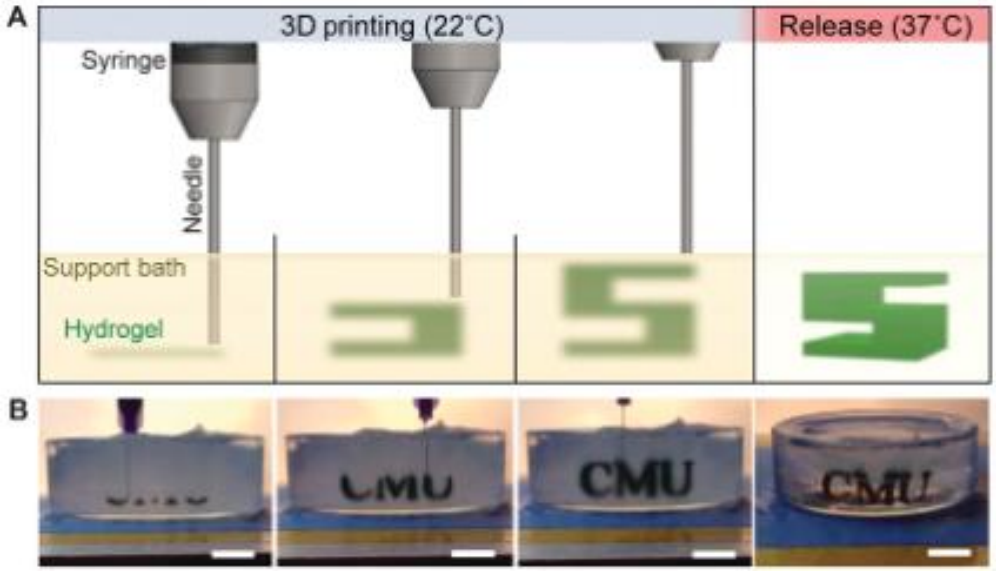

Figure 1.7 Embedded 3D printing of hydrogel structures within FRESH support bath. **a)** Schematic illustration of the printing process at room temperature (22 °C), followed by release of the printed construct at physiological temperature (37 °C). **b)** Representative images of printed hydrogel structures demonstrating shape fidelity and structural integrity after printing and release. Scale bars, b) 1 cm. Image adapted from [72].

The introduction of extrusion-based AM combined with a microfluidic printhead enables controlled multiphase droplet generation prior to filament deposition, facilitates the preservation of engineered droplet architectures during extrusion, and allows multiscale integration between microscale pore templating and macroscale construct definition. The incorporation of a support bath further ensures filament stabilization during 3D construct formation.

Such integration establishes a robust manufacturing microfluidic-assisted extrusion platform capable of fabricating pFGMs with deterministic structural and compositional control, consistent with the design requirements of a porous, functionally graded biomaterial scaffold.

1.4.Microfluidics-enhanced Extrusion-based 3D printing for Reproducible, Scalable, and Customizable pFGM

While extrusion-based AM enables precise control over scaffold geometry, its ability to regulate pore architecture at the microscale remains inherently limited[51,61], as porosity is largely governed by filament spacing and process-dependent factors[66,67], leading to irregular pore geometries and limited control over size distribution and interconnectivity.

In contrast, integrating microfluidic droplet generation with extrusion-based 3D printing introduces a new level of control over pore formation. By templating the structure with monodisperse droplets, it becomes possible to engineer spherical pore architectures with well-defined size, uniformity, and spatial distribution. When combined with programmable deposition strategies, such systems enable the fabrication of spherical-based porous metamaterials, in which both microstructural and macroscopic features can be precisely tailored. Beyond structural control, integrating microfluidics with AM also offers significant advantages in process reliability and manufacturing consistency. Digital manufacturing addresses critical translational challenges related to reproducibility and scalability[74]. The digital nature of the fabrication process enables standardized protocols, parameter optimization, and data-driven refinement of scaffold designs. This reproducibility is particularly important in biomedical applications, where batch-to-batch variability can significantly impact biological outcomes.

Furthermore, digital manufacturing offers a pathway toward patient-specific and application-driven solutions[75]. By integrating imaging data, computational modeling, and fabrication, constructs can be customized to

match defect geometries or targeted functional gradients. When combined with microfluidic strategies for precise material formulation and gradient generation, digital manufacturing bridges the gap between microscale material control and macroscale structural complexity. This integration ultimately enables the realization of advanced porous functionally graded biomaterials for regenerative applications (**Figure 1.8**).

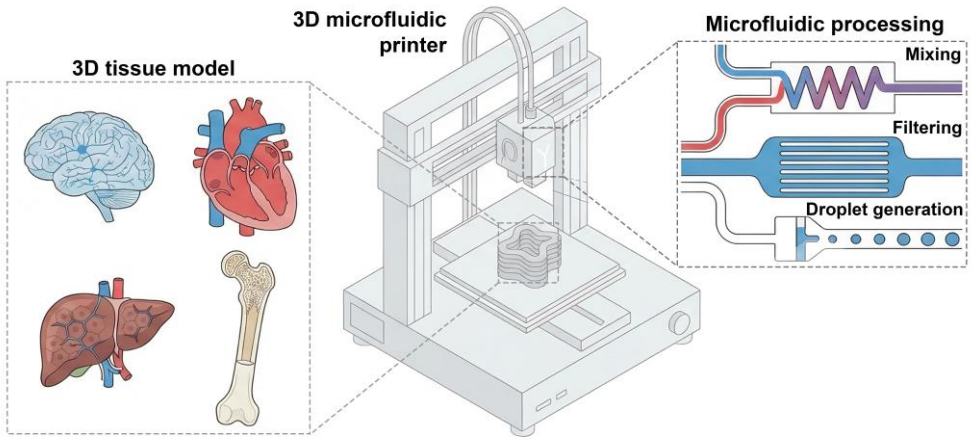

Figure 1.8 Conceptual illustration of a microfluidic-integrated 3D bioprinting platform. A microfluidic printhead enables in-line control over material composition and droplet formation (e.g., mixing, filtering, droplet generation), while the extrusion-based printing system deposits the resulting bioink into predefined architectures. This integration allows simultaneous control over microscale features and macroscale geometry, enabling the fabrication of structurally complex and functionally graded constructs.

1.5.Biomedical Applications of Porous Functionally Graded Biomaterials

pFGMs are particularly well suited for biomedical applications characterized by spatially heterogeneous tissue environments[76]. Many biological tissues exhibit gradual transitions in composition, structure, and mechanical properties rather than sharp interfaces. Replicating these gradients is essential to restoring physiological function, ensuring mechanical compatibility, and promoting long-term integration[77].

Within the broader field of tissue engineering and regenerative medicine, significant efforts have been devoted to developing strategies to restore or replace damaged tissues through the combined use of biomaterials, cells, and biochemical cues[78] (**Figure 1.9**). In this framework, biomaterial scaffolds serve as temporary three-dimensional templates that support cellular attachment, proliferation, and differentiation while guiding the formation of new tissue[79]. The scaffold architecture plays a critical role in regulating key biological processes such as nutrient diffusion, waste removal, vascularization, and extracellular matrix deposition[80]. An effective scaffold must therefore simultaneously satisfy multiple design requirements, including biocompatibility, appropriate mechanical properties, and a porous architecture that allows cell infiltration and mass transport. However, many native tissues exhibit hierarchical organization and gradual transitions in structure and composition, making it difficult to reproduce their functional behavior using homogeneous materials. As a consequence, conventional scaffolds with uniform properties often fail to replicate the spatial complexity of physiological environments[79]. In this context, pFGMs provide a promising strategy to better mimic the heterogeneity of biological tissues. The combination of controlled porosity and spatially graded composition enables the design of scaffolds that simultaneously address mechanical support, mass transport, and biological signaling. In this framework, extrusion-based AM integrated with microfluidic material control provides the architectural freedom and compositional tunability required to engineer continuous or stepwise gradients within a single construct[81]. Among the various clinical targets, bone and osteochondral tissues represent paradigmatic examples in which structural hierarchy and property gradients are fundamental to mechanical performance and biological activity.

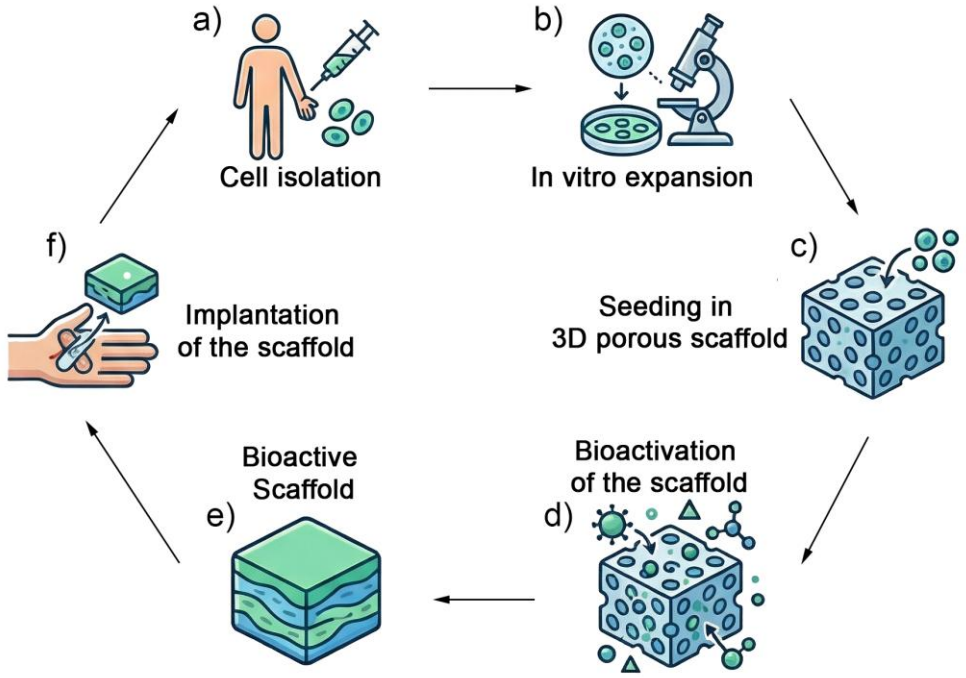

Figure 1.9 Overview of the tissue engineering paradigm. The process includes a) cell isolation, b) in vitro expansion, c) seeding within a three-dimensional porous scaffold, d) bioactivation through the incorporation of bioactive cues, e) formation of a functional bioactive construct, and f) implantation to support tissue regeneration.

1.5.1. pFGMs for Bone Tissue Engineering

Bone is a hierarchical, anisotropic, and dynamic tissue that combines structural load-bearing capacity with metabolic and regenerative functions[82,83]. At the macroscopic scale, cortical bone provides stiffness and structural integrity, while trabecular bone exhibits high porosity and facilitates metabolic exchange[82,84] (**Figure 1.10**). At smaller scales, mineralized collagen fibrils and lamellar organization contribute to mechanical resilience and toughness.

Scaffolds intended for bone tissue engineering must therefore satisfy multiple, and sometimes competing, requirements[83,85]. First, they must provide sufficient mechanical stability to withstand physiological loads, particularly in load-bearing applications. Second, they must exhibit interconnected porosity to promote

vascularization, nutrient diffusion, and waste removal. Third, they should support cell adhesion, proliferation, and differentiation, ultimately enabling matrix deposition and remodeling.

Porosity plays a central role in balancing these functions. High porosity enhances mass transport and tissue ingrowth but reduces mechanical stiffness, whereas lower porosity increases mechanical strength but may hinder biological integration[86,87]. Functionally graded designs offer a solution by spatially modulating porosity and composition: regions requiring higher mechanical support can be denser and stiffer, while areas intended for rapid bone ingrowth can exhibit larger, more interconnected pores. In this way, pFGMs provide a structural strategy for reconciling mechanical integrity with biological functionality within a single construct[88].

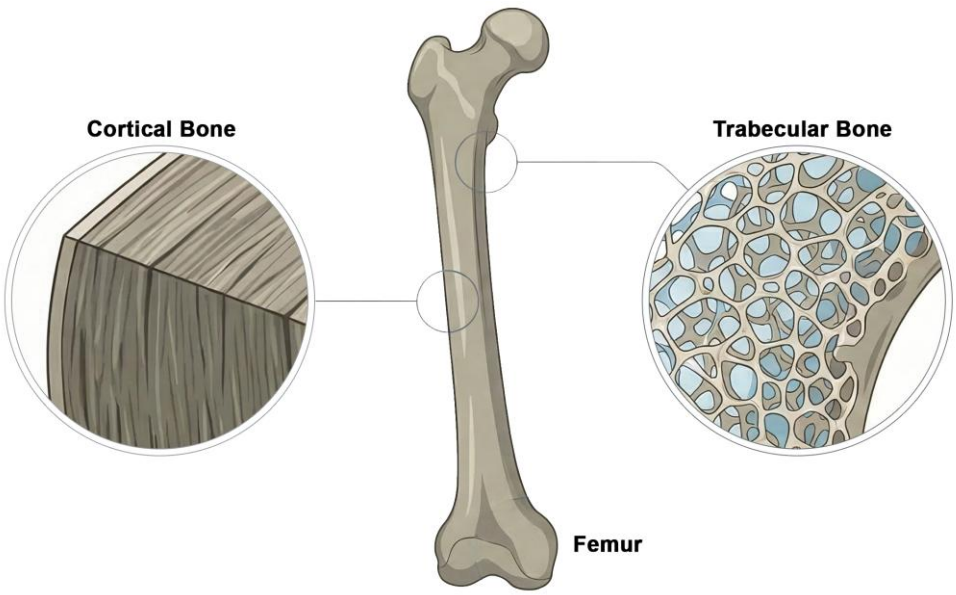

Figure 1.10 Schematic representation of the femur highlighting the hierarchical organization of bone tissue, characterized by dense cortical bone (left) and porous trabecular bone (right), which exhibit distinct structural and mechanical properties.

1.5.2. pFGMs for Interfacial Tissue Regeneration

The osteochondral interface represents a quintessential example of a naturally graded system[89]. It consists of a continuous transition from soft, viscoelastic cartilage to stiff, mineralized subchondral bone. This transition is characterized by progressive changes in extracellular matrix composition, mineral content, water content, and mechanical modulus. Cartilage is primarily composed of collagen type II and proteoglycans, providing compressive resistance and shock absorption[90]. In contrast, subchondral bone[91] contains a high mineralized matrix fraction, resulting in significantly higher stiffness and strength. Between these regions lies a calcified cartilage layer that functions as an interfacial transition zone, bridging cartilage and subchondral bone. In the absence of such gradation, a sharp modulus mismatch would concentrate stresses and compromise interfacial stability. The native gradient mitigates this mechanical discontinuity, enabling smooth stress transfer, mechanical compatibility, and coordinated biological function. The osteochondral interface, therefore, represents not only a clinical challenge but also a stringent benchmark for evaluating the ability of engineered materials to reproduce continuous mechanical and compositional gradients (**Figure 1.11**).

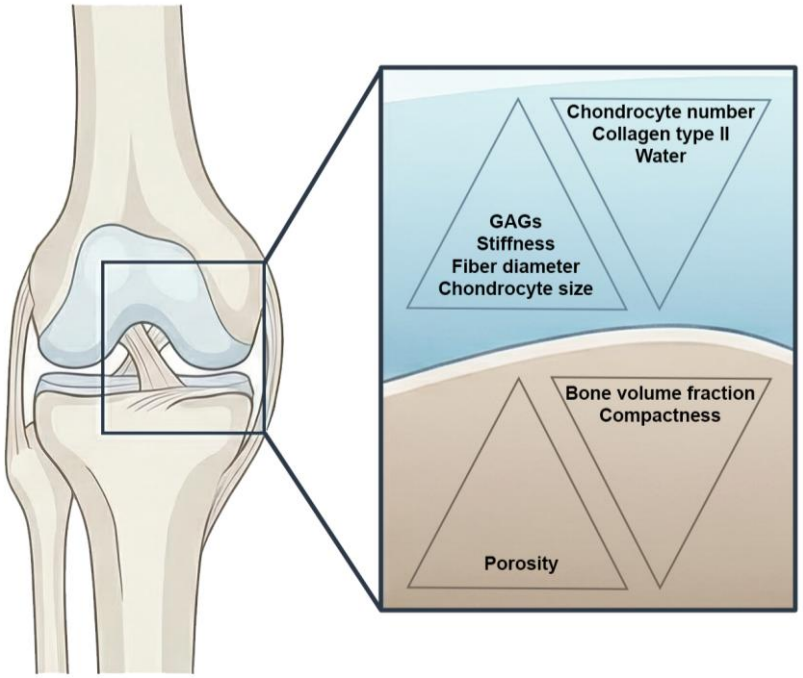

Figure 1.11 Schematic representation of the osteochondral unit highlighting microstructural and compositional gradients across cartilage and subchondral bone regions.

In this context, porous graded biomaterials offer a promising strategy to address the structural and biological complexity of interfacial tissues[92,93]. By integrating spatial variations in porosity, composition, and stiffness within a single construct, these systems aim to mimic native tissue gradients and promote region-specific biological responses. A graded scaffold may incorporate a cartilage-mimetic region characterized by higher water content, lower stiffness, and enhanced permeability, which progressively transitions into a mineralized, mechanically reinforced bone-like region. Tailored porosity across the construct supports chondrogenesis in the superficial layers and osteogenesis in the deeper regions, while reducing stress discontinuities at the interface. The realization of such architectures requires coordinated control over both material formulation and structural design. Microfluidic strategies enable tunable multiphase formulations and pore templating, while extrusion-based AM provides spatially controlled deposition and architectural design at the construct level[18]. By adjusting material formulation, fiber spacing, and

layer-by-layer deposition parameters, continuous or stepwise gradients can be reproducibly implemented within a single scaffold.

Despite the advances described above, several challenges continue to limit the widespread clinical translation of porous functionally graded biomaterials. Precise control over gradient continuity and reproducibility remains difficult, particularly when coupling variations in porosity, composition, and mechanical properties within a single construct. Small variations in processing parameters can significantly affect pore morphology and spatial material distribution. Moreover, the integration between microscale material regulation and macroscale architectural control is not yet fully optimized, limiting functional predictability. Addressing these limitations requires a systematic, interdisciplinary approach that bridges material design, microstructural control, and digital fabrication strategies. The experimental work presented in this thesis is developed within this framework, with the objective of establishing an integrated, reproducible platform for the fabrication of porous, functionally graded biomaterials targeting bone regeneration and tissue interfaces.

1.6.Scope and Structure of the Thesis

1.6.1. Research Objectives and Hypotheses

The objective of this doctoral thesis is to develop a microfluidic-integrated AM platform for the controlled fabrication of architected porous materials with spatially tunable porosity and composition. By integrating microfluidic droplet generation with extrusion-based 3D printing, the proposed strategy enables programmable regulation of spherical pore formation and material composition during fabrication. This work is grounded in the premise that advanced porous materials with predictable structural and functional properties require precise spatial control over pore architecture and composition across multiple length scales. Many natural materials, including

bone tissue, exhibit hierarchical porous architectures and compositional gradients that contribute to their exceptional mechanical and transport properties. Replicating such bioinspired structural complexity through synthetic manufacturing remains challenging. Conventional fabrication approaches often rely on stochastic templating strategies (e.g., bulk emulsification, gas foaming, or particulate leaching), which provide limited control over pore size distribution, spatial organization, and compositional gradients. In contrast, microfluidic technologies enable highly controlled multiphase flows and monodisperse droplets, allowing precise regulation of droplet size and generation dynamics. The central hypothesis of this work is that deterministic control of droplet generation and ink composition during AM enables the fabrication of porous materials with predictable structural and functional properties. Real-time modulation of droplet generation and ink composition is expected to yield architected materials with predictable pore-size distributions, spatially defined density variations, and compositional gradients. Compared with conventional fabrication methods, such control may improve structural predictability, mechanical reliability, and transport properties. The primary contribution of this thesis is the development of a microfluidic-assisted AM strategy enabling deterministic control over pore architecture and material composition during fabrication. Preliminary cell studies are included as a proof-of-concept demonstration of the potential applicability of the fabricated architectures in biologically relevant environments.

More specifically, this thesis tests the hypothesis through three research milestones. First, a microfluidic-assisted emulsion printing strategy is established to control pore formation at the microscale. Flow-focusing devices are used to generate monodisperse O/W emulsions with tunable droplet size

and dispersed phase volume fraction. These droplets serve as sacrificial templates for pore formation, yielding a spherical, highly controllable pore architecture. By integrating the microfluidic chip directly with an extrusion system and printing into a supporting bath, the rheological constraints traditionally associated with polymeric inks are decoupled from printability. This approach enables the fabrication of porous hydrogel constructs with controlled pore-size distributions, spatially modulated porosity, and both discontinuous and continuous density gradients. The emphasis of this stage lies in defining operational windows, ensuring process stability, and correlating emulsion parameters with resulting mechanical and structural properties (**Chapter 2**). Building upon the architectural control established in soft hydrogel systems, the second phase of the work translates these design principles to ceramic-based materials for the fabrication of mechanically robust porous scaffolds. Here, extrusion-based AM is employed to engineer hierarchical porous ceramic architectures suitable for load-bearing applications. Particular attention is devoted to the relationship between processing parameters, pore architecture, and mechanical performance, as well as to the adaptation of printing strategies to formulations suitable for sintering. While bone regeneration provides the application framework, the core contribution lies in developing a manufacturing route for architected porous ceramics with controlled structural integrity and predictable mechanical response (**Chapter 3**). Hence, the third technological advancement addresses compositional gradient control. A passive, highly-efficient microfluidic micromixer is integrated upstream of a flow-focusing junction, enabling the dynamic combination of multiple continuous-phase inks prior to droplet generation and extrusion. This configuration enables smooth, programmable compositional transitions during printing, extending the platform from density grading to true multimaterial gradient fabrication.

Quantitative evaluation of mixing efficiency, synchronization between flow modulation and spatial deposition, and simultaneous control of porosity and chemistry are systematically investigated. Preliminary biological assessments are included to demonstrate that spatial modulation of composition translates into localized functional responses; however, the primary contribution remains the development of a microfluidic printhead capable of real-time gradient engineering (**Chapter 4**).

Collectively, these developments establish a reproducible, scalable framework for the manufacturing of pFGMs. The thesis advances microfluidic-assisted AM from a droplet-generation technique to a comprehensive platform for multiscale material design, bridging microscale emulsion physical chemistry, mesoscale gradient control, and macroscale architectural structuring. Ultimately, this work aims to demonstrate the feasibility and robustness of a manufacturing strategy capable of producing architected porous materials with deterministic control over structure and composition. While the primary contribution lies in technological innovation and process engineering, the developed platform is conceived to serve as a foundation for future biomedical and tissue engineering applications, where precise spatial regulation of porosity and material gradients is essential.

1.6.2. Overview of the Thesis Chapters

The presented thesis is the result of different research projects already published or in submission. In particular:

- **Chapter 2** is readapted from the published original article in *Advanced Materials Technologies:*
  Marcotulli M. *et al.* Microfluidic 3D Printing of Emulsion Ink for Engineering Porous Functionally Graded Materials. *Advanced Materials Technologies* 2201244, 1–12 (2022), doi: 10.1002/admt.202201244

- **Chapter 3** is based on a work under preparation:
  Tirelli M.C. *et al.*, Microfluidic-Assisted Digital Manufacturing of Functionally Graded Porous Ceramics with Bone-Like Architecture

- **Chapter 4** is readapted from the published review article in *Materials Advances:*
  Tirelli M.C. *et al.*, Microfluidic-mixer assisted 3D printing of functionally graded multimaterial hydrogels for engineering complex tissue interfaces. *Materials Advances*, 2026, doi: 10.1039/d5ma01130b.

Chapter 2 - Microfluidic 3D printing of emulsion ink for engineering porous functionally graded materials

2.1.Introduction

Over the past two decades, growing attention toward structure–function relationships in natural materials has reinforced the importance of graded architectures. Nature achieves remarkable biomechanical and physiological performance by assembling a limited set of biopolymers and biominerals into hierarchically organized systems. Through controlled spatial arrangement of these building blocks, materials with properties far exceeding those of their individual components are obtained[94]. The key factor underlying such performance is the presence of gradients embedded within a multi-scale structural hierarchy. Depending on their biological function, natural systems integrate several types of gradients, including: (i) units characterized by chemical/constituent gradients, (ii) building blocks with a spatial distribution of cellular, fibrous, tubular units, (iii) structural units such as lamellas, fibrils, grains of varying dimensions down to the nanometers level, (iv) orientations of structural building units (e.g., successive dispositions of layers with different orientations of components)[95], (v) gradient interfaces (e.g., junctions), or (vi) integration of multiple gradients.

Despite their clear relevance, the controlled fabrication of graded spherical-based porous scaffolds remains challenging. Manufacturing strategies for pFGMs can be broadly classified into conventional and advanced approaches. Conventional techniques often rely on constructive assembly methods, in which prefabricated layers with distinct properties are sequentially stacked or bonded[6]. For example, porogens may be used to generate layers with varying

pore densities, which are subsequently assembled into a composite structure[96]. Alternative strategies, including centrifugation[97] or self-foaming followed by pyrolysis[96], have also been employed to introduce gradients. However, these methods typically offer limited precision and restricted control over gradient continuity and spatial resolution. AM technologies have introduced a more versatile route for pFGM fabrication. In particular, extrusion-based systems equipped with multiple nozzles have demonstrated the capability to deposit distinct materials within a single construct, enabling spatial modulation of composition and texture[98–100]. Such strategies have been extensively applied to thermoplastic and ceramic systems. Conversely, hydrogel-based inks present additional constraints. Their relatively low viscosity and limited structural stability often restrict the fabrication of geometrically complex architectures, especially those involving concave surfaces, overhangs, or simultaneous integration of multiple gradients.

In this context, we introduce a microfluidic-assisted 3D printing strategy for depositing O/W emulsions within a suspending medium. By generating the emulsion directly within a flow-focusing microfluidic device and depositing it onto a support bath, it is possible to fabricate complex hydrogel architectures incorporating spatial variations in density and composition. Crucially, this approach decouples ink rheology from structural fidelity, enabling the use of low-viscosity precursor solutions while maintaining high geometric control during printing.

2.2.Materials and methods

2.2.1. Materials

Dextran (from Leuconostoc spp., Mr ~ 70000), gelatin (from porcine skin, Type A, 300 Bloom), HA (nanopowder, <200 nm particle size), dimethyl sulfoxide (DMSO), glycidyl methacrylate (GMA), methacrylic anhydride (MA), cyclohexane (≥99.5%), pluronic F-68, 2-hydroxy-4′-(2-hydroxyethoxy)-2-methylpropiophenone (Irgacure 2959), fluorescent yellow-green latex beads (amine-modified polystyrene), hydrochloric acid (HCl), tin(II) chloride ($SnCl_2$), phosphate buffered saline (PBS) and Hanks′ Balanced Salt solution (HBSS) were purchased from Sigma Aldrich. 4-Dimethylaminopyridine (DMAP, 99%) was obtained by Acros Organics. Agarose was purchased from Carbosynth.

2.2.2. Synthesis of Dextran Methacrylate

Dextran methacrylate (DexMA) was synthesized following a previously published protocol[47]. Dextran (10 g) was dissolved in 90 mL of DMSO under stirring. DMAP (2 g) was added after dissolution in DMSO, followed by the addition of GMA (4 mL), corresponding to approximately 50% molar substitution relative to dextran repeating units. The reaction was conducted at room temperature (RT) under mild stirring (100 rpm) for 48 h in dark conditions. Upon completion, an equimolar amount of HCl was introduced to neutralize DMAP and terminate the reaction. The solution was transferred into dialysis tubing (Molecular Weight Cut-Off (MWCO) 1 kDa) and dialyzed against deionized water for five days until stable conductivity (18 MΩ·cm) was reached. The purified product was frozen at −80 °C, freeze-dried, and

stored at 4 °C. The degree of substitution (DS) was determined by ^1H-NMR spectroscopy.

2.2.3. Synthesis of Gelatin Methacryloyl

Gelatin Methacryloyl (GelMA) was prepared according to a documented method[101]. Gelatin was dissolved at 10% (w/v) in PBS at 50 °C. Methacrylic anhydride (0.8 mL per gram of gelatin) was added dropwise under continuous stirring (500 revolutions per minute rpm), and the reaction was allowed to proceed for 3 h. The reaction mixture was dialyzed against deionized water at 50 °C using dialysis tubing (MWCO 1 kDa) for five days until nominal conductivity was achieved. The resulting solution was frozen at −80 °C, lyophilized, and stored at 4 °C.

2.2.4. Supporting bath for 3D printing

An agarose-based fluid gel was prepared as a temporary support medium following an established procedure[102]. Briefly, agarose (0.5 g) was dispersed in 100 mL of deionized water to obtain a 0.5% (w/v) suspension. The solution was sterilized by autoclaving at 121 °C for 20 minutes and subsequently stirred continuously (700 rpm) for 12 h during cooling to RT, yielding a homogeneous fluid-gel structure. The supporting bath was stored at RT until use.

2.2.5. Fabrication of polycarbonate microfluidic chip

The flow-focusing microfluidic chip was fabricated from 5 mm-thick polycarbonate sheets using computerized numerical control (CNC) micro-milling (MSG402, ErgWind, Poland). The device featured: i) Continuous and

dispersed phase inlets: 250 μm width; ii) Orifice width: 100 μm; iii) Outlet channel width: 500 μm; iv) Channel depth: 100 μm; v) 25G needle coupled to outlet. After milling, substrates were sonicated in isopropanol for 30 minutes and thermally bonded using a hot press at 130 °C for 30 minutes, followed by controlled cooling to RT. To improve compatibility with the organic dispersed phase, the internal microchannels were treated with a 20% (w/w) $SnCl_2$ solution in ethanol[103]. The solution was infused at 20 mL/h for 2 h at 60 °C. The device was then thoroughly rinsed with deionized water prior to use.

2.2.6. Microfluidic emulsion

O/W emulsions were generated using the flow-focusing microfluidic chip. Cyclohexane was used as the dispersed organic phase, while the continuous aqueous phase consisted of 20% (w/v) DexMA, 15% (w/v) Pluronic F-68, and 1% (w/v) Irgacure 2959. Irgacure 2959 served as a photoinitiator to enable crosslinking of methacrylated polymers following deposition. The whole experiment was carried out in low light to avoid premature cross-linking of the radical initiators. Both phases were filtered through 0.22 μm syringe filters prior to loading into 1 mL syringes to prevent channel obstruction. Emulsions were produced under low-light conditions to avoid premature photopolymerization. The flow-focusing chip was used to generate a series of emulsions, with the flow rates of the two phases controlled using neMESYS (Cetoni GmbH) microfluidic pumps. The total flow rate was maintained at 20 μL/min. Dispersed-phase volume fractions (φD) in the range 0.2–0.8 were achieved by adjusting the relative flow rates of continuous and dispersed phases.

2.2.7. Image analysis (FastCAM) and emulsion characterization

The formation of O/W emulsions within the flow-focusing chip was monitored using a high-speed camera (Photron FASTCAM Mini UX) operating at 500 frames per second. The imaging system was coupled to an inverted optical microscope (Zeiss Observer.Z1) equipped with a 5× objective. Recorded videos were analyzed frame-by-frame using ImageJ software. Droplets generated at different dispersed-phase volume fractions (φD) were quantified using the "Particle Analyze" function to extract droplet area and equivalent diameter. For each condition, droplet size distributions were determined from at least 50 measurements.

2.2.8. Emulsion 3D printing of cylindrical porous scaffolds and complex geometries

Emulsion-based inks were deposited using a custom-built 3D printing system integrating the flow-focusing microfluidic printing head (ff-MPH) with three microfluidic pumps (neMESYS, Cetoni GmbH) controlled through Qmix software (Qmix Elements). The printer operated on a Cartesian linear-axis system driven by a motorized stage (Micos), enabling synchronized extrusion and spatial positioning. Standard cylindrical scaffolds were designed using Fusion 360 (Autodesk) and printed inside an agarose fluid-gel support bath to ensure structural confinement during deposition. To evaluate gradient fabrication capabilities, four scaffold architectures were produced: three with axial gradients (2, 4, and alternating layers) and one with a radial gradient. Three-dimensional structures that were impossible to print in air, with an overhang > 45°, were printed using porous fibers in agarose fluid-gel at a print speed of 3.3 mm/s (F200). The complex geometries were downloaded from

the Thingiverse repository. The Slic3r programme, which converts the stereolithography interface format (STL) to G-code, was then used to slice the models with a 0.2 mm slice thickness. To automate the modulation of porosity within a single construct, a custom script was implemented to dynamically adjust pump flow rates during printing. This allowed the generation of controlled dispersed-phase volume fractions (φD) across predefined regions of the scaffold. Fluorescent dyes were incorporated into selected hydrogel formulations to facilitate visualization of density variations within printed constructs.

2.2.9. Scaffolds cross-linking and purification

After deposition within the agarose support bath, printed structures were exposed to ultraviolet (UV) irradiation (λ = 365 nm) for 20 minutes to initiate crosslinking of the external aqueous phase. Constructs were manually retrieved from the support medium and immersed in DMSO to extract the internal cyclohexane phase. Oil removal was achieved by repeated DMSO washes over 3 days, followed by distilled water washes until nominal conductivity was reached. Purified scaffolds were subsequently frozen at −80 °C and lyophilized for further characterization.

2.2.10. Scanning Electron Microscopy

Lyophilized scaffolds were sectioned and mounted onto aluminum stubs using conductive carbon tape. Samples were sputter-coated with chromium to enhance conductivity. Morphological analysis was performed using a high-resolution field-emission scanning electron microscope (SEM) (HR-FESEM, AURIGA Zeiss) operated at 1.5 kV. Images were acquired at 145× magnification to evaluate pore morphology and internal architecture.

2.2.11. Microcomputed Tomography

To assess the internal microstructure of 3D-printed scaffolds, microcomputed tomography (microCT) was performed using an Xradia MicroXCT-400 system with the following parameters: 40 kV, 10 W, 0.18° rotation step over an angle interval of 184°. Prior to scanning, purified samples were partially dehydrated in a 50:50 (v/v) water/ethanol solution and subsequently immersed in sunflower oil to enhance radiographic contrast. Scanning was conducted at RT (25 °C) under atmospheric pressure. Three-dimensional reconstructions were generated from 2D image stacks using the 3D Viewer plugin in ImageJ.

2.2.12. Optical coherence microscopy

Morphological characterization of 3D FGM structure in hydrate conditions was performed using high-resolution optical coherence microscopy (OCM)[104]. A custom-designed spectral OCM system used a commercial femtosecond laser (Fusion Femtolasers, Austria) with a central wavelength of 795 nm and a 130 nm bandwidth, yielding an axial resolution of approximately 2.2 μm. A fiber-based Michelson interferometer with a 75/25 splitting ratio was used. The light reflected from the sample was combined with light reflected from the mirror in the reference arm, and the resulting interference signal was recorded with a high-speed 2048-pixel line-scan camera spectrometer (Cobra-S 800, Wasatch Photonics, USA).

A 4x microscope objective (Olympus Plan Fluorite, NA = 0.13, WD = 17.3 mm) was used for sample illumination. The pupil was illuminated with a 6 mm (1/e2) Gaussian beam, yielding a lateral resolution of 4.5 μm and a confocal parameter f ~100 μm. The sample was illuminated with an average optical power of 0.5 mW. Lateral laser beam scanning was performed using a

pair of galvoscan scanners (Thorlabs Inc., USA). 3D volumes typically extending over an area of 1.0 mm × 1.0 mm × 1 mm were acquired with a pixel density of 1024 × 1024× 2048 pixels for X, Y and Z-axes, respectively. The imaging depth, limited by light penetration and multiple scattering, was evaluated at 800 μm. Specific stand-alone software designed in LabVIEW, enabled the monitoring of a scanning protocol, coordination of camera and scanners, and data processing, including such steps as spectrometer calibration, numerical dispersion compensation, and spectral shaping. Data analysis allowed the volumetric recreation of the fine structure of investigated porous materials.

2.2.13. Bright-field imaging

The morphological structure of the laid emulsion fibres was investigated using a laser scanning confocal microscope (Olympus IX83). Imaged fibres with a fluorescently labelled disperse phase were visible under brightfield microscopy, with the fluorescent signal varying along the imaging direction. Prior to printing, the external phase was labelled with fluorescent yellow-green latex beads (λ_{ex} ~470 nm e λ_{em} ~505 nm). The printing was carried out in a 3-mm thick agarose fluid gel within a 700 μl volume chamber. A single fibre was deposited and analysed for printing fidelity.

The analysis was performed on non-purified scaffolds: porous cylinders were obtained, cross-linked, collected from the supporting bath and then washed with DW to remove agarose fluid-gel residues. The acquired images were stitched together with ImageJ software using the Grid/Collection stitching function.

2.2.14. Rheological measurements of emulsion inks

Rheological measurements were performed using a rotational rheometer (Anton Paar MCR 302) equipped with a 25 mm cone-plate geometry (1° cone angle) at 25 °C. The following materials were characterized: agarose fluid-gel support bath, continuous phase (DexMA + Pluronic F-68) and, emulsions at various dispersed phase volume fractions (φ_D = 0.2, 0.3, 0.4, 0.6, 0.7, 0.8). The shear viscosity behaviour of the samples was assessed by applying a share rate from 1 to 100 s^{-1}.

2.2.15. Mechanical testing of 3D printed emulsion scaffolds

The compressive mechanical behavior of the fabricated scaffolds was evaluated using a dynamic mechanical analyzer (DMA Q800, TA Instruments, New Castle, DE, United States). Tests were conducted on fully hydrated cylindrical samples (diameter: 7 mm; height: 7 mm) at 25 °C. Density-graded scaffolds and homogeneous control samples (φD = 0.2, 0.3, 0.4, 0.6, 0.7) were immersed in distilled water prior to testing. Sample dimensions were measured using a digital caliper and specimens were positioned between parallel compression plates. A preload force of 0.001 N was applied to ensure contact. Compressive strain was applied at 2.5% min^{-1} up to 30% deformation. The unloading phase was performed at 5% min^{-1}. Stress–strain curves were recorded for the entire loading–unloading cycle. Young's modulus was determined from the slope of the initial quasi-linear region corresponding to 0–5% strain.

2.2.16. *In vitro* degradation test

To assess hydrolytic stability of DexMA scaffolds, scaffolds were subjected to an *in vitro* degradation test in HBSS at 37 °C. Purified hydrogels were initially incubated in HBSS for 24 h, dried, and weighed to determine the initial dry mass (W_0). Samples were then immersed in 1 mL HBSS and incubated at 37 °C for up to 14 days. The medium was refreshed every three days. At predefined time points, samples were collected, dried, and weighed (W_t). The percentage weight loss was calculated according to:

$$Weight\ remaining\ (\%) = \frac{W_t}{W_o} \times 100 \qquad \textbf{(Eq. 2.1)}$$

2.2.17. Mass swelling ratio

Studies were carried out on DexMA hydrogels to investigate the mass swelling ratio. The scaffolds were weighed before ($m_{initial}$) and after crosslinking ($m_{initial,t0}$) to obtain their initial wet mass. The samples (n = 3) were freeze-dried to determine their dry mass ($m_{dry,t0}$). The value of the *actual macromer fraction* was determined as follows:

$$actual\ macromer\ fraction = \frac{m_{dry,t0}}{m_{initial,t0}} \textbf{ (Eq. 2.2)}$$

A further three samples were incubated for 24 hours in HBSS at 37 °C to allow swelling. After 24 hours, the samples were weighed ($m_{swollen}$) and then lyophilised and weighed (m_{dry}). The mass swelling ratio (q) was subsequently evaluated using Equation (2.3)[105]:

$$q = \frac{m_{swollen}}{m_{dry}} \textbf{ (Eq. 2.3)}$$

The experiment was replicated for all four types of scaffolds fabricated in this work (2, 4, alternate layers and radial FGMs).

2.2.18. Statistical analysis

Statistical analysis was performed using GraphPad Prism (GraphPad Software Inc., La Jolla, CA). Data normality was evaluated using the D'Agostino–Pearson test. Depending on the experimental design, one-way or two-way ANOVA was applied. Statistical significance was defined as $p < 0.05$. Sample size (n) is specified within figure captions.

2.3.Results and Discussion

2.3.2. Exploring operational ranges and rheological properties of microfluidic emulsion inks

A common strategy for fabricating porous scaffolds involves using biphasic systems, such as emulsions or foams, which serve as sacrificial templates. Thus, the use of biphasic inks in 3D printing has consisted of the preliminary formation of the emulsion/foam, its loading into a cartridge or reservoir, and subsequent deposition[106]. However, this method presents intrinsic limitations. Biphasic inks must simultaneously satisfy two competing requirements: sufficient shear-thinning behavior to allow extrusion and adequate structural integrity to preserve shape upon deposition. As a consequence, only a narrow range of external phase compositions and dispersed-phase volume fractions can be effectively processed. Moreover, the rheological behavior of concentrated emulsions is strongly influenced by both the dispersed-phase fraction and droplet interactions, making a priori prediction of printability challenging and often requiring extensive empirical optimization. Decoupling

the rheological characteristics of the biphasic ink from its printability would therefore significantly expand the accessible operational window and enable greater flexibility in pFGMs design. Approaches such as in-air microfluidic deposition have demonstrated the potential to modify fluid streams immediately prior to deposition. For instance, Visser and co-workers[107] reported encapsulation of internal phases during the flight of liquid jets in air. Nevertheless, this method requires droplet formation at a defined distance from the substrate, leading to high impact velocities and potentially reducing printing resolution.

To circumvent the resolution loss and high-impact velocities inherent in in-air jetting, the strategy proposed here is based on the direct deposition of an O/W emulsion generated within a flow-focusing microfluidic chip and extruded into a supporting medium. This configuration allows the emulsion to be deposited in close proximity to the substrate, minimizing structural perturbations and enabling the fabrication of geometrically complex architectures. The overall fabrication workflow is illustrated in **Figure 2.1**.

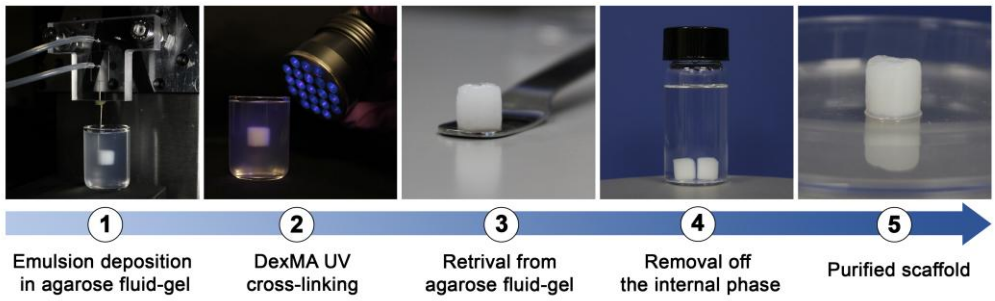

Figure 2.1 Sequence of steps illustrating the process of scaffold fabrication and purification.

The flow-focusing microfluidic printing head (ff-MPH) is designed to generate O/W emulsions with tunable properties and directly integrate them

into a 3D printing system (**Figure 2.2a**). The device enables modulation of (i) the chemical composition of the matrix, (ii) the density of the printed material through control of dispersed-phase volume fraction (φ), and (iii) the local porous architecture in a continuous or discontinuous manner along the depth or radius of the construct.

To define the operational window of the ff-MPH, preliminary experiments were conducted using a single aqueous continuous phase (DexMA/Pluronic F-68) and cyclohexane as the dispersed phase. Flow rates ranging from 5 to 30 μL/min were explored to identify conditions that enabled stable, continuous O/W emulsion formation. A total flow rate of 20 μL/min was found to provide steady droplet generation and reproducible operation, while simultaneously offering a broad range of accessible droplet diameters ($D_{droplet}$) and dispersed-phase volume fractions (φ). As shown in **Figure 2.2b**, by maintaining the total flow rate constant and adjusting the relative flow rates of the two immiscible phases, emulsions with φ values between 0.2 and 0.8 were reproducibly generated. Increasing the dispersed-phase flow rate resulted in both larger droplet diameters and higher φ values (**Figure 2.2c,d**), in agreement with previously reported behavior in flow-focusing systems[47].

Following identification of stable operating conditions, a comprehensive rheological characterization was performed on the continuous phase and the corresponding emulsions (**Figure 2.2e**). The DexMA/Pluronic F-68 precursor solution exhibited near-Newtonian behavior within the investigated shear rate range. In contrast, emulsion inks demonstrated progressively stronger shear-thinning behavior as φ increased. This transition can be attributed to the increase in total interfacial area and droplet–droplet interactions, which are known to govern the flow behavior of concentrated emulsions.[108]To

effectively decouple ink rheology from printability, an agarose-based fluid-gel was formulated as a temporary support medium. The agarose fluid-gel exhibits self-healing and shear-thinning characteristics, allowing local displacement during nozzle movement followed by rapid structural recovery. The efficacy of the agarose support bath was corroborated by rheological data indicating that the agarose fluid-gel exhibited more pronounced pseudoplasticity than the biphasic inks, facilitating rapid shear-thinning and structural recovery necessary for high-fidelity submerged extrusion (**Figure 2.2e**). Optical microscopy revealed a slurry-like microstructure, with spiky hydrogel microparticles distributed homogeneously throughout the medium (**Figure 2.2f**). During printing, these microparticles can be locally displaced by the extruded filament and subsequently reorganize to physically confine the deposited structure[101,102,105]. This mechanism ensures positional stability of the printed pFGMs while allowing the use of low-viscosity emulsion inks.

Overall, the combination of microfluidic emulsion generation and suspension-based deposition defines a broad and controllable operational window for the fabrication of graded spherical-based porous FGMs with tunable density and pore size.

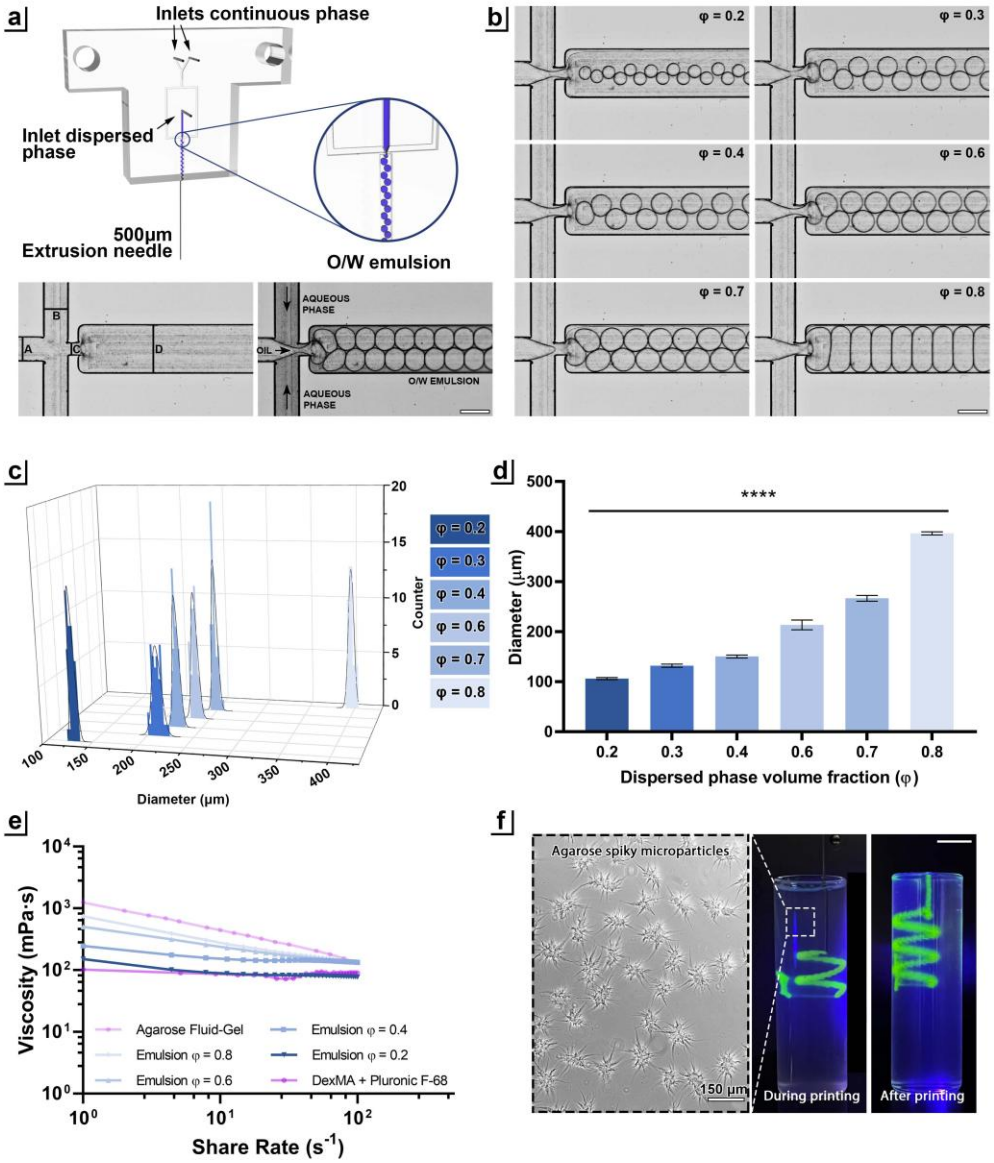

Figure 2.2 Operational range exploration for emulsion ink production. **a)** Schematics of the ff-MPH used to generate functionally graded O/W emulsions (values of characteristic dimensions of the microfluidic device are reported in the experimental section). **b)** Microfluidic production of the emulsions at different volume fractions of the dispersed phase ($0.2 < \varphi < 0,8$). **c,d)** Droplet size distributions (left) and resulting average droplet diameters (right) measured for the selected values of φ. **e)** Rheological characterization of the agarose fluid-gel, emulsion inks, and DexMA continuous phase. **f)** (left) Micrograph of the agarose fluid-gel diluted 1:100, revealing its slurry nature: spiky hydrogel microparticles, homogeneous in size, can be appreciated. (right) Stability of emulsion ink in agarose fluid-gel during and after 3D printing. Scale bars: (a,b) 300 µm, (f) 5 mm. Statistical significances were assessed by one-way ANOVA. Mean ± S.D. n=50, ****p<0.0001.

2.3.3. Emulsion ink printing in an agarose fluid-gel

The agarose fluid-gel acted as a temporary supporting medium during 3D deposition. Owing to its viscoelastic and shear-thinning behavior, the O/W emulsion generated within the ff-MPH could be directly extruded into the bath and spatially confined without collapse, as schematically illustrated in **Figure 2.3a**. The emulsion filament, once deposited, remained immobilized within the support matrix, which rapidly recovered its structure after local shear induced by nozzle movement. Emulsion inks were printed using the custom 3D printer equipped with the ff-MPH. The generation of O/W emulsions inside the microfluidic chip was precisely synchronized with the extrusion and spatial translation of the printhead. This coordination ensured continuous deposition of emulsion fibers, with the external aqueous phase encapsulating the dispersed cyclohexane droplets, preventing their diffusion into the surrounding support medium. **Figure 2.3b** (top) shows laser scanning confocal microscopy (LSCM) images of single deposited struts produced at different φ values. The droplet size and internal organization within the filament reflected the selected dispersed-phase volume fraction. Notably, direct deposition into the agarose bath compensated for the system dead volume, enabling sharp transitions in φ during layer-by-layer printing. Interestingly, cyclohexane droplets tended to cluster within laid struts upon deposition in the support medium, eventually forming long threads of adjacent droplets (**Figure 2.3b**). Following UV-induced crosslinking of the external phase, the purification protocol was applied to remove the internal organic phase[109–111]. Efficient extraction of cyclohexane required the use of a polar aprotic solvent (e.g., DMSO) miscible with both the organic phase and water. Multiple DMSO washes ensured complete oil removal, followed by extensive washing in distilled water to restore physiological conditions. This protocol

has previously demonstrated the ability to yield biocompatible porous structures[112]. To assess the capability of the ff-MPH to fabricate graded architectures, cylindrical scaffolds incorporating controlled density variations were printed (**Figure 2.3c**). Three discontinuous pFGM configurations (2-layer, 4-layer, and alternate-layer axial gradients) and one continuous radial gradient architecture were generated. These constructs demonstrated the system's versatility in patterning both discrete and continuous variations in φ.

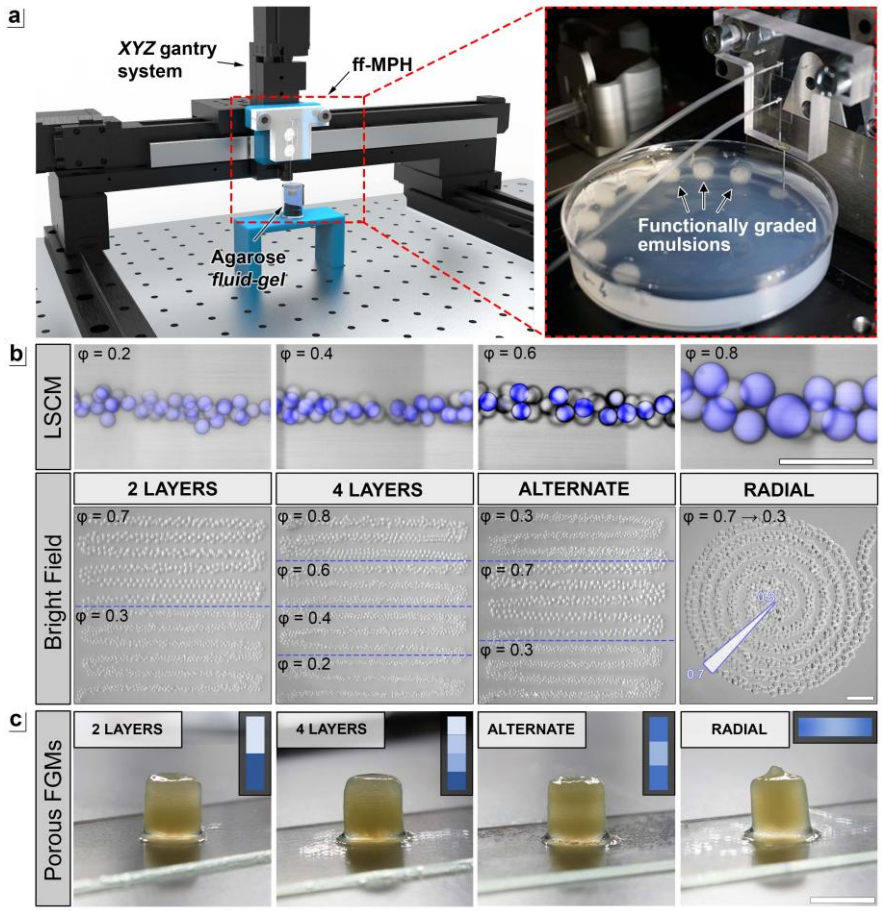

Figure 2.3 3D printing of porous FGMs. **a)** Schematics of the 3D printing setup used to generate and 3D print emulsion inks. **b)** (top) Laser scanning confocal microscopy (LSCM) micrographs showing droplet size and organization within single deposited struts at different values of φ. (bottom) Illustrative 3D printed single ZX (2, 4, alternate layers) and XY (radial) cross-sectional layers for easier appreciation of internal FGM structure. **c)** Porous cylinders characterized by discontinuous (2 layers, 4 layers, alternate) and continuous (radial) FGM architectures. Scale bars: b) 500 mm, c) 7 mm.

SEM analysis confirmed that the clustered droplet organization observed in confocal imaging was preserved after lyophilization (**Figure 2.4a**). The pore morphology reflected the initial $D_{droplet}$ distribution and φ selected during printing. Despite buoyancy-induced droplet rearrangement, the deposition process remained stable and reproducible across conditions. Mechanical characterization was subsequently performed to evaluate the influence of φ and gradient architecture on compressive behavior (**Figure 2.4b,c**).

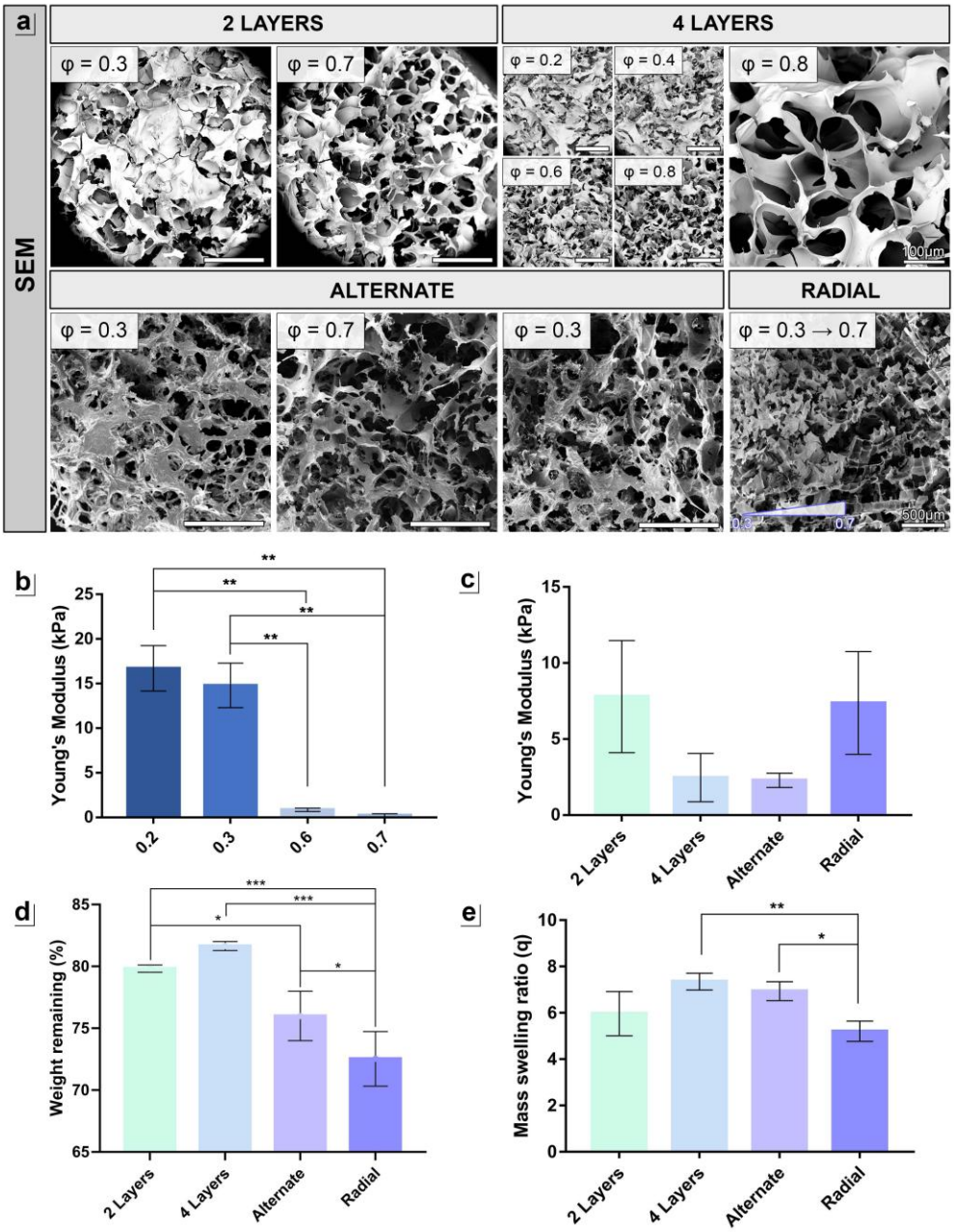

Figure 2.4 Morphological characterization of 3D printed porous FGMs. **a)** SEM images of the porous FGMs. **b-c)** Variation of Young's moduli in control samples characterized by a single porosity and in the manufactured porous FGMs. **d)** Weight loss and **e)** swelling ratio of FGMs. Scale bars: 300 µm. One-way ANOVA assessed statistical significance. Mean ± S.D. n=3, *p<0.05, **p<0.01, ***p<0.001.

Stress–strain curves of homogeneous scaffolds (**Figure 2.5a**) revealed a clear dependency on φ, for instance, lower φ samples (denser structures) exhibited higher Young's moduli, with stress–strain traces shifted toward higher stress values. For φ = 0.2 and 0.3, the curves displayed two distinct linear regions. The initial region (up to approximately 7% strain) corresponded to elastic deformation of pore walls and was used to calculate Young's modulus. Beyond this threshold, a steeper slope emerged, likely associated with pore buckling and bulk hydrogel deformation. In higher φ samples (0.6 and 0.7), pore deformation and buckling dominated the mechanical response from early stages of loading. Young's modulus values for constant φ scaffolds are reported in **Figure 2.4b**. Samples prepared at φ = 0.8 exhibited mechanical properties below the detection limit of the DMA apparatus and therefore could not be quantified.

pFGM samples exhibited mechanical responses distinct from homogeneous counterparts. The two-layer scaffold (φ = 0.3/0.7) showed three regions of varying slope (**Figure 2.5b**). The initial deformation (up to ~5% strain) was governed by the lower-density layer (φ = 0.7). At higher strain levels (~20%), a steeper slope emerged, consistent with engagement of the denser φ = 0.3 region. In contrast, the four-layer architecture exhibited a smooth and continuous transition in slope without abrupt changes. The similarity in pore volumes between adjacent layers likely led to coupled deformation behavior, resulting in a gradually evolving stress-strain profile.

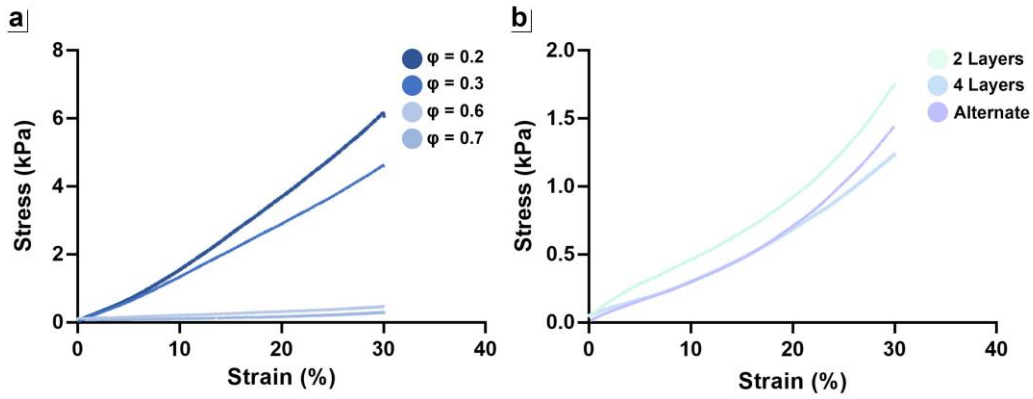

Figure 2.5 Compression mechanical characterization of 3D printed porous FGMs. Stress-strain plots: **a)** control homogeneous samples prepared with a single porosity value and **b)** FGM samples.

Given that these pFGMs consist of relatively soft hydrogel matrices, degradation and swelling behavior represent critical functional parameters. A 14-day *in vitro* degradation study in HBSS at 37 °C was conducted (**Figure 2.4d**). All 3D-printed architectures maintained structural integrity throughout the test period, confirming hydrolytic stability under physiological conditions. However, alternate-layer and radial pFGMs exhibited slightly higher weight loss than 2-layer and 4-layer configurations ($p < 0.01$), suggesting that the gradient distribution influences degradation kinetics. Swelling behavior was evaluated by measuring mass swelling ratio (q) (**Figure 2.4e**). DexMA hydrogels, characterized by a degree of substitution (DS) of 35%[113,114], exhibited moderate swelling, consistent with previously reported trends[105,115], in which swelling inversely correlates with DS. Additionally, q increased with increasing φ, in agreement with observations that emulsions with higher dispersed-phase fractions tend to exhibit enhanced swelling capacity. The results of this work supported the observation of Bjerregaard and co-workers[116], who reported that emulsions with elevated φ have a higher swelling ability compared to emulsions with small φ. To verify printing

fidelity and internal architectural resolution, microCT and OCM analyses were performed (**Figure 2.6**). MicroCT enabled volumetric reconstruction of dehydrated scaffolds, while OCM provided high-resolution imaging of hydrated structures.

Three-dimensional reconstructions, shown in **Figure 2.6**, confirmed accurate reproduction of programmed pFGM architectures, with clear distinction between high-porosity (low-density) and low-porosity (high-density) regions. As expected, zones characterized by higher φ exhibited larger pore sizes and increased pore interconnectivity. Radial constructs demonstrated particularly strong preservation of the designed gradient blueprint, highlighting the ff-MPH system's capacity to precisely pattern spatial variations in porosity within complex geometries.

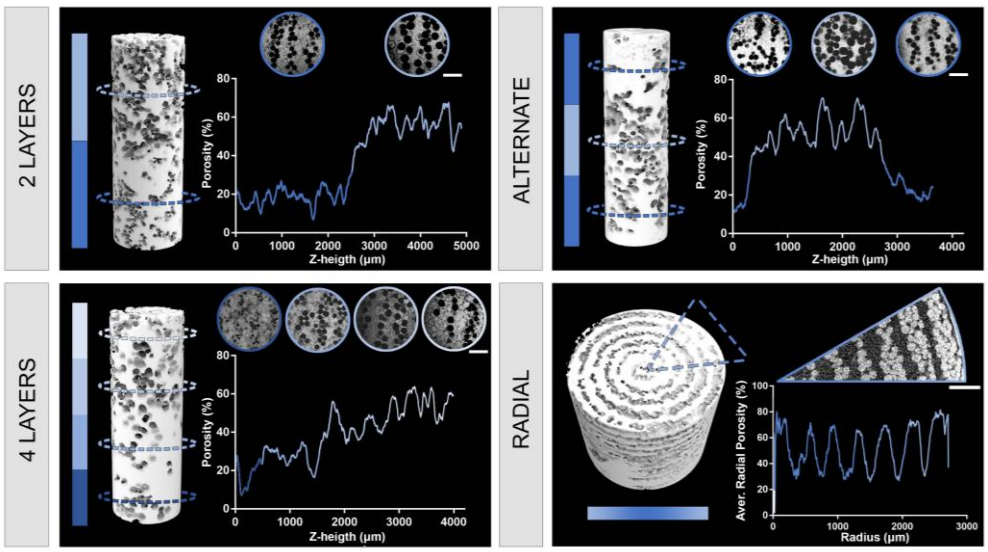

Figure 2.6 Internal topographic analysis via microCT and OCM. Three-dimensional reconstruction of porous FGMs from an image stack acquired by microCT; Horizontal sections of the scaffold acquired by OCM. For each FGM, a spatial porosity analysis was estimated from microCT volumetric reconstruction. Scale bars: (2 layers – Alternate – 4 layers) 300 mm, (Radial) 500 mm.

2.3.4. 3D printing complex FGM architectures in agarose fluid-gel

Fabricating geometrically complex hydrogel architecture remains particularly challenging when low-viscosity or biphasic inks are used. In extrusion-based systems, sufficient viscoelasticity is generally required to preserve filament shape upon deposition. This limitation becomes even more pronounced when printing emulsion inks, where the dispersed phase may destabilize filament integrity and induce structural collapse. To overcome these constraints, thixotropic and self-healing support media have been proposed, including gelatin-based FRESH systems[72], Laponite suspensions[115], and agarose fluid-gels[105]. Our agarose fluid-gel support bath enabled the stable deposition of O/W emulsion inks generated by the ff-MPH, alongside the fabrication of highly complex 3D geometries[109]. Using this configuration, we successfully printed architectures characterized by pronounced overhangs exceeding 45°, including gyroid cylinders, inverted pyramids, spheres, helices, and stair-like structures (**Figure 2.7a**). The supporting medium physically confined the extruded filaments during deposition and recovered its structure immediately after nozzle displacement, ensuring dimensional stability prior to crosslinking. To further demonstrate the system's versatility, additional complex geometries were fabricated (**Figure 2.8**), including a chess knight and a pawn, the sorting hat from Harry Potter, St. Peter's dome, a DNA helix, and a femoral epiphysis model. In all cases, the final printed constructs accurately reproduced the digital blueprints, including intricate overhanging details that would not be achievable via direct air extrusion.

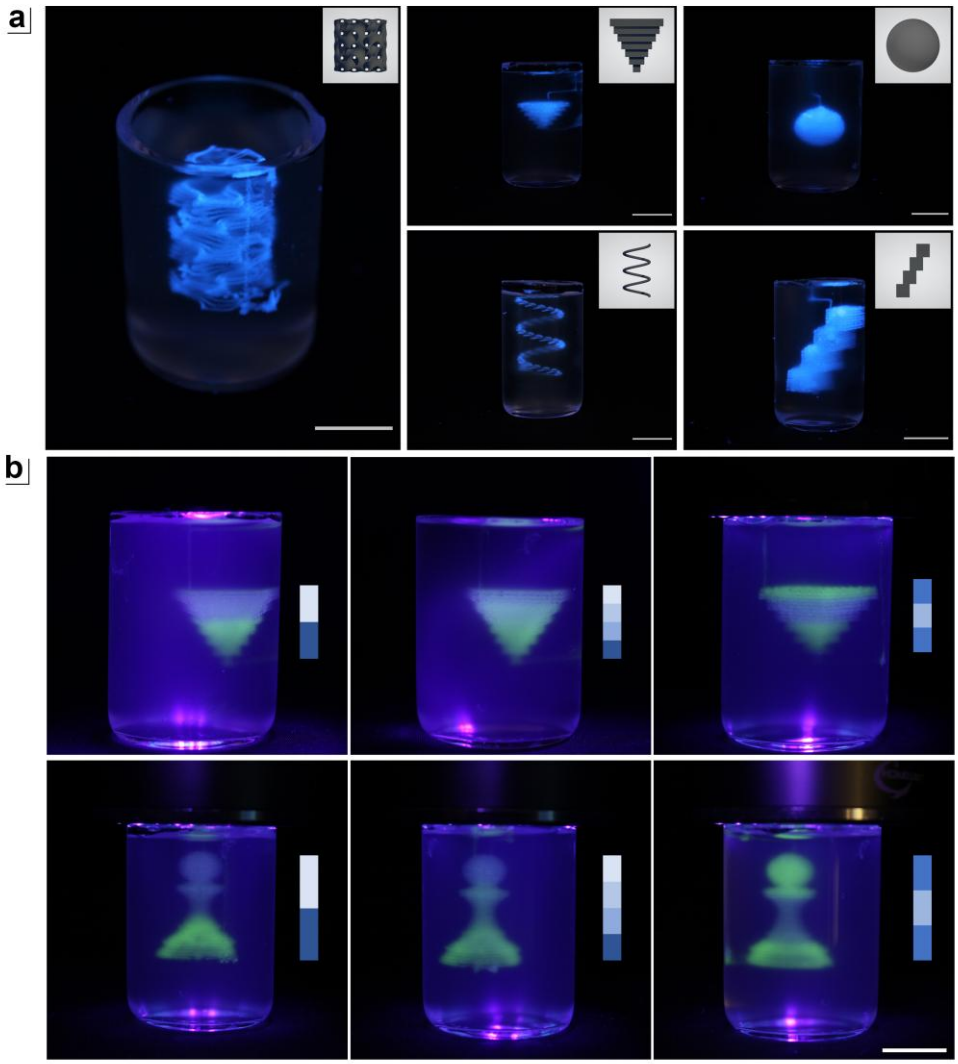

Figure 2.7 3D printing of complex FGM in fluid-gel **a)** 3D printing of complex architectures in fluid-gel. Various exemplary complex 3D structures printed in agarose fluid-gel: gyroid cylinder, inverted pyramid, sphere, helix, and stairs. **b)** 3D printing of complex FGM architectures in fluid-gel. Density gradient complex 3D geometries printed using a fluorescent dye in the continuous phase: the green signal corresponds to more dense areas (low porosity), while light green and pale signals indicate less dense zones (high porosity). Scale bars: a) 5 mm, b) 10 mm.

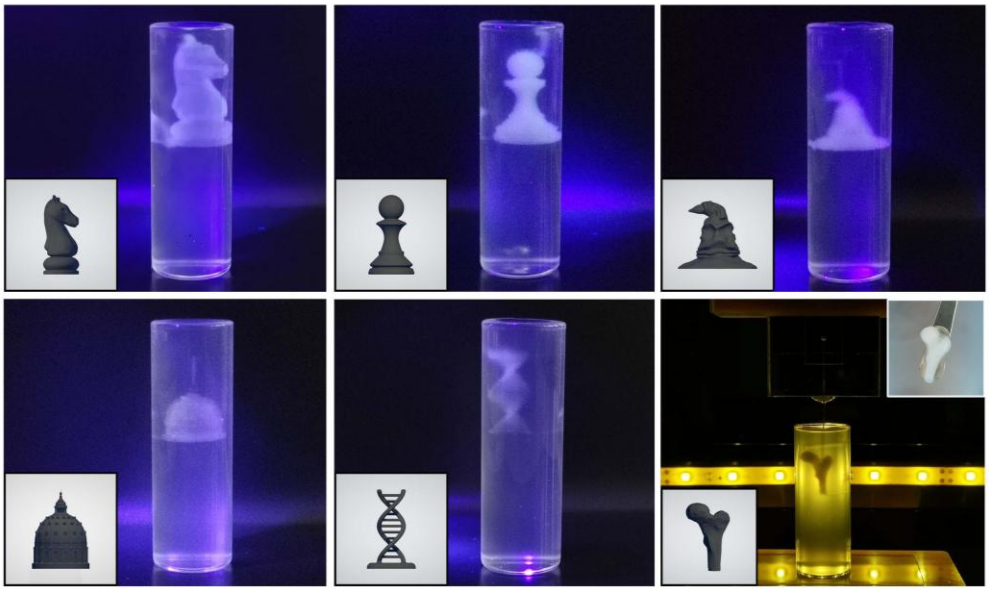

Figure 2.8 3D printing of complex architecture in fluid-gel. **a)** Various exemplary complex 3D structures 3D printed in agarose fluid-gel: chess knight and pawn, the sorting hat from Harry Potter, St. Peter's dome, DNA helix, and a reproduction of a femur epiphysis. Scale bars: 500 mm.

Importantly, architectural complexity did not compromise control over local porosity. To provide direct visual evidence of density modulation, selected scaffolds were printed using fluorescently labeled continuous phases (**Figure 2.7b**). Regions exhibiting stronger fluorescence corresponded to lower porosity (lower φ), whereas lower fluorescence intensity indicated higher porosity. The clear spatial transitions observed confirmed precise regulation of φ during 3D deposition, independent of geometric complexity.

Previous studies have demonstrated gradient fabrication using valve-based flow-focusing systems[18] fabricated from PDMS. However, such devices have inherent limitations, particularly regarding solvent compatibility. PDMS swelling in the presence of organic solvents restricts the use of hydrophobic monomers or organic dispersed phases, limiting the generation of emulsion templates. In contrast, the polycarbonate-based ff-MPH employed here allows

stable processing of cyclohexane-based O/W emulsions, expanding the range of printable formulations. Beyond density modulation, the ability to vary matrix composition further enhances the platform's versatility. As a proof-of-concept, GelMA was used as an alternative continuous phase and demonstrated operational stability comparable to that of the continuous phase during emulsion generation (**Figure 2.9**). Emulsions with φ values between 0.2 and 0.8 were reproducibly produced, with droplet size distributions following trends analogous to those observed for DexMA-based systems. This confirms that the ff-MPH can accommodate different hydrogel chemistries while maintaining control over φ and $D_{droplet}$. To explore multi-material patterning capabilities, exploited for the replication of physiological structures in engineered tissues[117] DexMA loaded with nanohydroxyapatite (DexMA-nHA), and GelMA were employed as continuous phases (**Figure 2.10a**). By synchronizing the supply of multiple continuous phases with the dispersed-phase flow and the 3D motion of the printhead, homogeneous matrices with discontinuous pFGM architectures were fabricated.

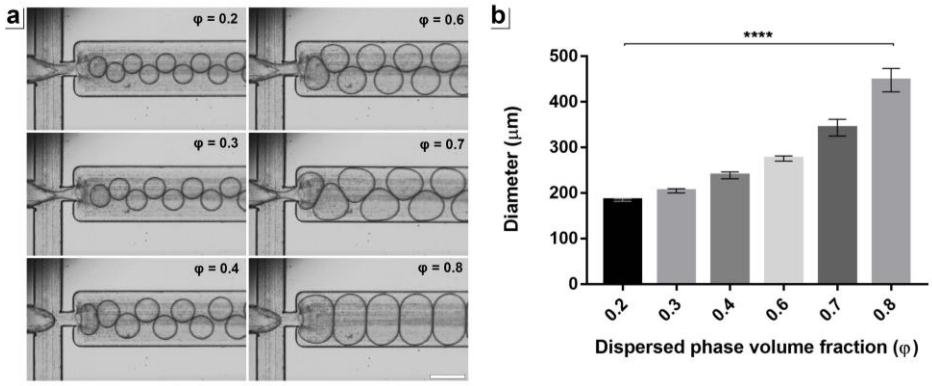

Figure 2.9 Operational range exploration for GelMA emulsion ink production. **a)** Microfluidic production of the cyclohexane-in-GelMA emulsions at different volume fractions of the dispersed phase ($0.2 < \varphi < 0,8$). **b)** Droplet size distributions measured for the selected values of φ. Scale bars: (a) 200 μm. Statistical significances were assessed by one-way ANOVA. Mean ± S.D. n=50, ****p<0.0001.

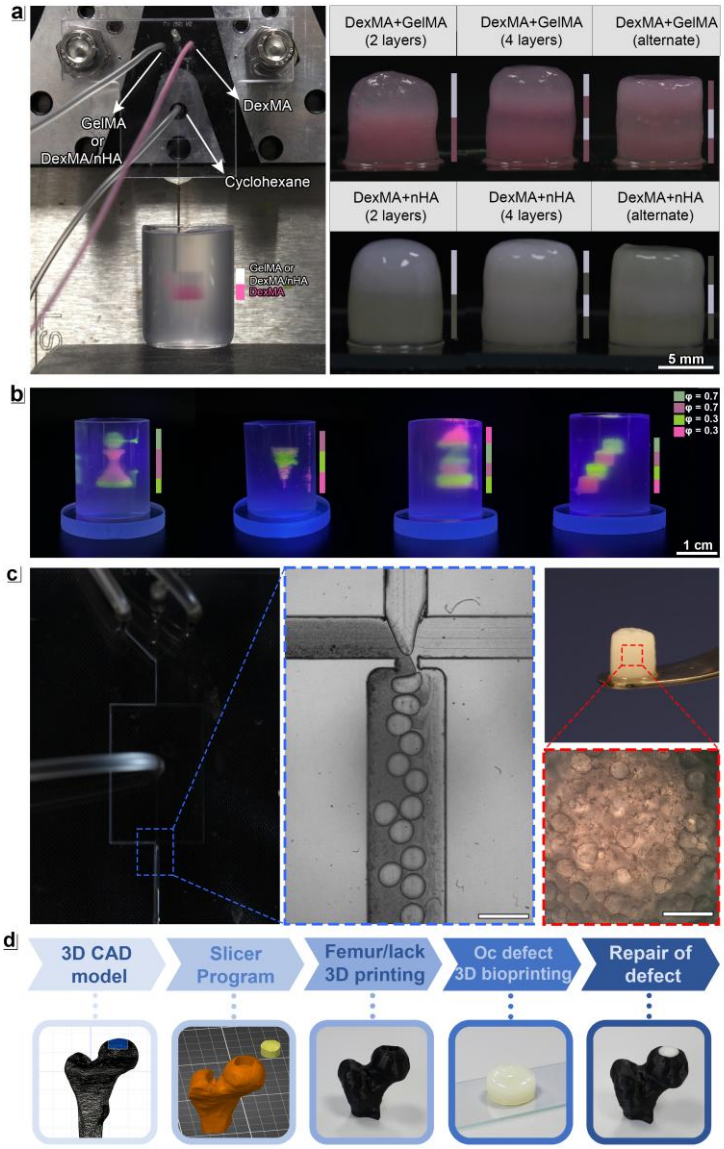

Figure 2.10 Printing a gradient mix of multiple materials. **a)** (left) Multi-inlet chip during alternating printing of GelMA or DexMA/nHA and DexMA emulsions. (right) Alternating scaffolds following cross-linking and extraction from the support bath: DexMA/GelMA FGMs (top-right) and DexMA/nHA FGMs (bottom-right). To differentiate DexMA from GelMA, rhodamine-labelled DexMA was used. **b)** Density gradient complex structures printed using labelled DexMA with fluorescein (in yellow) and labelled DexMA with rhodamine (in red): pawn chess (alternate), inverted pyramid (alternate), horse chess (4 layers), stairs (4 layers). Dark green/pink signals correspond to more dense areas (low porosity), while light green/pink and pale signals correspond to less dense zones (high porosity). **c)** Generating the DexMA/nHA multiple materials structures by producing a Janus-like fiber within the microfluidic channels. Scale bars: 300 µm. **d)** Replicating an osteochondral scaffold to mimic the repair of a cartilage-bone interface defect.

As presented in **Figures 2.9** and **2.10**, multi-material inlets to the ff-MPH enable the production of complex matrices with discrete pFGM features. By precisely synchronizing the supply of the two continuous solutions and the dispersed phase with the 3D motion, one can design a priori and build pFGMs with local porosity and chemical composition precisely tuned. Recent studies have fabricated multi-layered scaffolds via rapid prototyping techniques for tissue engineering applications[17,72,118,119]. For instance, Liu *et al.*[17] manufactured functionally graded tri-layered GelMA/nHA hydrogels to mimic the different osteochondral zones by using an extrusion-based multi-nozzle 3D printing strategy. Similarly, using our multi-inlet ff-MPH, we successfully printed alternating DexMA/GelMA and DexMA/DexMA-nHA scaffolds within the agarose support bath **(Figure 2.10a**). Fluorescent labeling of DexMA with rhodamine enabled clear differentiation between material regions. We then printed complex gradient geometries with alternating material composition, including pawn chess pieces, inverted pyramids, horse chess models, and stair-like structures while preserving predefined density patterns (**Figure 2.10b**). Darker fluorescence indicated denser regions (lower φ), whereas lighter regions corresponded to higher φ. Notably, Janus-like fibers were generated by mixing DexMA and DexMA-nHA directly within the outlet channel of the ff-MPH (**Figure 2.10c**). This configuration enabled side-by-side deposition of materials within a single filament, demonstrating further spatial control at the microscale. The incorporation of nanohydroxyapatite (nHA) into DexMA matrices introduces a mineralized component that may enhance osteoconductive properties in future tissue-engineering applications. As a representative application, a discontinuous FGM architecture mimicking an osteochondral interface was fabricated (**Figure 2.10d**), illustrating the potential of the ff-MPH system for interface engineering[120]. Overall, the multi-material capabilities of the ff-MPH

significantly broaden the design space for fabricating spherical-based porous pFGMs with programmable composition and density.

2.4.Conclusions

The fabrication of complex hierarchical FGM constructs remains challenging, particularly when soft hydrogel systems are involved, and strict rheological requirements are imposed by extrusion-based printing. In conventional approaches, material inks must exhibit specific viscoelastic properties to ensure filament stability, often leading to structural collapse or limited geometric complexity during deposition. These constraints become even more critical when biphasic systems such as emulsions are employed. In this study, we demonstrated a microfluidic-assisted 3D printing strategy for fabricating spherical-based porous, functionally graded hydrogels from low-viscosity biopolymeric solutions, including DexMA, GelMA, and DexMA/nHA formulations. By integrating a ff-MPH with an agarose fluid-gel support bath, we established a manufacturing approach in which emulsion generation and spatial deposition are tightly controlled yet mechanically decoupled from ink rheology. The use of the agarose fluid-gel as a temporary support medium proved essential. Its self-healing and shear-thinning characteristics enabled the confinement of extruded emulsion filaments while maintaining structural integrity prior to crosslinking. This configuration effectively broadened the operational window of the system, enabling fine regulation of dispersed-phase volume fraction (φ), droplet size ($D_{droplet}$), and resulting scaffold density without the need to tailor ink viscosity for printability. Both discontinuous and continuous FGM architectures were successfully fabricated, demonstrating high shape fidelity and mechanical stability after purification. The reproducibility and stability of emulsion generation within the ff-MPH

enabled accurate control of pore-size distribution and three-dimensional density gradients, closely matching the digital blueprints. Furthermore, the combination of microfluidic emulsion templating and suspension-based deposition allowed the fabrication of geometrically complex hydrogel structures, including architectures with pronounced overhangs that would be unattainable through direct air extrusion. Finally, we demonstrated that the ff-MPH system supports multi-material deposition, enabling the patterning of scaffolds with spatially tunable composition and porosity. The incorporation of nHA into DexMA matrices further underscores the potential of this platform to generate hierarchical constructs with distinct physicochemical properties. Overall, this work highlights the synergistic integration of microfluidic-assisted emulsion generation and support-bath 3D printing as a versatile strategy for manufacturing porous FGMs with controlled geometry, density gradients, and material composition. The approach provides a flexible foundation for the design of advanced graded hydrogel systems.

Chapter 3 - Microfluidic-Assisted Digital Manufacturing of Functionally Graded Porous Ceramics

3.1. Introduction

The regeneration of large bone defects remains a major challenge in regenerative medicine, given the intrinsic hierarchical and heterogeneous nature of bone tissue[121,122]. Bone exhibits a peculiar architecture spanning multiple length scales[123], where variations in mineral content, porosity, and microstructure are integrated to ensure mechanical competence and mass transport[124]. Replicating such spatial complexity in engineered scaffolds requires manufacturing strategies capable of precisely controlling both microstructural porosity and macroscopic geometry.

Porous ceramics, and in particular hydroxyapatite-based materials, have been extensively investigated for bone regeneration owing to their chemical similarity to the mineral phase of native bone and their inherent osteoconductive properties[125]. However, conventional fabrication routes for porous ceramics, including replica templating[126], sacrificial porogen leaching[127], and foaming techniques[18], offer limited control over pore interconnectivity, spatial distribution, and gradient continuity. As a result, achieving hierarchical and spatially graded architectures remains challenging. pFGMs represent a rational approach to introduce controlled spatial variations in composition and porosity[128]. In the context of bone substitutes, graded architecture holds the potential to integrate dense, load-bearing regions with highly permeable porous domains within the same construct[88]. Nevertheless, fabricating ceramic pFGMs remains technically demanding, particularly when independent control over microscale pore generation and macroscale

architectural design is required. AM has significantly expanded design freedom in ceramic scaffold fabrication, enabling the layer-by-layer construction of complex geometries with high spatial fidelity[129]. However, extrusion-based ceramic printing, particularly direct ink writing (DIW)[130] and robocasting[131], typically relies on highly loaded, high-viscosity pastes to ensure shape retention after deposition, which inherently limits the ability to engineer microscale porosity within the filaments and constrains material design flexibility[132,133]. Moreover, these approaches often require dedicated printing systems and carefully optimized rheological windows, restricting their broader accessibility and adaptability. Extrusion-based approaches allow precise regulation of filament spacing and global scaffold geometry, yet offer limited control over the internal pore architecture within individual filaments. Conversely, microfluidic technologies enable the controlled generation of monodisperse emulsions that can serve as highly tunable templates for microporous materials[18,48] by regulating droplet size and volume fraction. However, microfluidic systems alone cannot define 3D constructs with arbitrary geometry. Despite these advances, strategies capable of simultaneously controlling microscale pore formation and macroscale scaffold architecture during fabrication remain limited.

To overcome the complementary limitations of these approaches, we have integrated microfluidic emulsion templating with digital manufacturing via a flow-focusing microfluidic printhead (ff-MPH) platform, thereby coupling microscale control of porosity with macroscale architectural design[134]. While extrusion-based AM enables precise spatial definition of scaffold geometry, microfluidics provides programmable control over droplet size and dispersed phase volume fraction, thereby defining pore size and local density at the microscale. This approach decouples ink processability from the final pore

architecture, enabling the use of low-viscosity, nanoparticle-loaded formulations that would otherwise be incompatible with conventional extrusion-based ceramic printing. Importantly, this strategy enables the fabrication of hierarchically porous ceramic scaffolds using standard extrusion-based printing platforms, thereby reducing reliance on specialized ceramic printing systems[133]. In this approach, hydroxyapatite nanoparticles (nHA)-loaded O/W emulsions were generated within the flow-focusing device and immediately deposited, enabling in-line control of droplet templating during printing. By dynamically modulating droplet size and dispersed phase volume fraction, local porosity and density were spatially programmed within 3D constructs. Following crosslinking, freeze-drying, thermal debinding, and sintering, the hybrid printed structures were converted into fully ceramic scaffolds while preserving the programmed hierarchical organization. Importantly, this strategy enabled the processing of low-viscosity, nHA-loaded inks that would otherwise be incompatible with conventional extrusion-based systems[135], further broadening the range of printable ceramic formulations.

The present study focuses on the development of an integrated manufacturing workflow, the preservation of structural integrity after sintering, the evaluation of architectural fidelity across scales, and a preliminary assessment of the osteogenic response to graded porosity, thereby establishing a technological foundation for the future development of advanced bone-regenerative scaffolds.

3.2. Materials and Methods

3.2.1. Materials

Gelatin type B (isolated from bovine hides by an alkaline process) was purchased from Russelott. MA, 2-aminoethyl methacrylate hydrochloride (AEMA·HCl), DMSO, N-(3-Dimethylaminopropyl)-N′-ethylcarbodiimide hydrochloride (EDC), N-Hydroxysuccinimide (NHS), 4-tert-butylcatechol (polymerization inhibitor), SnCl2, nHA, Lithium phenyl-2,4,6-trimethylbenzoylphosphinate (LAP photoinitiator), L-ascorbic acid, β-glycerophosphate, Dexamethasone, paraformaldehyde (PFA), Triton X-100, bovine serum albumin (BSA), and Anti-osteocalcin antibody were purchased from Sigma Aldrich. Agarose was purchased from Carbosynth. Phosphate buffer solution (PBS), α-Minimum Essential Medium (α-MEM), Fetal Bovine Serum (FBS), Penicillin/Streptomycin (P/S), Phalloidin Alexa Fluor 488, 4′,6-Diamidino-2-phenylindole dihydrochloride (DAPI), Alexa Fluor secondary antibodies were purchased from Thermo Fisher Scientific. Anti-osteopontin antibody was purchased from Santa Cruz Biotechnology

3.2.2. Synthesis of Doubly Methacrylated Gelatin

Methacrylation of Primary Amines in Gelatin B

GelMA was synthesized following an established protocol published previously[136]. Briefly, gelatin B (100 g, corresponding to 38.5 mmol of primary amine groups) was dissolved in phosphate buffer (1 L, pH 7.8) at 40 °C under mechanical stirring until complete dissolution. MA, 2.5 equivalents relative to amine groups; 14.34 mL, 96.25 mmol) was then added dropwise, and the reaction was allowed to proceed for 1 h at 40 °C. The reaction mixture was subsequently diluted with double-distilled water (DDW) and dialyzed (MWCO 12,000–14,000 g/mol) against DDW at 40 °C for 24 h, with repeated

water exchanges, to remove unreacted reagents and by-products. The purified solution was frozen and lyophilized to obtain GelMA.

Methacrylation of Carboxylic Acid Groups in Gel-MOD

Further functionalization of GelMA was performed through carbodiimide-mediated methacrylation of carboxylic acid groups. GelMA (10 g, corresponding to 10.98 mmol of carboxylic acid groups) was dissolved in anhydrous DMSO (300 mL) at 50 °C under an inert atmosphere until complete dissolution. EDC (1.2 equivalents; 2.525 g, 13.176 mmol) and NHS (1.5 equivalents; 1.895 g, 16.48 mmol) were added to activate the carboxyl groups. After 30 min, 2-aminoethyl methacrylate hydrochloride (AEMA·HCl, 1.5 equivalents; 4.546 g, 21.96 mmol) was introduced together with 4-tert-butylcatechol (0.01 equivalents; 18 mg) as radical polymerization inhibitor. The reaction mixture was stirred overnight at 50 °C under a light-protected atmosphere. The product was precipitated in cold acetone, collected by filtration, redissolved in DDW, and dialyzed (MWCO 12,000–14,000 g/mol) against distilled water for 24 h. The purified product was finally frozen and lyophilized to obtain doubly methacrylated gelatin (GelMOD).

3.2.3. Preparation of 3D printing Supporting bath

The supporting bath was prepared following a standard operating protocol[102]. Briefly, agarose (0.5 g) was dispersed in 100 mL of DW, and the resulting suspension was sterilized by autoclaving at 121 °C for 20 min. After autoclaving, the agarose solution was allowed to cool to RT under continuous mechanical stirring at 700 rpm for 12 h, promoting the formation of fluid gel. The resulting agarose-based supporting bath was stored at RT and used without further modification.

3.2.4. Fabrication of Polycarbonate Microfluidic Chip

The flow-focusing microfluidic chip was fabricated using polycarbonate sheets and designed with the following characteristics: dispersed and continuous phase inlet = 250 μm; orifice width = 200 μm; output channel width = 1000 μm; channels depth = 200 μm; printing nozzle coupled to the outlet channel = 21G. The microfluidic devices were fabricated following a previously reported procedure[137]. Briefly, 5-mm-thick polycarbonate sheets were engraved using a CNC milling machine (MSG402, ErgWind, Poland). The patterned sheets were subsequently sonicated in isopropanol for 30 min to remove debris and contaminants, and then thermally bonded using a hot press at 130 °C for 30 min. To modify the surface properties of the microchannels, a 20% (w/v) $SnCl_2$ solution in ethanol was injected into the channels. The solution was continuously flushed through the microchannels for 2 h at a flow rate of 20 mL/h and a temperature of 60 °C, to prevent interactions between the polycarbonate substrate and the organic inner phase. Finally, the microchannels were thoroughly rinsed with DW to remove residual $SnCl_2$ prior to use.

3.2.5. Microfluidic Emulsion

O/W emulsions were generated using a flow-focusing microfluidic chip, in which an organic phase (hexadecane) was dispersed within an aqueous continuous phase (15% w/v GelMOD + 20% w/v nHA + 1% w/v Plantacare + 1% w/v LAP). To minimize particle agglomeration in the continuous phase, we first dispersed nHA in water containing Plantacare. Then GelMOD was added slowly to the dispersion to avoid a sudden increase in viscosity and promote uniform dispersion. The final suspension was sonicated prior to

printing to disrupt potential aggregates and reduce the risk of microchannel clogging during microfluidic processing. LAP was used as a radical photoinitiator to enable UV-induced cross-linking of the methacrylated polymer chains. The flow-focusing junction enabled precise control over droplet formation by independently adjusting the flow rates of the continuous and dispersed phases using microfluidic syringe pumps (neMESYS, Cetoni GmbH). Prior to each experiment, both organic and aqueous phases were filtered through syringe filters (0.2–1.2 μm pore size, respectively, Sartorius) and loaded into 1 mL syringes (BD Medical) to prevent clogging of the microchannels. All experiments were conducted under low-light conditions to avoid premature photoinitiator activation. The total flow rate of the two phases was fixed at 60 μL/min, while the dispersed-phase volume fraction (φD) was varied from 0.3 to 0.7 to tailor droplet size and porosity in the resulting materials.

3.2.6. Image analysis (FastCAM) and emulsion characterization

Emulsion formation was monitored using a high-speed camera (Photron FASTCAM Mini UX) operating at 500 frames per second, coupled to an inverted optical microscope (Zeiss Observer.Z1) at a magnification of 5×. The acquired videos were subsequently processed for image analysis. Droplets generated at different dispersed-phase volume fractions (φD) were analyzed using the *Particle Analyze* function in ImageJ to extract characteristic geometric parameters, including droplet area and equivalent diameter. For each volume fraction and time point, at least 50 droplets were analyzed from independent video sequences to ensure statistical robustness. The coefficient of variation (CV) of the droplet diameter was calculated as the ratio between

the standard deviation and the mean diameter (CV = SD/mean × 100), providing a quantitative measure of droplet monodispersity.

3.2.7. Emulsion 3D printing of cubic porous scaffolds and complex geometries

A custom-made 3D bioprinting system was used to fabricate porous ceramic scaffolds. The printer was equipped with two microfluidic syringe pumps (neMESYS, Cetoni GmbH), which were programmed and controlled via neMESYS software. The pumps regulated the delivery of the emulsion inks to the flow-focusing microfluidic printhead (ff-MPH), while a linear motion system in Cartesian configuration, driven by a stepper motor, enabled precise 3D deposition of emulsion fibers. To standardize the printing procedure and enable comparative analysis of emulsion printing, 3D cubes were printed within an agarose-based fluid-gel supporting bath. Using this approach, cubic scaffolds were fabricated with two architectures: uniform porosity (single porosity) and a two-layer axial porosity gradient (double porosity). This approach enabled the fabrication of geometries that could not be printed in air, particularly structures with overhang angles exceeding 45°. Porous fibers were deposited at a constant printing speed of 6.7 $mm \cdot s^{-1}$ (F400). The printed geometries were designed using CAD software (Autodesk Inventor), while more complex models were obtained from the Thingiverse repository. All designs were converted to STL format and subsequently sliced into G-code using Slic3r, with a slice thickness of 0.5 mm. To automate the generation of spatially varying porosities within a single construct, a custom Script function was developed within the neMESYS software environment. This script enabled precise, real-time control of the microfluidic pump flow rates, thereby

regulating the dispersed-phase volume fraction and enabling the fabrication of scaffolds with predefined porosity gradients.

3.2.8. Scaffold cross-linking and sintering

After printing the emulsion within the agarose supporting bath, the external phase of the sample was cross-linked under a UV-lamp (λ = 365 nm) for 30 min. The constructs were retrieved from the agarose fluid-gel using a spatula and immersed in distilled water to remove the remaining agarose bath. The samples were then frozen at -80 °C and freeze-dried. The sintering of nHA was carried out according to a previously published protocol[18]. Briefly, dried scaffolds were subjected to a controlled thermal treatment in a muffle furnace (Nabertherm B180) according to the following temperature program: (i) heating from RT to 400 °C at a rate of 400 °C/h, followed by (ii) a dwell time of 1 h at 400 °C; (iii) heating from 400 °C to 1200 °C over 5 h; (iv) a dwell time of 3 h at 1200 °C; and finally (v) controlled cooling from 1200 °C to RT over 8 h.

3.2.9. Microcomputed Tomography

The internal microstructure of the 3D-printed scaffolds was evaluated by microCT both after printing (wet state) and after thermal debinding and sintering (dry ceramic state) to assess structural preservation and volumetric shrinkage during processing. Image acquisition was performed using Skyscan 1172 (Bruker, USA) with a scanning voltage of 40 kV, power of 10 W, and a rotation step of 0.50° over an angle range of 192.50°. Image smoothing and noise reduction were performed via NRecon software (Bruker, USA). Data analysis and 3D reconstruction of the models were performed with ImageJ software (National Institutes of Health, USA).

3.2.10. Scanning Electron Microscopy

Microstructures and surface morphology of the scaffolds were investigated using SEM (Nova Nano SEM system - FEI Company, USA) operating at 1.50 kV. For morphological characterization of the materials, scaffolds were analyzed both after freeze-drying (green bodies) and after sintering. For cell-material interaction studies, scaffolds colonized with human mesenchymal stem cells (hMSCs) and were collected at different culture time points (days 7, 14, and 21) and fixed in 4% PFA. The samples were then dehydrated through a graded ethanol series, treated with hexamethyldisilazane (HMDS) to preserve cellular morphology, and subsequently air-dried. Prior to imaging, samples were mounted on aluminum stubs using conductive carbon tape and sputter-coated with a thin gold layer (~5 nm) to prevent charging

3.2.11. Rheological Measurement

Rheological properties of the continuous phase solutions (GelMOD + nHA + Plantacare and agarose fluid gel) were analyzed using a rotational rheometer (Anton Paar MCR 305) at 25 °C equipped with a cone-plate geometry. Photorheological measurements were performed to evaluate the UV-induced crosslinking kinetics of the GelMOD–nHA formulation. The samples were exposed to UV light (λ = 365 nm) using an integrated UV source operating at 40% of the maximum intensity. During the test, oscillatory measurements were conducted to monitor the evolution of the storage modulus (G′) and the loss modulus (G″). UV irradiation was initiated 50 s into the measurement to capture the transition from the uncrosslinked state to the crosslinked hydrogel network.

3.2.12. Mechanical testing of 3D printed ceramic scaffolds

Uniaxial quasi-static compression tests were performed using a universal testing machine (Instron, USA), with a 15 N force transducer, at a loading rate of 30%/min. All experiments were performed with three independent samples (N = 3). Young's modulus was obtained as the slope of the stress-strain curve in the linear elastic region, defined as the segment preceding the structure's buckling.

3.2.13. Thermogravimetric analysis

Thermogravimetric analysis (TGA) was performed on GelMOD and GelMOD+nHA samples using a Q5000 IR thermogravimetric analyzer (TA Instruments). Samples (≈5–10 mg) were heated from RT to 600 °C at a heating rate of 10 °C/min under a nitrogen atmosphere (25 mL/min). The resulting thermograms were analyzed using Universal Analysis software (TA Instruments).

3.2.14. Evaluation of the osteogenic properties of the nHA scaffolds

Human mesenchymal stem cells (hMSCs) were cultured in basal α-MEM medium supplemented with 10% FBS and 1% P/S. Cells were maintained under standard culture conditions (37 °C, 5% CO_2), and the culture medium was refreshed every two days. Prior to seeding, cells were detached using trypsin–EDTA (0.25%), centrifuged at 300 × g for 5 min at RT, and resuspended in growth medium at a concentration of 1×10^6 cells mL^{-1}.

Ceramic scaffolds were washed with ethanol to remove potential processing residues and sterilized for 2h under UV irradiation. Each scaffold was placed in a 1.5 mL microcentrifuge tube and seeded with 200 µL of cell suspension, corresponding to a final seeding density of 2×10^5 cells per scaffold ($3 \times 3 \times 2$ mm^3). Samples were incubated for 2 h under static conditions to enable efficient initial cell adhesion to the scaffold surface. During incubation, tubes were gently agitated every 15 min to resuspend cells that had not yet adhered and enhance homogeneous cell distribution.

After seeding, the scaffolds were transferred to a new 24-well plate and cultured under standard conditions (37 °C, 5% CO_2). The culture medium was replaced every two days. After 7 days of culture in basal medium, selected scaffolds were switched to osteogenic differentiation medium composed of α-MEM supplemented with 10% FBS, 1% P/S, 50 µg mL^{-1} L-ascorbic acid, 10 mM β-glycerophosphate, and 100 nM dexamethasone.

3.2.15. Immunofluorescence (IF) staining

hMSCs-seeded ceramic scaffolds were fixed using 4% (v/v) PFA in PBS overnight at 4°C. Cells were permeabilized with 0.3% (v/v) Triton X-100 in PBS for 30 min at RT, followed by blocking of non-specific binding with 5% (w/v) BSA (Bovine Serum Albumin) in PBS for 2 h at RT. For the detection of osteocalcin (OCN) and osteopontin (OPN), both late osteogenic differentiation markers, samples were incubated overnight at 4 °C with mouse anti-osteocalcin (Sigma-Aldrich) and rabbit anti-osteopontin (Santa Cruz Biotechnology) primary antibodies, both diluted 1:100 in 0.5% BSA. After two PBS washes (5 min each), samples were incubated with Alexa Fluor 568-conjugated anti-mouse and Alexa Fluor 647-conjugated anti-rabbit secondary

antibodies (both diluted 1:500 in 0.5% BSA) for 2 h at RT. F-actin was stained using Phalloidin Alexa Fluor 488 conjugate (Invitrogen), added during the secondary antibody incubation step. Cell nuclei were finally counterstained with DAPI (Invitrogen) diluted 1:1000 in 1% BSA solution for 10 min at RT. Fluorescence images were acquired using a Nikon A1R confocal microscope, while image analysis was performed using ImageJ software (National Institutes of Health, USA).

3.2.16. Alamar Blue

Cell metabolic activity was evaluated using the Alamar Blue assay (Bio-Rad). At the selected culture time points (days 7, 14, 21, and 28), the culture medium was replaced with fresh medium containing 10% (v/v) Alamar Blue reagent, and samples were incubated for 4 h under standard culture conditions. After incubation, 100 µL of the supernatant was transferred to a 96-well plate, and absorbance was measured at 570 nm and 600 nm using a microplate reader. Cellular metabolic activity was calculated according to the manufacturer's instructions. All experiments were performed in triplicate.

3.2.17. Quantitative real-time polymerase chain reaction

At the designated experimental time-points, the cell-seeded scaffolds were transferred into sterile 2 mL RNase-free tubes, washed in PBS for 5 min, and rapidly frozen in liquid nitrogen, and stored until RNA extraction. Total RNA was extracted from samples of each experimental condition using a mortar and pestle and liquid nitrogen. The pulverized material was collected with 700 µL of TRIzol reagent (Invitrogen, Life Technologies) and transferred into a new RNase-free tube. It was then purified using the RNeasy Mini Kit (Qiagen, 74106) according to the manufacturer's protocol. RNA concentration and

purity were assessed using NanoDrop UV-Vis spectrophotometer (Thermo Fisher Scientific). For reverse transcription, 500 ng of total RNA were converted into complementary DNA (cDNA) using the High-Capacity cDNA Reverse Transcription Kit (Applied Biosystems - 374966) in a total reaction volume of 20 µL. The resulting cDNA was then diluted to a final volume of 50 µL. Quantitative real-time polymerase chain reaction (qRT-PCR) was performed using the RT-PCR Mix SYBR (A&A Biotechnology -2008-1000) on a LightCycler 96 system (Roche). All reactions were carried out in duplicate in a total volume of 25 µL. Gene expression was evaluated using the ΔΔCt method. Fold change values were subsequently expressed relative to the control group by subtracting 1 from 2^-ΔΔCt, so that positive and negative values indicate upregulation or downregulation relative to baseline, respectively. GUS was used as a housekeeping gene. Primer sequences used for osteogenic gene expression analysis are provided in **Table 3.1**.

GENE	*FORWARD*	*REVERSE*
hGUSb	GGAATTTTGCCGATTTCATGA	CCGAGTGAAGATCCCCTTTTT
hALPL	ACGTACAACACCAATGCCC	GGTCACAATGCCCACAGATT
hBGLAP	GCGCTACCTGTATCAATGGC	GGCAAGGGGAAGAGGAAAGA
hSPP1	ACTGATTTTCCCACGGACCT	CTCCTCGCTTTCCATGTGTG
hRUNX2	GGGACCTACAGACAGCCTTT	AAATCTGCCATGTGACTGCC
hKI67	AGCAAGCCTGAGAAATTGGG	AGTTCAGGTCTTAGGTGCCC

Table 3.1 Primer sequences used for quantitative PCR analysis. Forward and reverse primer sequences for the target genes (hGUSB, hALPL, hBGLAP, hSPP1, hRUNX2, hKI67).

3.2.18. Statistical Analysis

Statistical analysis was performed using GraphPad Prism (GraphPad Software Inc., La Jolla, CA). Data normality was evaluated using the D'Agostino–Pearson test. Depending on the experimental design, a one-way or a two-way ANOVA was used. Statistical significance was defined as $p < 0.05$. Sample size (n) is specified within figure captions.

3.3. Results and Discussion

3.3.1. Microfluidic generation of emulsion templates and control over pore architecture

The combination of microfluidics and digital manufacturing is emerging as a novel platform for fabricating pFGMs[48,134]. In this work, a flow-focusing microfluidic chip (**Figure 3.1a**) was designed and fabricated to enable the controlled generation of o/w emulsions in which the continuous phase is a nHA-loaded GelMOD solution, and the dispersed phase is hexadecane. The chip geometry was adapted from a flow-focusing device previously developed and described in **Chapter 2** of this thesis. For the present study, the channel dimensions were increased (approximately twofold, orifice width = 200 μm; output channel width = 1000 μm; channel depth = 200 μm) to allow the flow of the nHA-loaded polymer solution and to minimize the risk of clogging associated with suspended nanoparticles. The microfluidic chip was conceived as the core element of the manufacturing strategy, enabling in-line control of the emulsion-templating process prior to material deposition. The device geometry ensures hydrodynamic confinement of the dispersed phase, allowing droplet breakup in a stable dripping regime[138] within the explored operational window. High-speed imaging revealed that across the investigated dispersed-phase volume fractions (φ = 0.3–0.7), droplet formation remained periodic and stable, without transitioning to jetting or satellite droplet formation. Operating in this regime ensures the generation of monodisperse droplets[139], which is important for emulsion-templating approaches, where droplet size directly determines the pore size of the final scaffold[41,140]. Maintaining a narrow droplet size distribution, therefore, enables better control over the resulting pore architecture and overall scaffold porosity.

As reported in **Figure 3.1b**, increasing φ resulted in a progressive increase in droplet diameter. In these experiments, φ was adjusted by varying the relative flow rates of the dispersed and continuous phases while maintaining a constant total flow rate of 60 µL/min. The resulting droplet diameter increased consistently with φ, demonstrating that droplet size can be tuned by controlling the flow rate ratio between the two phases. The diameter distributions were unimodal with limited dispersion (**Figure 3.1c,d**), with coefficients of variation (CV) below 10%, indicating a high level of monodispersity, in line with values typically reported for microfluidic droplet generators operating in controlled flow-focusing systems[141]. These results demonstrate that the pore size of the resulting scaffolds can be tuned by controlling the droplet size through adjustment of the relative flow rates of the two phases. To further evaluate process robustness, droplet production at φ = 0.3 and φ = 0.7 was monitored over time (0, 5, and 10 minutes), since stable droplet generation is required to ensure consistent porosity during prolonged printing sequences. No statistically significant variation in average droplet diameter or CV was observed (**Figure 3.1e**), demonstrating stable hydrodynamic conditions and the absence of clogging or nHA particle sedimentation within the microchannels. The droplet generation frequency remained constant within experimental uncertainty, confirming steady dripping conditions throughout the acquisition period.

We characterized droplet generation in the microfluidic chip and verified that the system provides programmable, stable control over droplet formation, making it suitable for reproducible manufacturing of porous scaffolds. These results demonstrate that the system enables robust, reproducible control over droplet formation even under particle-loaded conditions, a known limitation in the microfluidic processing of composite materials[142]. This capability is

critical for translating microfluidic templating strategies into scalable manufacturing workflows for porous ceramics.

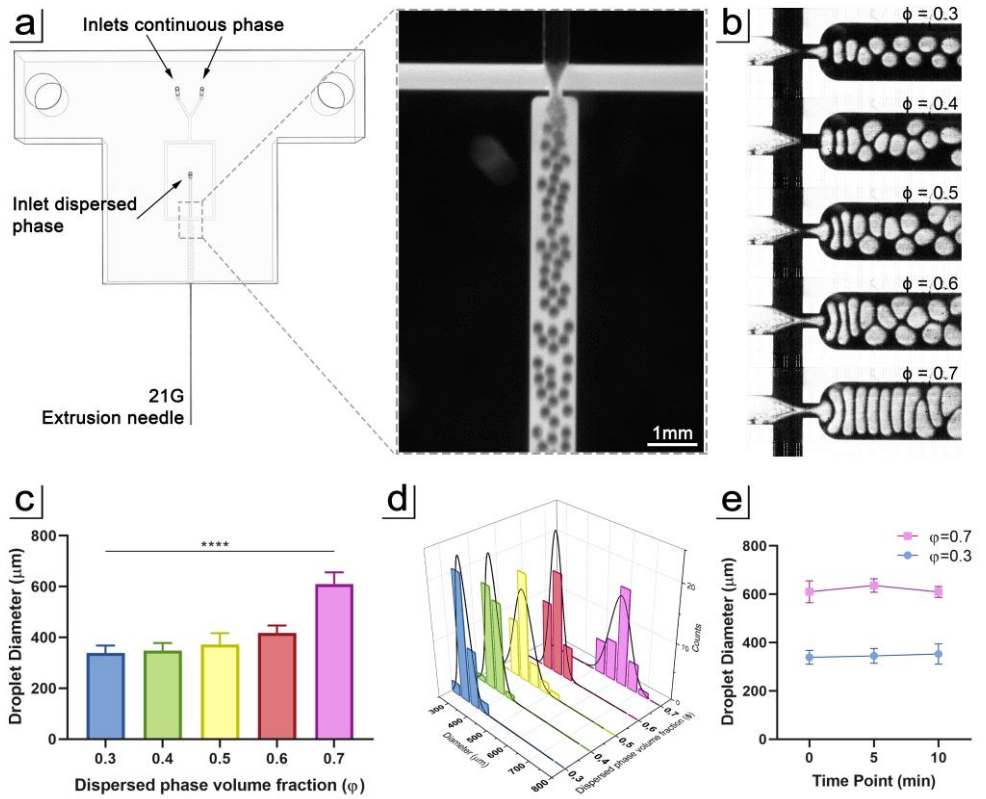

Figure 3.1 Operational range exploration for emulsion ink production. **a)** Schematics of the ff-MPH used to generate functionally graded O/W emulsions (values of characteristic dimensions of the microfluidic device are reported in the experimental section). **b)** Microfluidic production of the emulsions at different volume fractions of the dispersed phase ($0.2 < \varphi < 0,8$). **c,d)** Average droplet diameters (c) and droplet size distributions (d) measured for the selected values of φ. **e)** Droplet diameter measured over time for two representative dispersed phase volume fractions ($\varphi = 0.3$ and $\varphi = 0.7$). Statistical significances were assessed by one-way ANOVA. Mean ± S.D. n=50, ****$p<0.0001$.

3.3.2. Rheological characterization and embedded printing strategy

The microfluidic flow-focusing device was integrated into a custom extrusion-based printing system (**Figure 3.2a**) and operated as a microfluidic printhead

(ff-MPH), enabling synchronized emulsion generation and spatial deposition. This configuration enabled continuous production of nHA-loaded emulsions directly upstream of the nozzle, with immediate deposition within a supporting medium. Using this setup, complex geometries, including overhanging features, were successfully fabricated within the agarose support bath (**Figure 3.2b**), demonstrating stable extrusion and high shape fidelity for structures that would otherwise collapse when printed in air[72].

To rationalize this embedded printing strategy, the rheological properties of both the emulsion ink and the supporting bath were investigated (**Figure 3.2c**). The GelMOD–nHA emulsion exhibited low viscosity and only limited shear-thinning behavior across the tested shear rate range, indicating insufficient yield stress to support free-standing extrusion in air, which resulted in filament spreading and geometric collapse. In contrast, the agarose supporting bath exhibited shear-thinning and yield-stress behavior, allowing localized fluidization during nozzle movement and rapid recovery upon shear removal. This behavior is consistent with previous reports on low-viscosity emulsion-based inks, which typically lack the viscoelastic properties required for direct ink writing in air[130,143]. This behavior stabilizes extruded filaments within the support medium and effectively decouples printability from the emulsion's intrinsic rheological properties. Compared to conventional direct ink writing approaches, which require strict rheological windows[132], the use of a supporting bath significantly expands the range of printable formulations. Following deposition, the printed filaments were stabilized via in situ UV crosslinking enabled by the photoinitiator LAP in the continuous phase. Photorheological analysis revealed a rapid increase in storage modulus upon UV exposure, indicating the formation of a crosslinked polymer network (**Figure 3.2d**). The transition from a weak viscoelastic state ($G' > G''$) to a

predominantly elastic solid ($G' \gg G''$) confirms efficient photopolymerization of the GelMOD matrix, which rapidly fixes the printed emulsion microstructure and preserves the microfluidically defined droplet architecture prior to subsequent processing. Notably, prior to UV exposure, the storage modulus remained slightly higher than the loss modulus ($G' > G''$), indicating a weak viscoelastic structure that contributes to droplet stability and helps limit particle sedimentation before photo-induced crosslinking. Importantly, UV-induced crosslinking was performed directly within the agarose bath, enabling immediate solidification after deposition. Once crosslinked, the printed constructs could be safely collected from the support medium while preserving the programmed geometry (**Figure 3.2b, bottom**). Overall, integrating microfluidics with embedded printing overcomes key limitations of using these techniques independently, enabling simultaneous control over microstructure and macroscopic geometry.

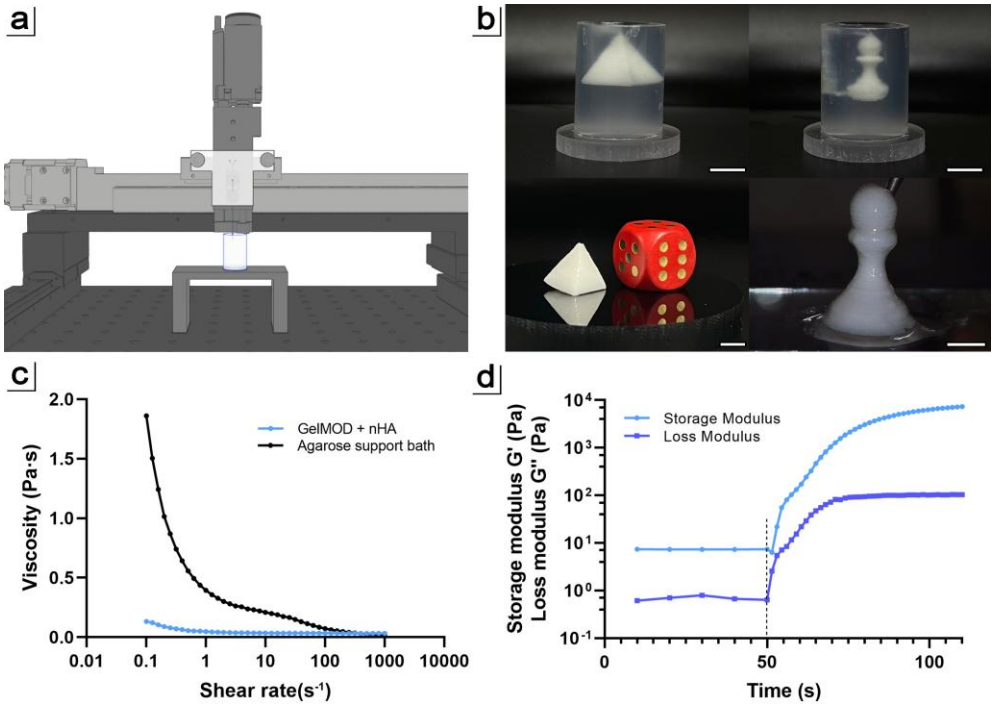

Figure 3.2 Microfluidic-assisted embedded printing and rheology of GelMOD-nHA emulsions. **a)** 3D printing of porous FGMs. a) Schematics of the 3D printing setup used to generate and 3D print emulsion inks. **b)** 3D printed complex architectures in fluid-gel (top), complex architecture after UV crosslinking (bottom). **c)** Rheological characterization of the agarose fluid-gel and GelMOD-nHA continuous phase. **d)** Photorheological characterization of GelMOD+nHA+LAP. Scale bars: b) (top) 1 cm, (bottom) 1 cm, 5mm.

3.3.3. Material conversion, sintering behaviour, and mechanical response

Following UV crosslinking and freeze-drying, the printed structures were subjected to thermal debinding and sintering (1200 °C) to convert the composite polymer-ceramic constructs into fully ceramic scaffolds. Macroscopic inspection already revealed a clear transformation of the printed structures during thermal treatment (**Figure 3.3a**). While the freeze-dried samples retained the geometry of the printed green bodies, sintering produced compact ceramic scaffolds with a visibly reduced overall size, reflecting the removal of the polymeric template and the densification of the inorganic

phase[144]. The microstructural evolution of the scaffolds during thermal processing was further investigated by scanning electron microscopy. SEM images of the freeze-dried printed constructs (green bodies) revealed nHA nanoparticles distributed throughout the scaffold matrix, with individual particles still clearly distinguishable and arranged in loosely packed agglomerates (**Figure 3.3b**). Following thermal debinding and sintering, SEM analysis revealed a significant microstructural transformation: the nanoparticles underwent neck formation[144] and partial coalescence, forming a consolidated ceramic network (**Figure 3.3c**). The observed densification and particle necking are characteristic of hydroxyapatite-based systems subjected to thermal treatment in this temperature range[145]. Importantly, the preservation of the porous architecture indicates that the emulsion-templated structure remains stable during both debinding and sintering, a critical challenge in templated ceramic processing. Individual particle boundaries became progressively less distinct as adjacent particles fused together during high-temperature treatment. Despite this consolidation, the overall porous architecture was preserved, indicating that ceramic densification occurred without collapse of the emulsion-templated structure. The microstructural transformations observed after thermal treatment are consistent with the thermal degradation behavior of the polymeric matrix, as evidenced by the TGA profiles shown in **Figure 3.3d**. Both samples (GelMOD matrix and the GelMOD-nHA composite) exhibit an initial weight loss below 150 °C, which can be attributed to the evaporation of residual moisture and volatile components trapped within the polymeric network. The main degradation step occurs between approximately 250 °C and 360 °C, corresponding to the thermal decomposition of the GelMOD polymer chains. In the composite sample, the degradation profile remains similar, indicating that HA nanoparticles do not significantly alter the polymer matrix's thermal stability.

However, a substantially higher residual mass is retained at elevated temperatures due to the thermally stable hydroxyapatite phase. The stabilization of the mass above ~400 °C confirms the complete removal of the organic phase prior to sintering, indicating that the selected thermal schedule provides a suitable debinding window for converting the polymer–ceramic composite constructs into fully ceramic scaffolds.

Consistent with the removal of the organic phase and the subsequent ceramic densification evidenced by TGA, the structural evolution during thermal processing was further quantified by microCT analysis (**Figure 3.3e**). Comparison between the wet (post-printing) green bodies and the dry ceramic scaffolds (after-sintering) revealed a substantial volumetric shrinkage during thermal treatment. Quantitative analysis indicated a volumetric reduction of approximately 83% (**Figure 3.3f**), this value falls within the range typically reported for polymer-derived ceramic systems, where significant dimensional changes are associated with organic phase removal and particle rearrangement. The isotropic nature of the shrinkage suggests uniform stress distribution during sintering, which is essential to avoid structural defects such as cracking or warping. This shrinkage originates from two sequential processes occurring during thermal treatment: the removal of the polymeric matrix during thermal debinding and the subsequent densification of the ceramic network during sintering. Importantly, the shrinkage remained largely isotropic within the experimental resolution, indicating homogeneous densification without macroscopic distortion or collapse of the printed architecture. These results demonstrate that the proposed workflow enables predictable dimensional evolution from the green body to the fully ceramic scaffold while preserving the programmed porous architecture. Finally, the mechanical response of the resulting ceramic scaffolds was evaluated by

compression testing (**Figure 3.3g**). Dense ceramic samples exhibited a Young's modulus of 5.92 ± 0.96 MPa, whereas porous scaffolds showed a significantly lower modulus of 1.93 ± 1.06 MPa. This approximately threefold reduction in stiffness reflects the engineered porous architecture, which decreases the effective load-bearing cross-section and promotes stress redistribution within the cellular structure. Although the absolute stiffness values remain below those of native cortical and trabecular bone, the relative mechanical differentiation between dense and porous constructs reflects the structural hierarchy observed in osseous tissue[146]. In particular, the increase in modulus from porous to non-porous ceramics parallels the functional distinction between highly porous trabecular regions and denser load-bearing cortical domains. These findings demonstrate that microfluidically controlled porosity can be used to tune the mechanical properties of the resulting ceramic scaffolds, enabling the design of mechanically heterogeneous structures inspired by the graded organization of bone. Although the measured Young's modulus remains lower than that of native bone, this is consistent with highly porous hydroxyapatite scaffolds reported in the literature[147,148]. The reduction in stiffness is an expected consequence of increased porosity, highlighting the need to balance mechanical performance and mass transport in scaffold design. In this context, microfluidic control of porosity provides a powerful strategy to address this trade-off, enabling spatially defined modulation of pore architecture. This represents a key advancement toward the fabrication of functionally graded ceramic scaffolds with predictable mechanical properties.

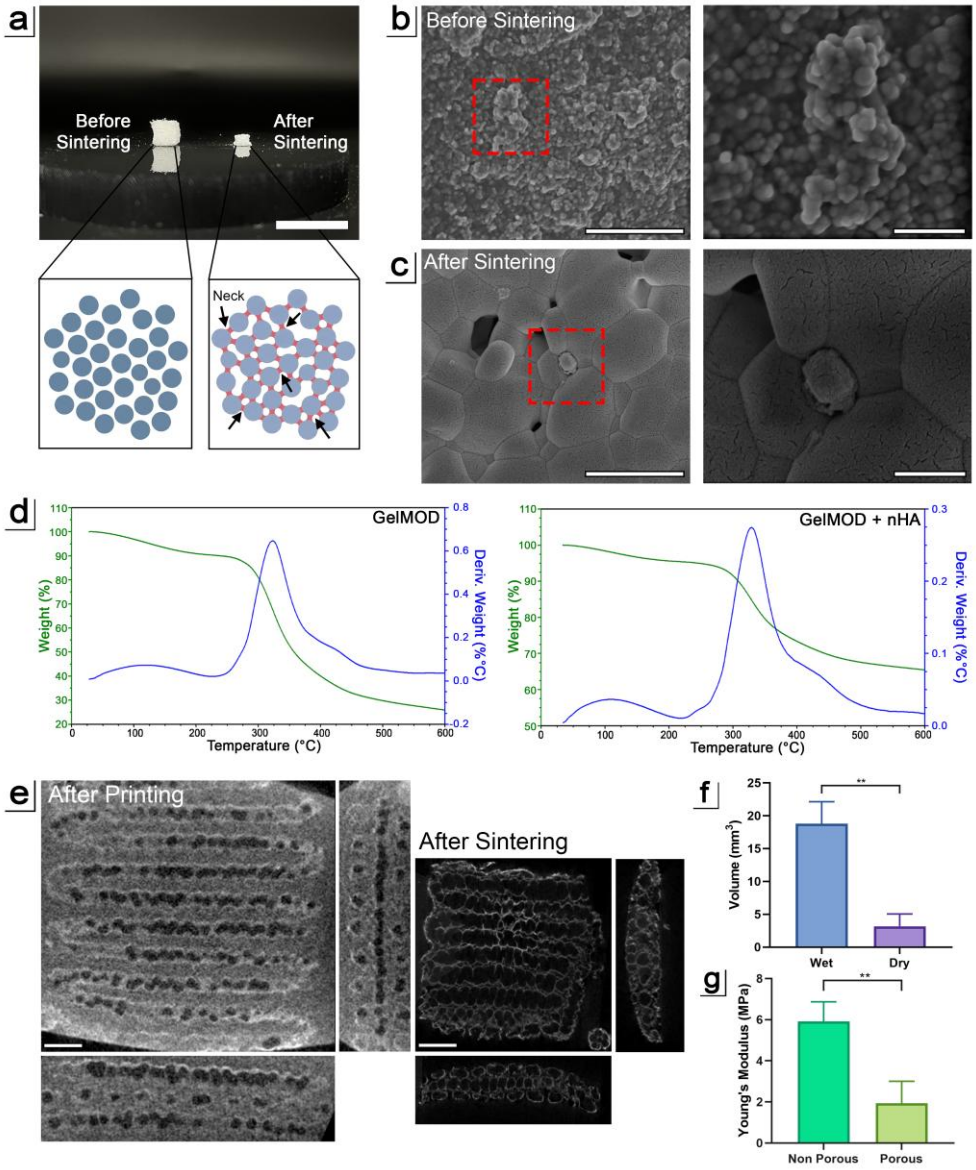

Figure 3.3 Structural evolution and mechanical properties of the microfluidic-templated ceramic scaffolds. **a)** Optical image of printed scaffolds before and after sintering. **b)** SEM images of the freeze-dried scaffold (green body). **c)** SEM images of the scaffold after sintering. **d)** TGA of GelMOD and GelMOD+nHA samples. **e)** microCT reconstructions of the scaffold architecture after printing and after sintering. **f)** Quantitative analysis of volumetric shrinkage obtained from microCT measurements comparing wet (post-printing) and dry (post-sintering) samples. **g)** Young's modulus of dense and porous ceramic scaffolds obtained from compression testing. Scale bar: a) 1cm, b,c) 2µm (top), 500nm (bottom), e) 1mm. Statistical significances were assessed by one-way ANOVA. Mean ± S.D. n=3, **p<0.01.

Having established that the porous architecture is preserved after sintering and that shrinkage remains largely isotropic, the ability of the manufacturing strategy to generate spatially controlled pore architectures was confirmed through microCT analysis (**Figure 3.4**). Three-dimensional reconstructions of the ceramic scaffolds (after-sintering) enabled direct visualization of the internal pore architecture (**Figure 3.4a–b**). Scaffolds fabricated using a constant droplet generation parameter (Single Porosity with $\varphi = 0.7$) exhibited a uniform pore distribution throughout the structure (**Figure 3.4a**), whereas constructs printed by dynamically modulating the droplet generation parameters (Double Porosity with $\varphi = 0.7$ and $\varphi = 0.3$) displayed clearly distinguishable regions with different pore sizes and local porosity (**Figure 3.4b**). Color-coded pore-size maps further highlighted the spatial organization of the pore architecture, confirming that the droplet-size modulation introduced during printing was preserved after sintering (**Figure 3.4c**). This behavior is quantitatively reflected in the porosity profiles extracted along the scaffold height: the single-porosity scaffold shows nearly constant porosity, while the double-porosity scaffold exhibits a clear transition between the two regions (**Figure 3.4d**). Consistently, pore size distributions extracted from the reconstructed volumes reveal distinct pore populations associated with the different printing conditions (**Figure 3.4e**).

Together, these results demonstrate that the droplet size modulation achieved at the microfluidic stage can be reliably translated into spatially controlled porous architectures in the final ceramic scaffolds. Previous extrusion-based approaches have explored the fabrication of porous ceramic scaffolds. For instance, Guo et al.[147] reported hydroxyapatite scaffolds fabricated via direct ink writing, where porosity is governed by a combination of filament spacing and foaming-assisted strategies, primarily at the macroscale. Similarly,

robocasting-based approaches[131] enable precise control over scaffold geometry, yet offer limited tunability of the internal pore structure within individual filaments. In contrast, the presented approach enables continuous, programmable control over pore size and spatial distribution at the microscale via microfluidic droplet templating. Importantly, this level of control over pore architecture directly translates into tunable mechanical properties, as confirmed by compression testing, highlighting the potential of the proposed strategy for the design of mechanically graded, bone-mimetic ceramic scaffolds.

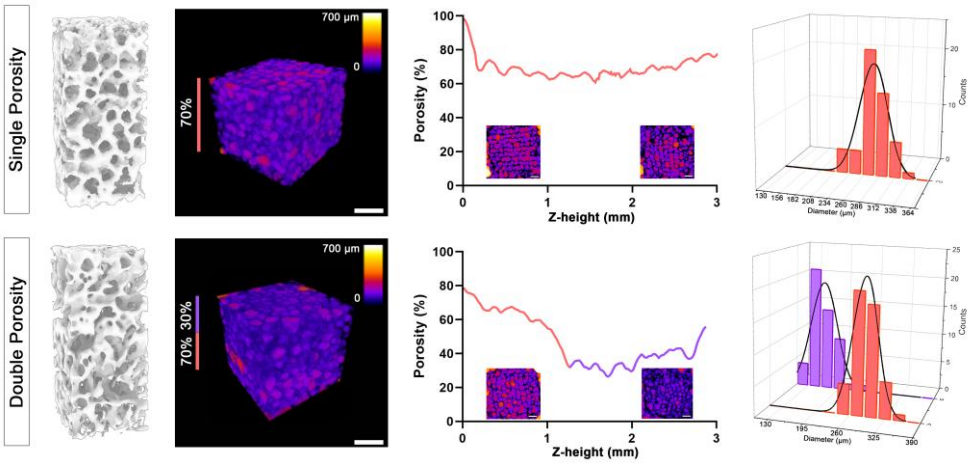

Figure 3.4 pFGMs internal topographic analysis via microCT. Representative results for Single Porosity (top) and Double Porosity (bottom) scaffolds. From left to right: three-dimensional reconstruction of the porous structures obtained from microCT image stacks; color-coded pore size maps highlighting spatial variations in pore diameter; porosity profiles along the scaffold height (Z-axis); and pore size distributions extracted from volumetric analysis. Scale bars: 1 mm (reconstructions) and 650 µm (pore maps).

3.3.4. Bioactivity and Osteoinductive Capacity of Porous Ceramic Scaffolds toward Stem Cells

To evaluate the biological properties of the fabricated scaffolds, bone-marrow derived human mesenchymal stem cells (hMSCs) were seeded onto the porous

ceramic constructs and cultured under either basal or osteogenic conditions. Prior to cell seeding, scaffolds were thoroughly washed to remove potential processing agents, including surfactant and photoinitiator, and subsequently sterilized under UV irradiation to ensure a sterile environment suitable for biological evaluation. After 7 days of culture, the samples were divided into two groups: one cultured in osteogenic medium and the other maintained in basal medium as a control to assess the osteogenic potential of the scaffolds.

Cell distribution, colonization, and interaction with the porous ceramic architecture were further investigated by SEM (**Figure 3.5a-c).** High-resolution SEM imaging at 7, 14, and 21 days of culture revealed a pronounced, time-dependent progression of cell colonization across both the scaffold surface and the internal pore walls. At early time points (day 7), cells exhibited an elongated morphology with prominent filopodial extensions anchoring to the ceramic substrate, indicative of active cell-material engagement. As culture progressed (day 14), cells formed increasingly interconnected networks spanning the porous architecture, and by day 21, a dense, continuous cellular layer bridged adjacent pores. This extensive colonization highlights the scaffold's capacity to support not only robust cell adhesion but also effective cell spreading and spatial organization throughout its three-dimensional structure. Notably, the highly interconnected pore network facilitated cell infiltration and migration across the scaffold volume, promoting a progressively more homogeneous cellular distribution.

Cell viability and metabolic activity were assessed using the Alamar Blue assay at multiple time points during culture (**Figure 3.5d**). Overall, sustained metabolic activity was observed throughout the experimental period, indicating the cytocompatibility of the ceramic scaffolds on hMSCs.

Metabolic activity progressively increased from day 7 to day 21 in both experimental groups, reaching a peak at day 21, followed by a decrease on day 28. Notably, although an earlier peak in proliferation was initially anticipated around day 7, this trend suggests a delayed proliferative response within the 3D scaffold environment. This behavior may be attributed to the intrinsic heterogeneity in cell distribution within the porous structure, resulting from the predominantly passive, static seeding approach. While cells efficiently adhered to the scaffold, the three-dimensional architecture likely led to uneven colonization, with regions of higher and lower cell density. Given that mesenchymal stem cells are known to undergo osteogenic differentiation preferentially at higher confluence, cells located in less densely populated regions may have retained proliferative activity over extended time points[149]. This spatial heterogeneity could explain the similar metabolic trends observed between basal and osteogenic conditions, with no clear divergence between the two groups.

Immunofluorescence analysis demonstrated extensive cell colonization and osteogenic progression within the porous scaffold (**Figure 3.6**). hMSCs showed a well-defined actin cytoskeleton with prominent stress fibers and were broadly distributed across the scaffold surface, with morphological features consistent with firm attachment and cytoskeletal remodeling in response to the ceramic microenvironment. OCN, commonly associated with late-stage osteogenic differentiation, was readily detected, with signal intensity increasing at later culture time points. OPN was also detected in distinct regions throughout the scaffold, consistent with osteogenic protein expression and progression toward matrix formation and maturation. Together, the distribution of OCN and OPN signals suggests that osteogenic differentiation was not confined to isolated regions but extended across the

three-dimensional scaffold.

These findings highlight the ability of porous ceramic architecture to support not only effective cell engraftment but also microenvironment-driven osteogenic maturation. The coexistence of widespread cellular colonization and spatially distributed expression of osteogenic markers underscores the scaffold's intrinsic osteoinductive properties, promoting a coordinated transition from cell adhesion to lineage-specific differentiation within a 3D context.

To further quantify osteogenic commitment, gene expression analysis of key osteogenic markers was performed (**Figure 3.5e**). Gene expression levels were reported as fold changes in samples cultured in growth medium (GM) relative to those cultured in osteogenic medium (OM), which served as the reference condition. Therefore, a fold change value of 1 indicates equivalent gene expression between GM and OM conditions. Overall, the expression levels of all investigated markers were comparable between the two conditions, with most values remaining close to 1 or below. The greatest increase was observed for ALP, reaching approximately 2-fold at day 21, while all other markers showed more moderate changes. These results suggest that hMSCs cultured on ceramic scaffolds under basal conditions exhibit a gene expression profile largely comparable to that observed under osteogenic stimulation, supporting the scaffold's intrinsic bioactivity. ALP expression showed a transient increase, peaking at day 21, suggesting a slight temporal shift in early osteogenic differentiation compared to the OM condition. In contrast, in the GM condition, expression of late osteogenic markers, including OCN (gene BGLAP) and OPN (gene SPP1), decreased progressively from day 14 to day 28. This trend may reflect differences in the kinetics of matrix maturation, potentially associated with the heterogeneous

cell distribution within the 3D porous scaffold and the absence of exogenous osteoinductive factors, leading to a less synchronized differentiation process. RUNX2 expression remained relatively stable across all time points, with values close to 1, indicating no substantial differences between GM and OM conditions in the early transcriptional commitment stage. Similarly, Ki67 expression decreased over time, particularly from day 14 to days 21 and 28, consistent with a reduction in proliferative activity as cells progressively differentiate.

Collectively, these findings indicate that the hydroxyapatite-based scaffold promotes osteogenic commitment of hMSCs even in the absence of osteogenic supplements, resulting in a gene expression profile comparable to that observed under standard osteogenic conditions. This supports the scaffold's osteoinductive potential and highlights its ability to modulate cell fate through material-driven cues.

Overall, these results demonstrate that the microfluidic-assisted printed ceramic scaffolds provide a favorable microenvironment for hMSC attachment, proliferation, and osteogenic commitment. The combination of bioactive hydroxyapatite and controlled porous architecture appears to support both cell viability and osteogenic differentiation, highlighting the potential of this manufacturing strategy for the development of bone-inspired ceramic scaffolds.

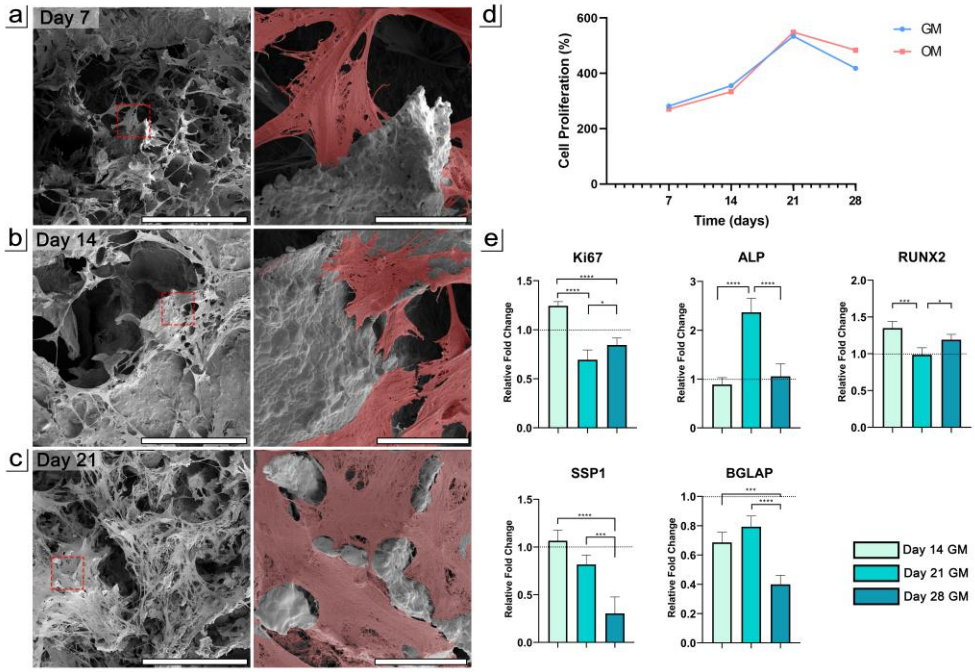

Figure 3.5 Biological evaluation of porous ceramic scaffolds. **a-c)** SEM images of hMSCs (highlighted in red) seeded on porous scaffolds at (b) day 7, (c) day 14, and (d) day 21. **d)** Cell proliferation of hMSCs cultured in GM and OM scaffolds over 28 days, relative to day 0. **e)** Gene expression analysis of osteogenic markers, including Ki67, ALP, RUNX2, SSP1, and BGLAP, at days 14, 21, and 28 (relative fold change). Scale bar: a-c) 200µm (left) 30µm (right). Statistical significances were assessed by one-way ANOVA. *$p < 0.05$, **$p < 0.01$, ***$p < 0.001$, ****$p < 0.0001$.

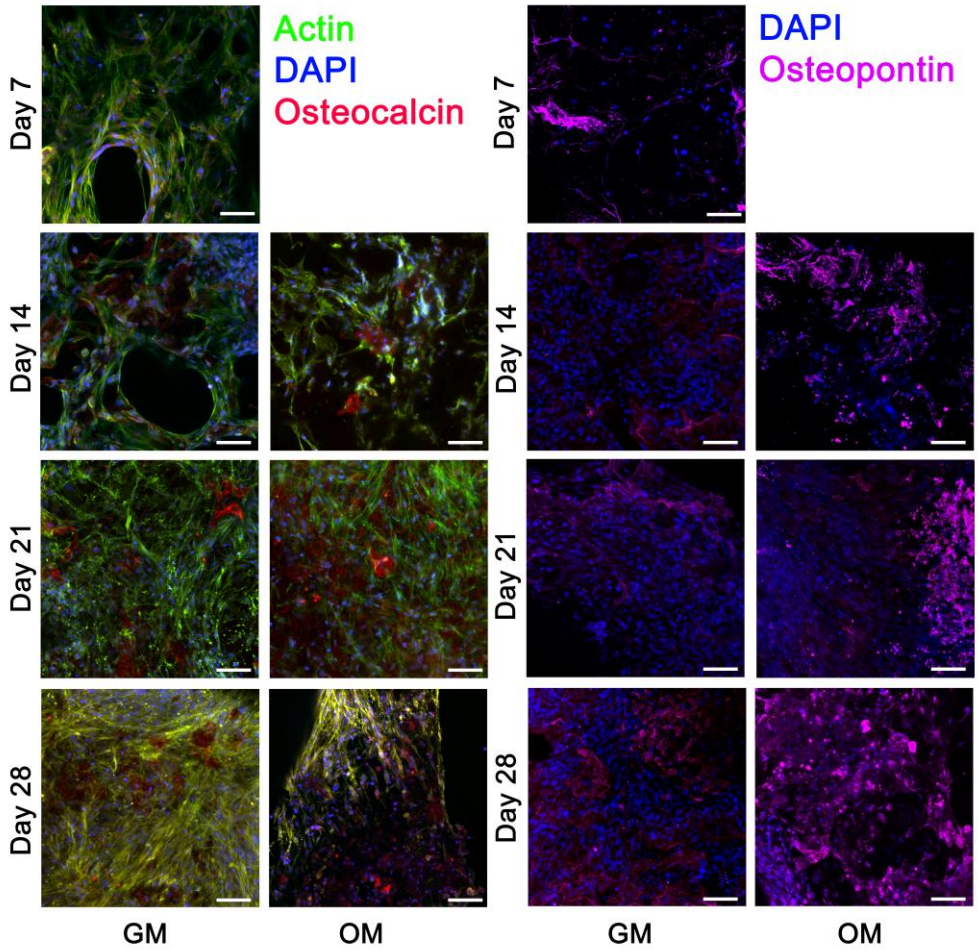

Figure 3.6 Immunofluorescence analysis of hMSC osteogenic differentiation on porous scaffolds. Left panel: actin (green), nuclei (DAPI, blue), and osteocalcin (red), shown for GM (left column) and OM (right column). Right panel: nuclei (DAPI, blue) and osteopontin (magenta), shown for GM (left column) and OM (right column). Scale bars: 100μm.

3.4. Conclusion

In this study, we developed an integrated manufacturing strategy combining microfluidic emulsion templating with extrusion-based AM to fabricate functionally graded porous ceramic scaffolds. By coupling precise droplet generation within ff-MPH with spatially controlled deposition during printing, it was possible to decouple microscale pore templating from macroscale

architectural design. The microfluidic platform enabled the stable, reproducible generation of monodisperse o/w emulsions, allowing programmable control over droplet size and the dispersed-phase volume fraction. These parameters directly defined the pore size and local porosity of the resulting scaffolds. When integrated with embedded printing in an agarose support bath, this approach enabled the deposition of low-viscosity, nHA-loaded emulsions that would otherwise be incompatible with conventional extrusion-based systems. Following UV crosslinking, freeze-drying, and thermal processing, the hybrid printed constructs were successfully converted into fully ceramic scaffolds. MicroCT analysis revealed predictable volumetric shrinkage during sintering while preserving the overall architecture and pore interconnectivity. Furthermore, dynamic modulation of droplet generation during printing enabled the fabrication of scaffolds with spatially graded porosity, demonstrating that microfluidic templating parameters can be directly translated into functionally graded ceramic architectures. Mechanical characterization confirmed that controlled porosity enabled predictable modulation of scaffold stiffness, producing mechanically heterogeneous constructs reminiscent of bone's hierarchical organization. Preliminary biological evaluation further demonstrated that the fabricated scaffolds support cell viability and osteogenic differentiation of hMSC.

Overall, this work establishes a versatile microfluidic-assisted digital manufacturing platform for fabricating hierarchical, functionally graded porous ceramics. By enabling independent control over microscale pore architecture and macroscale geometry, this approach provides a promising technological foundation for the development of next-generation bone-regenerative scaffolds and other architected ceramic biomaterials.

Chapter 4 - Microfluidic-Mixer Assisted 3D Printing of Functionally Graded Multimaterial Hydrogels for Engineering Complex Tissue Interfaces

4.1. Introduction

Biological tissues are inherently heterogeneous systems organized across multiple length scales, spanning from the macroscopic to the molecular level (~ 10^{-1} - 10^{-9} m). This hierarchical complexity becomes particularly evident at tissue interfaces, where two distinct biological environments interface and gradually transition into one another. Rather than presenting abrupt discontinuities, these interfacial regions display spatially orchestrated gradients in structure, composition, and function. Such gradients are essential for mechanical continuity and coordinated cellular activity[150]. The osteochondral interface represents a paradigmatic example of this phenomenon. Here, compliant cartilage progressively transforms into mineralized subchondral bone through continuous variations in extracellular matrix composition, microstructural organization, and cell phenotype. Reproducing this level of structural and biochemical sophistication remains a primary challenge in tissue interface engineering[89].

The key challenge in engineering tissue interfaces is replicating the multiscale hierarchical structure[151]. To emulate native interfacial tissues, scaffolds must incorporate controlled variations in mechanical properties, porosity, and biochemical composition[17,152]. Spherical-based porous functionally graded hydrogels (pFGHs) have emerged as promising candidates in this context, as they allow the integration of compositional and structural gradients within a single construct[6]. Conventional fabrication techniques such as freeze-

drying[153], solvent casting[154], and AM[155] have enabled the production of scaffolds with tunable gradients in density and stiffness. However, these strategies typically lack fine spatial control over microscale porosity and internal architecture-features that are critical for accurately reproducing the hierarchical nature of native tissue interfaces.[89] Microfluidic technologies offer a promising alternative. By generating highly controlled, monodisperse emulsions, microfluidic platforms can template porous hydrogels with tunable internal architecture and mechanical properties[156]. Techniques as step-emulsification[48], T-junction[157], and flow-focusing[134,156] have demonstrated precise control over droplet size and distribution, allowing the formation of pFGHs with a controlled internal architecture. Despite these advances, current systems remain limited in their ability to create multi-material gradients, a key requirement for tissue interfaces. Existing multi-inlet microfluidic approaches for generating composition gradients mostly produce Janus fibers rather than smoothly blended compositions[158]. Passive microfluidic micromixers provide a strategy to overcome this limitation[37]. By promoting controlled mixing of distinct bioinks before extrusion[38], micromixers enable the generation of gradual compositional transitions that more closely resemble native tissue interfaces[150]. When coupled downstream with a flow-focusing junction, such systems can potentially regulate matrix composition and porosity in real time during printing[39,62,159].

In this work, we introduce a microfluidic-assisted 3D printing platform integrating a passive micromixer with a flow-focusing junction within a single printhead (mix-ff-MPH). This configuration enables dynamic control over both the chemical composition of the hydrogel matrix and the density of the internal porous network. The resulting system allows fabrication of spherical-based porous hydrogels with spatially programmable gradients, thereby

providing a versatile tool for engineering complex tissue-like architectures. Preliminary biological assessment demonstrates that regional differences in material composition can modulate 3T3-fibroblast behavior, underscoring the relevance of controlled microenvironmental gradients for advanced biofabrication strategies.

4.2. Materials and Methods

4.2.1. Materials

Dextran from Leuconostoc spp., Mr ≈ 70 000), gelatin (from porcine skin, 300 bloom, Type A), DMSO, GMA, MA, hexadecane (99%), Plantacare 2000, Irgacure 2959, HCl, SnCl2, DMAP, 99%, agarose (Calbiochem™ OmniPur™), Fluorescein isothiocyanate (FITC), rhodamine, PFA, Triton X-100, BSA were purchased from Sigma-Aldrich. PBS, Dulbecco's Modified Eagle Medium (DMEM), FBS, P/S, Phalloidin Alexa Fluor 488, DAPI, and Alexa Fluor secondary antibodies were purchased from Thermo Fisher Scientific. All reagents were used as received unless otherwise specified.

4.2.2. Synthesis of Dextran-Methacrylate

DexMA was synthesized following a previously established protocol[156]. Briefly, dextran (10 g) was dissolved in 90 mL of DMSO under stirring in a round-bottom flask. DMAP (2 g) was separately dissolved in DMSO and added to the dextran solution, followed by the addition of GMA (4 mL), corresponding to approximately 50% molar substitution relative to the repeating units of dextran. The reactants were stirred gently (100 RPM) and left to react in the dark at RT for 48 hours. The reaction mixture was stirred at 100 rpm for 48 h at RT in the absence of light. The reaction was quenched by

adding an equimolar amount of HCl to neutralize the catalyst. The resulting solution was transferred to dialysis tubing (MWCO 1 kDa) and dialyzed against deionized water for five days until stable conductivity (18 MΩ·cm) was reached. The purified solution was freeze-dried and stored at 4 °C until use.

4.2.3. Synthesis of Gelatin-Methacryloyl

GelMA was synthesized using a previously documented protocol.[156] Gelatin was dissolved in PBS at 10% (w/v) at 50 °C under continuous stirring. MA was then added dropwise (0.8 mL per gram of gelatin) while maintaining vigorous stirring (500 rpm). The reaction proceeded for 3 h at 50 °C. The modified gelatin solution was subsequently dialyzed (MWCO 14 kDa) against deionized water at 50 °C until the conductivity stabilized at 18 MΩ·cm. After dialysis, the solution was freeze-dried and preserved at 4 °C before further use.

4.2.4. Preparation of 3D printing Supporting bath

Agarose fluid-gel was prepared as a printing support medium following a standardized protocol[102]. Briefly, agarose powder (0.5 g) was dispersed in 100 mL of deionized water and sterilized by autoclaving at 121 °C for 20 minutes. After autoclaving, the solution was cooled to RT under continuous stirring at 700 rpm for 12 h to obtain a homogeneous fluid-gel suspension. The supporting bath was maintained at RT until printing.

4.2.5. Fabrication of Polycarbonate Microfluidic Chip

The microfluidic chip integrating the micromixer and flow-focusing unit was fabricated from 5 mm thick polycarbonate sheets using CNC micromilling

(MSG402, ErgWind, Poland)[137]. The device design included two continuous-phase inlets and one dispersed-phase inlet (250 μm width), a mixing channel of 400 μm width with 5 mm repeating units, a flow-focusing orifice of 100 μm, and an outlet channel of 500 μm width. Channel depth was fixed at 200 μm. A 25 G needle was coupled to the outlet channel to enable extrusion. After milling, the polycarbonate substrates were sonicated in isopropanol for 30 minutes to remove debris and contaminants. The layers were then thermally bonded in a hot press at 130 °C for 30 minutes. To minimize interactions between the polycarbonate walls and the dispersed organic phase[103], the internal surfaces were treated with a 20% (w/v) $SnCl_2$ solution in ethanol. The solution was flushed through the channels at 20 mL/h for 2 h at 60 °C, followed by thorough rinsing with deionized water.

4.2.6. Rheological Measurement

The rheological behavior of the continuous phase formulations (DexMA + Plantacare, GelMA + DexMA + Plantacare, and agarose fluid gel) was investigated using a rotational rheometer (Malvern Kinexus Pro) equipped with a cone–plate geometry. Measurements were conducted at 35 °C to replicate the printing conditions while preventing thermal gelation of GelMA. The shear behavior of the samples was assessed by applying shear rates ranging from 1 to 10^3 Hz. Viscosity profiles were recorded to evaluate flow behavior under processing-relevant conditions.

4.2.7. Microfluidic mixing and emulsion generation

Before each experiment, both aqueous and organic phases were filtered through 0.22 μm syringe filters to prevent channel obstruction. The micromixer was used to passively mix the two aqueous biomaterial inks (20%

DexMA + 1% Plantacare + 1% Irgacure 2959 and 10% GelMA + 2% DexMA + 1% Plantacare + 1% Irgacure 2959). The mixed aqueous solution was then used as a continuous phase to produce an O/W emulsion using a flow-focusing junction, with hexadecane as the dispersed phase. The mixing of the continuous phases and the droplet generation were precisely controlled by varying the flow rates of the different phases using microfluidic pumps (neMESYS, Cetoni GmbH). All porous materials were printed with a dispersed phase volume fraction (φ_D) in the range of 0.2-0.8, and the total flow rate of the two phases was adjusted to 20 μL/min. Emulsion formation and mixing behavior were monitored using a high-speed camera (IDS, Germany) operating at 165 fps with 1× magnification.

4.2.8. Mixing Index

The mixing efficiency within the microfluidic printhead was quantified using the Mixing Index (MI), calculated from fluorescence intensity distributions across a cross-sectional plane perpendicular to the flow direction. For a selected cross-section, the MI was defined as:

$$MI = 1 - \frac{\sqrt{\frac{1}{N}\sum_{i=1}^{N}(C_i - \bar{C})^2}}{\bar{C}} \quad \textbf{(Eq.4.1)}$$

Where N is the number of sampling points in a chosen cross-section, C_i is the point concentration (calculated from pixel intensity) of the analyzed specimen, and C is its mean concentration along the cross-section.

In view of its application in 3D printing of scaffold for cell seeding, the mixing performance of five different microfluidic printheads (MPH) (**Figure 4.1**) was tested using two solutions with different viscosities at 35 °C (**Figure 4.2**). The

continuous-phase solutions were introduced at a combined flow rate of 14 µL/min, which was the maximum continuous-phase flow rate used during printing. To assess mixing performance under varying compositional conditions, GelMA:DexMA ratios of 100:0, 80:20, 50:50, 20:80, and 0:100 were tested. For example, under the 80:20 condition, flow rates of 11.2 µL/min (GelMA) and 2.8 µL/min (DexMA) were applied (**Table 1**). For imaging purposes, to distinguish between the two colorless biomaterial inks, DexMA was labeled with rhodamine, and GelMA with Fluorescein Isothiocyanate (FITC). Confocal microscopy images were acquired and processed to calculate MI values.

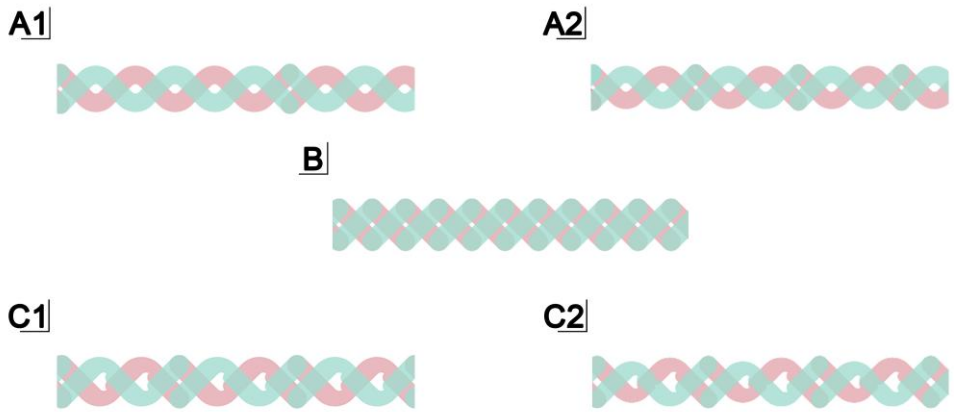

Figure 4.1 Schematic representation of different microfluidic micromixer geometries composed of two superimposed layers (red and green). **A1, A2, B)** two serpentine channels with forced helixes varying in the length and geometry of the repeating unit. **C1, C2)** incorporate additional obstacles and barriers into the split-and-recombine structure.

	Flow rate(µl/min)	
Emulsion fibers composition GelMA:DexMA	*GelMA*	*DexMA*
100:0	14	0
80:20	11.2	2.8
50:50	7	7
20:80	2.8	11.2
0:100	0	14

Table 4.1 Flow rate for each solution supplied to the micromixer for analysis of MI.

4.2.9. Emulsion 3D printing of Cubic Porous Scaffold and Complex Geometries

A custom-made 3D printer was used to fabricate the FGPSs, with the neMESYS software controlling three microfluidic pumps (neMESYS, Cetoni GmbH) connected to the 3D printer. The deposition of emulsion fibers in 3D was achieved using a linear-axis system arranged in a Cartesian configuration, driven by a stepper motor. All printing was performed inside a temperature-controlled chamber maintained at 35 °C. To standardize the 3D printing process and conduct a comparative analysis of gradient emulsion printing, 3D cubes were printed in an agarose fluid-gel bath. The 3D structures that are impossible to print in air with an overhang >45° were printed using porous

fibers in agarose fluid-gel at a print speed of 3.3 mm/s (F200). Standard cubic constructs (7 × 7 × 7 mm^3) and complex geometries were designed in the CAD program Autodesk Inventor and subsequently sliced (0.3 mm layer thickness) using the STL-to-G-code conversion software Slic3r. To automate the creation of different porosities within the same geometry and distinct degrees of mixing for the continuous phases, a Script function was developed in neMESYS. The code precisely controlled the microfluidic pumps to achieve the required flow rates, thereby automating the formation of the dispersed phase's volume fractions. To visualize gradients in printed geometries, a fluorescent dye was incorporated into hydrogel solutions.

4.2.10. Scaffold cross-linking and purification

Irgacure 2959 was employed as a radical photoinitiator in the external phase to enhance crosslinking of the methacrylated biopolymer chains (DexMA and GelMA). The 3D printing was conducted in the dark to prevent radical initiators from premature cross-linking. The printed scaffolds were cross-linked using a UV lamp (λ = 365 nm) for 10 minutes after the emulsions were printed in the agarose supporting solution. The crosslinked constructs were then collected from the agarose fluid-gel with a spatula, and the internal organic phase (hexadecane) was eliminated by immersing them in a DMSO solution for over three days. Subsequently, scaffolds were rinsed with distilled water until nominal conductivity was achieved.

4.2.11. Fourier Transform Infrared Analysis

Fourier Transform Infrared (FTIR) spectra of the DexMA-GelMA gradient samples were recorded using a Nicolet 8700 spectrometer (Thermo Fisher Scientific, USA). FTIR analysis, based on changes in the vibrational energy

of molecular grafts, enables the identification of functional groups and molecular structures. This qualitative technique correlates specific wavenumber regions with characteristic chemical bonds. To obtain each spectrum, scans were acquired over the 400–4000 cm^{-1} range at a resolution of 4 cm^{-1}. Single-material and gradient scaffolds were 3D-printed, crosslinked, and freeze-dried prior to analysis using an FTIR instrument. Slices (approximately 2 × 2 mm) were manually dissected from predefined positions along the z-axis of the 3D printed gradient scaffolds before FTIR acquisition.

4.2.12. X-ray computed tomography analysis

Morphological analysis of 3D-printed samples was performed microCT, using Skyscan 1172 (Bruker, USA) with a scanning voltage of 40 kV, power of 10 W, and a rotation step of 0.50° over an angle range of 192.50°. Image smoothing and noise reduction were performed via NRecon software (Bruker, USA). Data analysis and 3D reconstruction of the models were performed with ImageJ software (National Institutes of Health, USA).

4.2.13. Mechanical testing

Compressive mechanical testing was performed using a DMA Q800 (TA Instruments, New Castle, DE, United States) to evaluate the scaffolds' Elastic Modulus. A static force of 0.001 N was applied before testing. The compression test was conducted at RT using a ramp strain rate of 5%/min to 30%. The tested samples had cylindrical dimensions with a base diameter of 7 mm, while the software automatically detected the sample height. Samples were selected to have either single (GelMA or DexMA) or bi-composite material formulation with defined ratios of the two components

(DexMA:GelMA = 80:20, 60:40, 40:60). The Young's modulus of each sample was identified as the slope of the linear elastic part of the stress-strain curve, in the range of 3-5% strain.

4.2.14. Culture of 3T3-fibroblast and cytocompatibility testing

3T3-fibroblasts were cultured in basal DMEM supplemented with 10% FBS and 1% P/S. Before seeding, scaffolds were sterilized by exposure to UV light for 2 h. Cells were detached using 0,25% trypsin-EDTA, centrifuged at 300 x g for 5 minutes at RT, and suspended in media at a concentration of 10^6 cells/mL. Each scaffold (7x7x2 mm) was inserted into a 1.5mL sterile tube and completely submerged in 500 µL of cell suspension, resulting in a final seeding of 5×10 ^5 cells per scaffold. Then, the tubes containing the samples were placed on a rotating stage in the incubator for 1 h to achieve homogeneous cell distribution and seeding. Finally, scaffolds were moved to a 24-well plate and cultured under standard conditions (37 °C, 5% CO_2). The medium was changed every 48 hours.

4.2.15. Live/dead assay

The viability of 3T3-fibroblasts was evaluated using LIVE/DEAD Cell Imaging kit 488/570 (Invitrogen) after 1 and 7 days of cell culture. At the desired time points, according to the manufacturer's protocol, the cell-seeded 3D-printed constructs were stained with the Live/Dead assay solution and incubated for 15 min at RT. Subsequently, image acquisition was performed using a confocal microscope (Nikon A1R) with 488 nm and 561 nm laser sets to detect living and dead cells, respectively. The images were acquired with 10x magnification and the Grab Large Image option to obtain an overview of the entire scaffold.

4.2.16. Immunofluorescence (IF) staining

3D printed scaffolds seeded with 3T3 fibroblasts were fixed using 4% v/v PFA in PBS overnight at 4°C. The cells were permeabilized with 0.2% v/v Triton X-100 in PBS for 30 minutes at RT, followed by blocking of non-specific binding with 1% (v/v) BSA in PBS for 2 hours at RT. The scaffolds were stained to evaluate the cell attachment and collagen I deposition. Actin filaments were labeled with Alexa Fluor 488-conjugated Phalloidin (Sigma, Germany) (1:40 v/v in 1% BSA solution) for 2 hours at RT. For collagen I staining, samples were incubated overnight at 4°C with a primary anti-collagen I antibody (Sigma, Germany, rabbit-derived) (1:100 v/v in 1% BSA solution). After two washes in PBS (5 minutes each), samples were incubated with a Texas Red-conjugated anti-rabbit secondary antibody (1:150 v/v in 1% BSA solution) for 2 hours at RT. Finally, nuclei were counterstained with DAPI (Invitrogen) (1:1000 in 1% BSA solution) for 10 minutes at RT. IF images were acquired using a Nikon A1R confocal microscope, while image analysis was performed using ImageJ software (National Institutes of Health, USA).

4.2.17. Cell density determination

Cell density within the scaffolds at different time points was determined by analyzing confocal stacks in ImageJ. Areas of 638 x 638 μm^2 were analyzed along z-axis. Cell number was normalized to the analyzed scaffold volume.

4.2.18. Statistical Analysis

For statistical analysis, GraphPad Prism (GraphPad Software Inc., La Jolla, CA) was used. Either a one-way ANOVA or a two-way ANOVA was used to

determine differences between groups. Significantly different data were identified as $p < 0.05$.

4.3. Result and discussion

4.3.1. Micromixer and flow-focusing microfluidic printhead

Recent developments in microfluidic-assisted AM have demonstrated the potential of droplet-templating strategies to fabricate porous hydrogels with controlled internal architectures[48,134]. In particular, flow-focusing systems enable the generation of monodisperse emulsions, which can subsequently be solidified to obtain spherical porous constructs with defined pore size and density. Moreover, these platforms allow rapid switching between different inks in a continuous manner, resulting in heterogeneous structures with alternating or co-extruded spatial bioink patterns[48,156,160]. However, most of the currently available systems are limited to discrete material transitions or side-by-side extrusion configurations. Such approaches do not allow the formation of smooth, continuous compositional gradients within a homogeneous matrix, which are essential for reproducing the gradual transitions typical of native tissue interfaces[158].

To overcome this limitation, we designed a novel microfluidic printhead, referred to as mix-ff-MPH, that integrates a passive micromixer upstream of a flow-focusing junction (**Figure 4.2a**). The objective was to decouple and independently control two key parameters of the printed scaffold: (i) matrix chemical composition, regulated through controlled mixing of two continuous phases, and (ii) pore architecture, determined by the dispersed-phase volume fraction during emulsion generation. The printhead geometry included two inlets dedicated to the continuous phases, which converged into a serpentine-

based passive micromixer, followed by a single dispersed-phase inlet connected to a flow-focusing junction. This configuration enabled real-time blending of polymeric solutions before droplet formation. The operational window of the flow-focusing unit was defined in accordance with **Chapter 2**[156]. We used DexMA or GelMA, supplemented with Plantacare as the surfactant, as the continuous phase. As the dispersed phase, we used Hexadecane. A total flow rate of 20 μL/min was selected, as it provided stable emulsion formation without flow instabilities. By maintaining this constant overall flow rate and modulating the ratio between continuous and dispersed phases, dispersed-phase volume fractions (φD) between 0.2 and 0.8 were achieved. This resulted in droplet diameters ranging approximately from 100 to 400 μm, consistent with previously reported data[48].

To optimize mixing efficiency, five different micromixer geometries were fabricated and experimentally evaluated (**Figure 4.2a**). The versions A1, A2, and B (**Figure 4.3)** consist of two serpentine channels with forced helices varying in the length and geometry of the repeating unit. Versions C1 (**Figure 4.3**) and C2 (**Figure 4.2a**) incorporate additional obstacles and barriers into the split-and-recombine structure. Variations included changes in the length of the repeating units and the presence of internal obstacles to enhance streamlined stretching and folding[161,162]. Passive micromixers rely exclusively on geometrical constraints to promote chaotic advection and increase interfacial area between fluid streams. Therefore, mixing efficiency strongly depends on channel architecture and fluid properties. From an engineering perspective, selecting an efficient geometry is critical not only for maximizing mixing performance but also for minimizing mixer length. Reducing mixer volume directly decreases dead time and improves synchronization between compositional modulation and extrusion during printing[48].

The mixing performance of each geometry was evaluated using fluorescently labeled polymer solutions (20% w/v DexMA-rhodamine and 10% w/v GelMA-FITC). Rheological characterization (**Figure 4.2b**) at 35 °C confirmed that both solutions exhibited moderate shear-thinning behavior, with viscosities in the order of 10^1–10^3 mPa under relevant shear conditions. This temperature was selected to reproduce printing conditions while preventing premature GelMA gelation[163]. The solutions were supplied to the mix-ff-MPH, and fluorescence images were taken with a confocal microscope to analyze the MI. Experiments were conducted at a combined flow rate of 14 μL/min, corresponding to the maximum continuous-phase flow used during printing. Five volumetric ratios (100:0, 80:20, 50:50, 20:80, and 0:100 GelMA:DexMA) were tested. (**Figure 4.2c**). The results demonstrated that micromixer geometry significantly influenced mixing efficiency, with MI values ranging from approximately 0.7 to above 0.8. Among the tested configurations, the C2 geometry consistently achieved MI ≥ 0.8 across all compositional ratios and was therefore selected for subsequent printing experiments (**Figure 4.2d**). Additional MI measurements collected at 7, 21, and 28 μL/min for the selected mixer geometry are shown in **Figure 4.4**, demonstrating consistent mixing performance across a broader flow-rate range. Compared to a previously implemented serpentine mixer in our laboratory[112], which yielded MI ≤ 0.6 with alginate-based systems, the present configuration achieved at least a 20% improvement. This enhancement can be attributed to the combined effect of optimized channel architecture and the rheological characteristics of the employed polymer solutions. These findings align with established design principles, indicating that mixer performance is highly dependent on both geometric complexity and fluid viscosity[164]. Following optimization of the mixing unit, we evaluated the integration of the micromixer with the downstream flow-focusing junction. As reported in

Figure 4.2e, stable O/W emulsions were successfully generated across the entire investigated φD range (0.2–0.8). Importantly, modulation of the continuous-phase composition upstream directly translated into controlled compositional variations in the emulsion matrix, as visually confirmed by the gradual transition in fluorescent signals. This result demonstrates that the mix-ff-MPH enables simultaneous regulation of matrix composition and pore architecture within a single integrated device, establishing a robust foundation for the fabrication of spatially graded porous hydrogels.

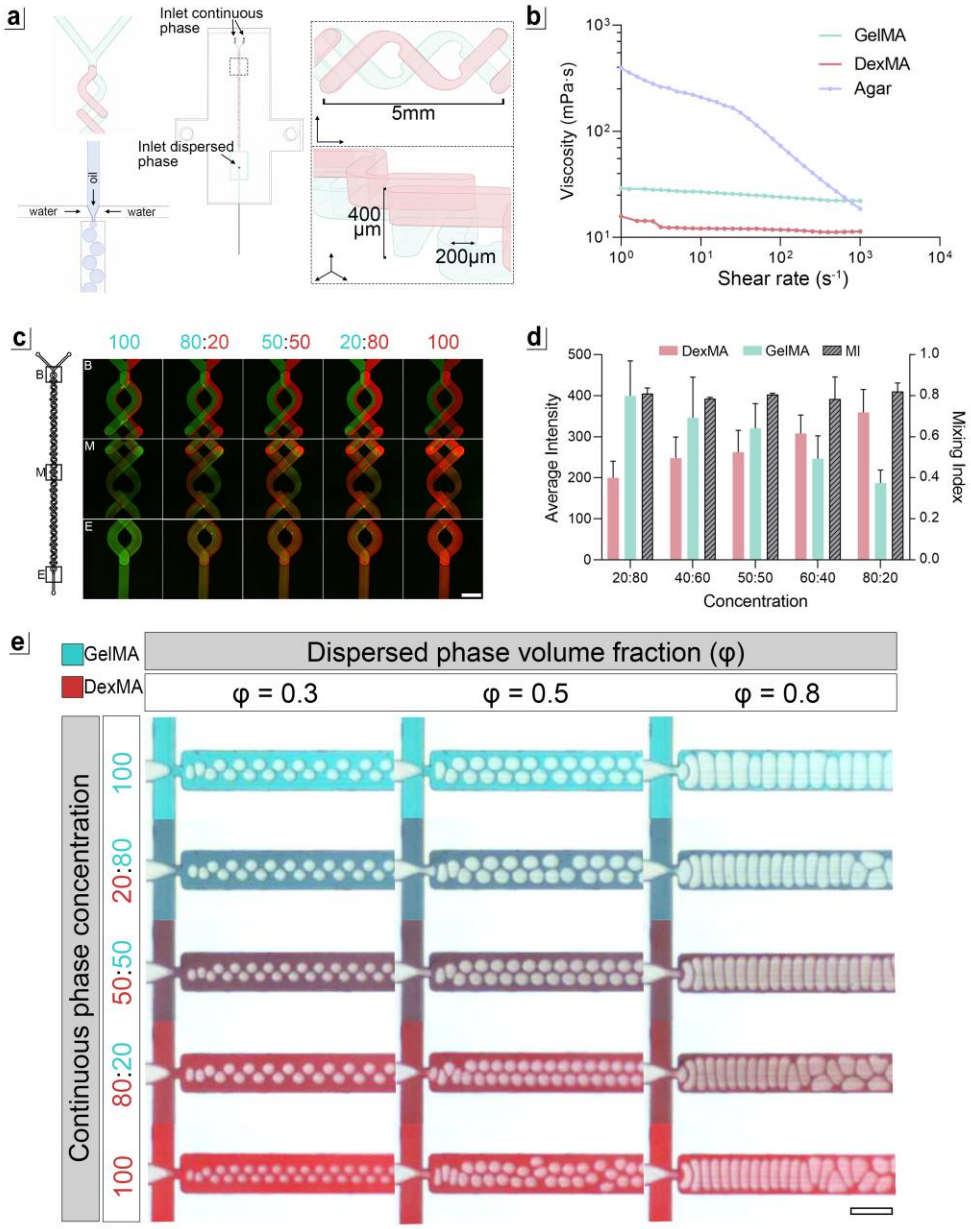

Figure 4.2 mix-ff-MPH bearing a passive micromixer. **a)** Schematic representation of the flow-focusing microfluidic chip (C2) with relative cross sections. **b)** Rheological characterization of the agarose fluid-gel, DexMA, and GelMA solutions. **c)** Confocal images of different points of the micromixer beginning (B), middle (M) and end (E) captured at different mixing ratio DexMA (red):GelMA (green). **d)** Analysis of MI (gray column) and Average Intensity (green and red column). **e)** Microfluidic production of the emulsions at various volume fractions of the dispersed phase ($0.2 < \varphi < 0.8$) and at various ratios between two different polymeric solutions DexMA (red) and GelMA (green). Scale bar c) 800 µm, e) 500 µm.

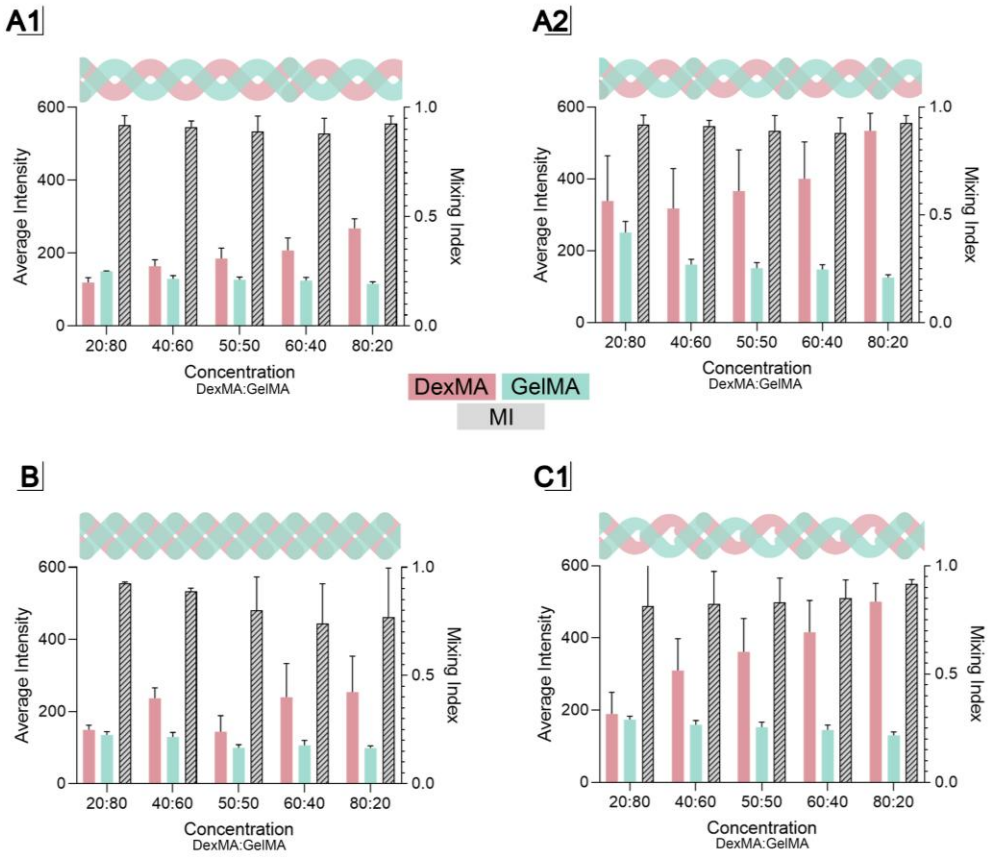

Figure 4.3 Analysis of MI (gray column) and average Intensity (green and red columns) for 4 different geometries of microfluidic micromixer. For each mixer geometry (shown on top of the graph), the graph reports the Average Intensity and MI for the two solutions injected in the micromixer DexMA (red) and GelMA (green).

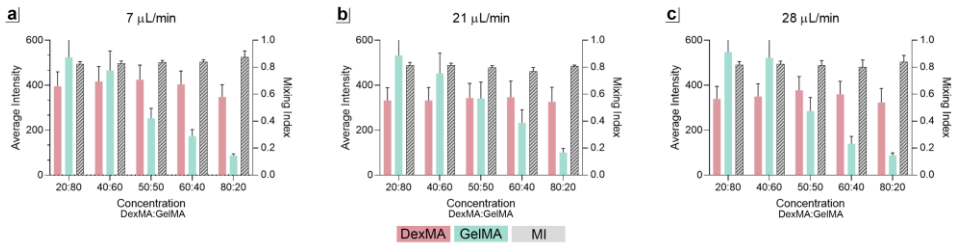

Figure 4.4 Analysis of MI (gray column) and average Intensity (green and red columns) for 3 different flow rates (7, 21, and 28 µL/min). For each flow rate, the graph reports the Average Intensity and MI for the two solutions injected in the micromixer DexMA (red) and GelMA (green).

4.3.2. 3D printing

The ability to simultaneously regulate matrix composition and pore density significantly expands the fabrication capabilities of pFGHs. From a manufacturing standpoint, this dual control enables the production of constructs with spatially tunable physicochemical properties, including mechanical stiffness, swelling behavior, and cell–matrix interaction potential. Such flexibility is particularly relevant when aiming to recreate the gradual transitions that characterize native biological tissues. To experimentally validate the proposed approach, the customized 3D printer was equipped with the mix-ff-MPH (**Figure 4.5a**) and operated inside a temperature-controlled chamber maintained at 35 °C. By synchronizing the microfluidic flow rates with the printhead's coordinated movement, it was possible to fabricate hydrogels with controlled gradients in composition and porosity. Printing was performed in an agarose fluid-gel bath, which served as a temporary support medium. This strategy enabled stable deposition of soft emulsion-based inks that would otherwise lack sufficient viscoelasticity for printing in air[102]. The supporting bath effectively maintained structural integrity during extrusion and prevented collapse of overhanging features.

To first assess the system's ability to modulate local material composition, a two-layer grid structure (**Figure 4.5b**) was printed using fluorescently labeled DexMA (rhodamine) and GelMA (FITC). The compositional ratios of the continuous phase were dynamically adjusted during printing. Confocal imaging of the deposited filaments revealed distinct, spatially controlled variations in fluorescence intensity corresponding to the programmed mixing ratios. These results confirm that the integrated micromixer reliably blends polymer solutions before extrusion, enabling predictable control over the local matrix composition. Subsequently, the platform's ability to generate continuous gradients along the printing direction was evaluated by fabricating cubic constructs ($7 \times 7 \times 7$ mm³). To verify compositional transitions within the bulk structure, FTIR analysis was performed on sections collected at predefined positions along the z-axis (**Figure 4.5c** and **Figure 4.6**). Particular attention was given to the amide I band of gelatin (~1627 cm^{-1}), associated with C=O stretching vibrations of the peptide backbone. Progressive variations in peak intensity were observed along the scaffold height, consistent with the programmed DexMA-to-GelMA gradient. The absence of abrupt spectral changes supports a smooth compositional transition, confirming effective inline mixing during printing.

In addition to chemical gradients, the system allows independent modulation of scaffold porosity by adjusting the dispersed-phase volume fraction. To demonstrate this capability, both simple cubic geometries and more complex architectures featuring overhang angles exceeding 45° were printed (**Figure 4.5d**). The ability to fabricate such structures highlights the stability of the printing process within the agarose support bath. As visible in **Figure 4.5d,** fluorescent labeling of the continuous phase further enabled qualitative visualization of density variations. Regions with higher fluorescence intensity

corresponded to lower porosity (higher polymer content), whereas regions with lower fluorescence intensity corresponded to higher porosity. Importantly, density modulation was achieved while maintaining a constant compositional gradient between GelMA and DexMA, demonstrating independent control of these two parameters.

After purification and removal of the internal oil phase, the printed constructs were analyzed using microCT to assess structural fidelity and internal architecture. Three-dimensional reconstructions reported in **Figure 4.5e–f** confirmed accurate reproduction of the designed geometries and preservation of pore interconnectivity throughout the scaffold volume. For comparison, a two-layer reference scaffold with discrete porosity values (30%–70% porosity, **Figure 4.5e**) exhibited a sharp transition between regions characterized by distinct pore morphologies. In contrast, constructs featuring a continuous porosity gradient from 30% to 70% (**Figure 4.5f**) displayed a gradual evolution in pore size and density along the printing direction, without detectable discontinuities. Pore size distribution analysis further supported these observations. These findings demonstrate that the mix-ff-MPH platform enables precise spatial control over both matrix composition and internal pore architecture within a single continuous manufacturing process.

Of note, the modular design of the printhead was further extended to accommodate three continuous-phase inlets. In this configuration, three differently pigmented polymer solutions (blue, yellow, and red) were simultaneously injected into the micromixer. As illustrated in **Figure 4.5g**, the resulting printed structures exhibited smooth color transitions, independent of geometry complexity or extrusion sequence. This result highlights the system's

scalability and its potential for multi-material gradient fabrication beyond binary systems.

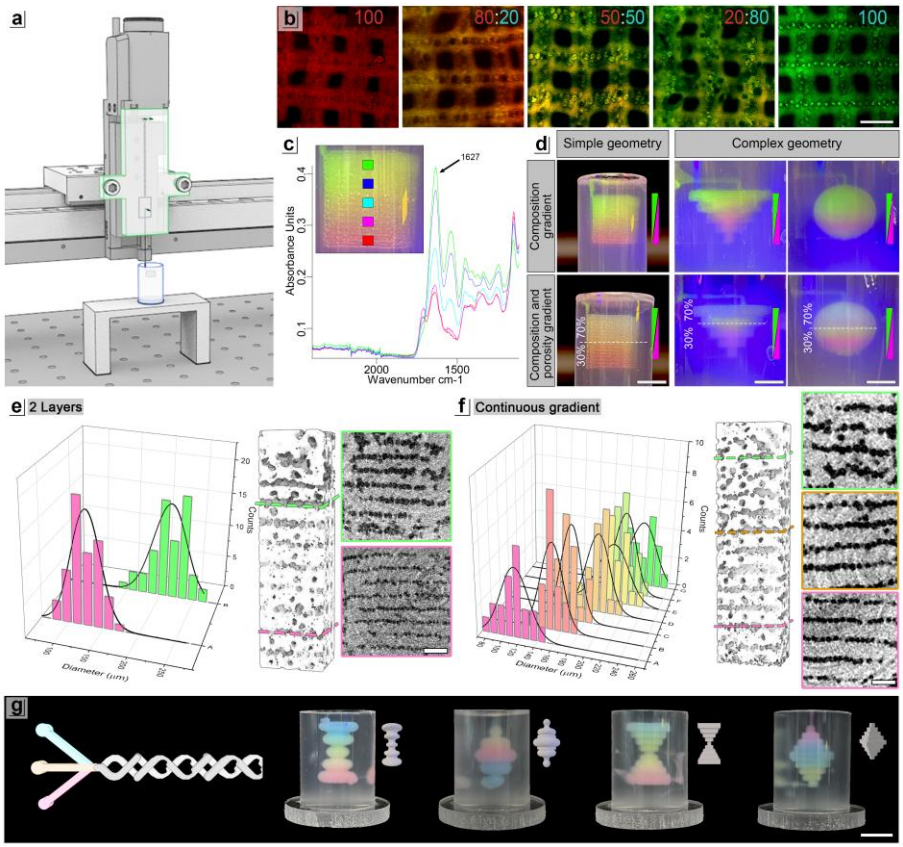

Figure 4.5 Operational set-up. **a)** Schematic representation of 3D printer with the mix-ff chip as printhead. **b)** Confocal images of 3D printed grids of mixed compositions of DexMA:GelMA at various mixing ratios: 100:0,80:20, 50:50, 20:80,0:100, reporting the efficiency of the mixing. **c)** FTIR spectra at specific points of DexMA:GelMA gradient samples. **d)** 3D printed porous structures inside the agarose fluid-gel bath that were printed using two different fluorescent dyes in the continuous phases (the first line exhibits a graded transition between two colors, indicating a compositional gradient between two materials along the z-axis. In the second line, while the compositional gradient remains consistent with the first line, a density gradient is introduced. This density variation is evident in the fluorescence intensity of the dyes: regions with a stronger fluorescence signal correspond to higher density (low porosity), whereas regions with a weaker fluorescence signal indicate lower density (high porosity)). **e-f)** microCT analysis of pFGMs. Three-dimensional reconstruction of the scaffold obtained from X-ray image stacks and a representative horizontal cross-section (right), together with the corresponding pore size distribution (left). **g)** Schematic representation of 3 inlets micromixer and 3D printed complex geometries with gradient composition evidenced by smooth gradient of color. Scale bars: b) 1mm, d) 5mm e) 1mm f) 500µm g) 1mm.

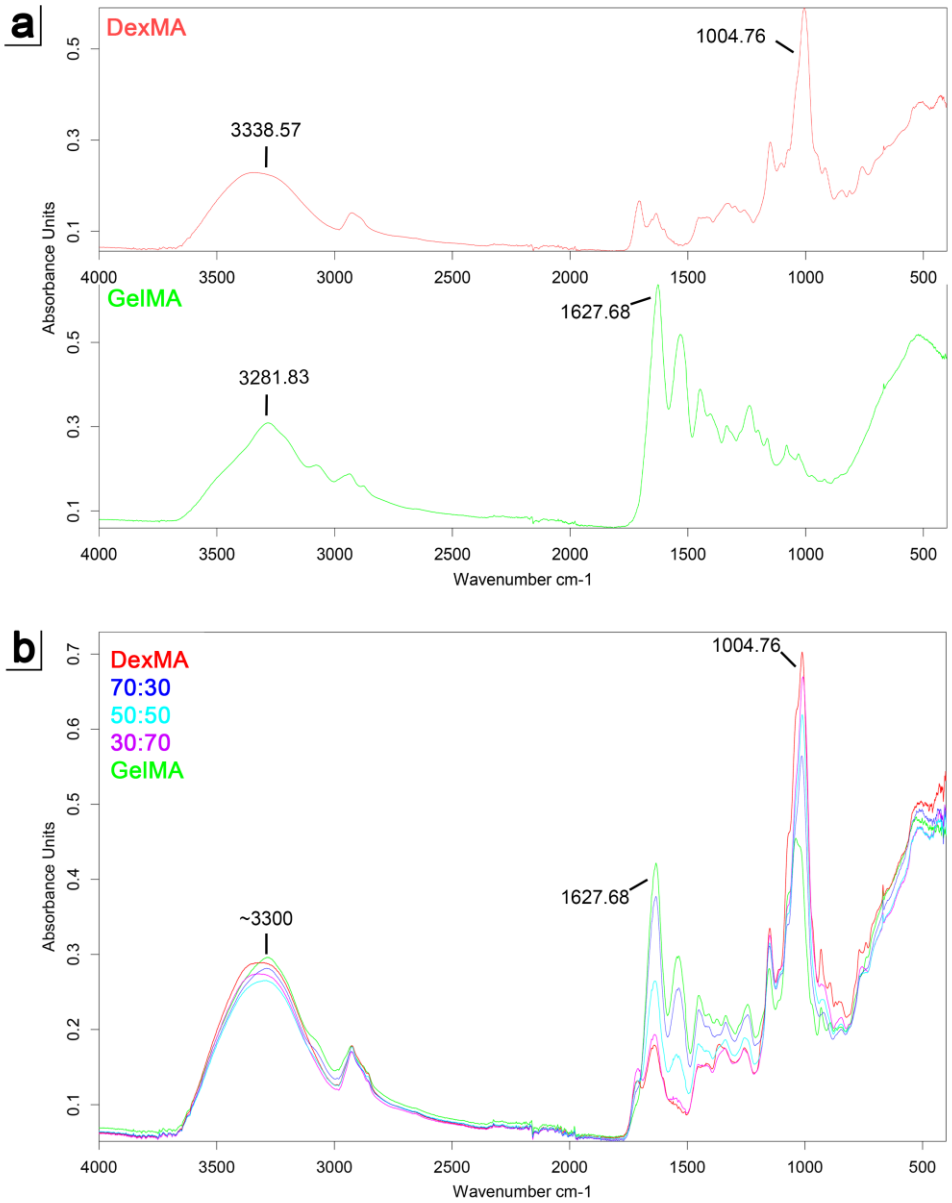

Figure 4.6 FTIR spectra of GelMA/DexMA pFGMs. **a)** FTIR spectra of GelMA and DexMA. **b)** FTIR spectra at specific points of DexMA:GelMA gradient samples – e.g., 70:30 means spectra recorded at the cross-section of the sample at ~25% of sample height.

4.3.3. Cell viability on the heterogeneous scaffold

Following validation of the micromixer's performance and the successful fabrication of scaffolds with continuous 3D compositional gradients, we investigated the biological response of cells to the heterogeneous microenvironment generated by the mix-ff-MPH platform.

Prior to biological evaluation, printed scaffolds were thoroughly purified to remove residual surfactant and dispersed oil phase and subsequently sterilized under UV light. This ensured a suitable and controlled environment for cell culture experiments. 3T3 fibroblasts were then seeded onto gradient hydrogels characterized by a continuous transition from 100% DexMA at the bottom region to 100% GelMA at the top. These two biomaterial inks were intentionally selected due to their markedly different biochemical and mechanical characteristics. GelMA is widely recognized for its intrinsic cell-adhesive properties, biodegradability, and relatively compliant mechanical behavior, making it a common material for tissue engineering applications.[165] In contrast, DexMA hydrogels, while cytocompatible, are mechanically stiffer and lack inherent adhesive motifs, resulting in limited cell–matrix interactions.[166]

Live/Dead staining performed after 1 and 7 days of culture demonstrated overall high cell viability (>80%) throughout the gradient scaffold (**Figure 4.7a**). Notably, a distinct change in cellular organization was observed approximately one-third of the scaffold height, as indicated by the yellow reference line in the cross-sectional images (**Figure 4.7a**). This transition corresponds to the region where the GelMA fraction becomes sufficiently dominant to influence cell adhesion behavior. As shown in **Figure 4.7b**,

quantitative cell counting along the gradient confirmed a progressive increase in cell number toward the GelMA-rich region. This trend is consistent with the presence of Arg-Gly-Asp (RGD) sequences in GelMA, which enhance integrin-mediated adhesion and promote cell spreading.[165] In contrast, cells located within the DexMA-dominant region displayed a markedly different morphology. Rather than spreading on the scaffold surface, they tended to localize within the pores and form rounded aggregates, suggesting limited substrate adhesion. The graded construct, therefore, enabled simultaneous observation of cellular responses across a continuous spectrum of biochemical composition and mechanical properties within a single sample. Such a configuration provides a powerful platform for screening cell–matrix interactions under spatially varying conditions, reducing the need for multiple independent formulations.

To further elucidate the relationship between composition, mechanical properties, and cell behavior, homogeneous scaffolds composed of single materials (100% GelMA or 100% DexMA) or defined blends (DexMA:GelMA = 100:0, 80:20, 50:50, 40:60, 0:100) were fabricated and mechanically characterized. Compression testing revealed a pronounced variation in Young's modulus across formulations (**Figure 4.8a**). In particular, the 80:20 DexMA:GelMA formulation exhibited a modulus approximately 2.5 fold higher (~400 kPa) than the 60:40 blend. A progressive decrease in stiffness was observed with increasing GelMA content, reflecting the softer nature of GelMA-based hydrogels. These mechanical differences are directly reflected in the cellular responses observed. This result indicates significant differences in mechanical properties among the various compositions: as DexMA content decreases, Young's modulus rapidly decreases, resulting in increasingly softer hydrogel matrices. This trend is consistently reflected in

subsequent cell behavior observed in the experiments. It is well known that substrate stiffness is a crucial regulator of cellular processes such as adhesion, spreading, migration, and cytoskeletal remodeling.[165]

3T3-fibroblast adhesion analysis at day 7 (**Figure 4.8b**) demonstrated minimal fibroblast attachment on 100% DexMA scaffolds. Confocal imaging confirmed low cell density and predominantly rounded morphology in this condition (**Figure 4.8c**), with limited F-actin organization and absence of well-defined cytoskeletal structures. These observations indicate insufficient adhesion and spreading on the DexMA substrate. With increasing GelMA content, fibroblast attachment and spreading progressively improved. In the 80:20 formulation, cell distribution appeared heterogeneous, with localized clusters interspersed with sparsely populated regions. This trend became more pronounced in the 60:40 and higher GelMA formulations, culminating in the 100% GelMA scaffold, which exhibited dense and uniform cellular coverage. Collagen type I (Col I) deposition followed a similar trend (**Figure 4.8d**). Regions with higher cell density exhibited stronger collagen expression, indicating active matrix remodeling. Additionally, enhanced cytoskeletal organization was evident in GelMA-rich samples, where well-developed stress fibers and elongated morphologies were observed (**Figure 4.8c–e**), reflecting improved mechanotransduction and cell–matrix engagement. These findings suggest the existence of a compositional and mechanical threshold that governs the switch from limited adhesion to active spreading and matrix production. Substrate stiffness and biochemical cues act synergistically in regulating fibroblast behavior, influencing adhesion, cytoskeletal remodeling, and extracellular matrix synthesis.

To further investigate the influence of scaffold architecture on three-dimensional cell distribution, highly porous scaffolds (up to 70% porosity, pore size ~300 μm) were fabricated. In these constructs, extensive cell infiltration throughout the scaffold thickness was observed (**Figure 4.8e–f**), demonstrating effective 3D colonization. Scaffolds with lower porosity (30%) also supported cell attachment; however, cellular penetration was comparatively limited, likely due to reduced pore interconnectivity.

Overall, the DexMA:GelMA gradient configuration introduces an additional level of functional complexity, enabling evaluation of cellular responses within a spatially heterogeneous microenvironment. These results underline the importance of balancing composition, mechanical properties, and pore architecture to achieve effective three-dimensional cell colonization. While 3T3 fibroblasts were employed as a preliminary validation of the fabricated pFGHs, the proposed microfluidic-assisted 3D printing platform holds potential for more advanced biological investigations, including co-culture systems and interface-mimicking tissue models.

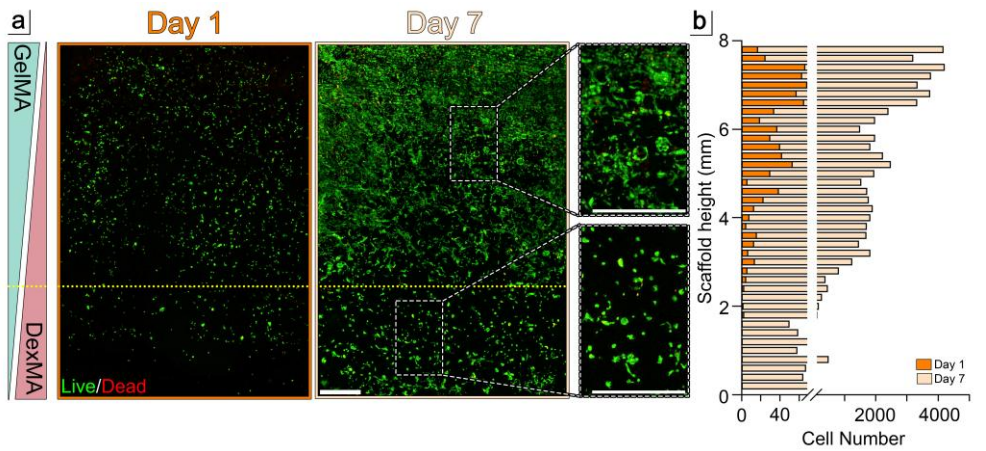

Figure 4.7 3T3 fibroblast adhesion on a functionally graded hydrogel, 30% porosity. **a)** Live/Dead staining of gradient sample DexMA(bottom) to GelMA (top). Day 1 and Day 7. **b)** Cell number counting along the gradient samples Day 1 and Day 7. Scale bar: a) 1mm.

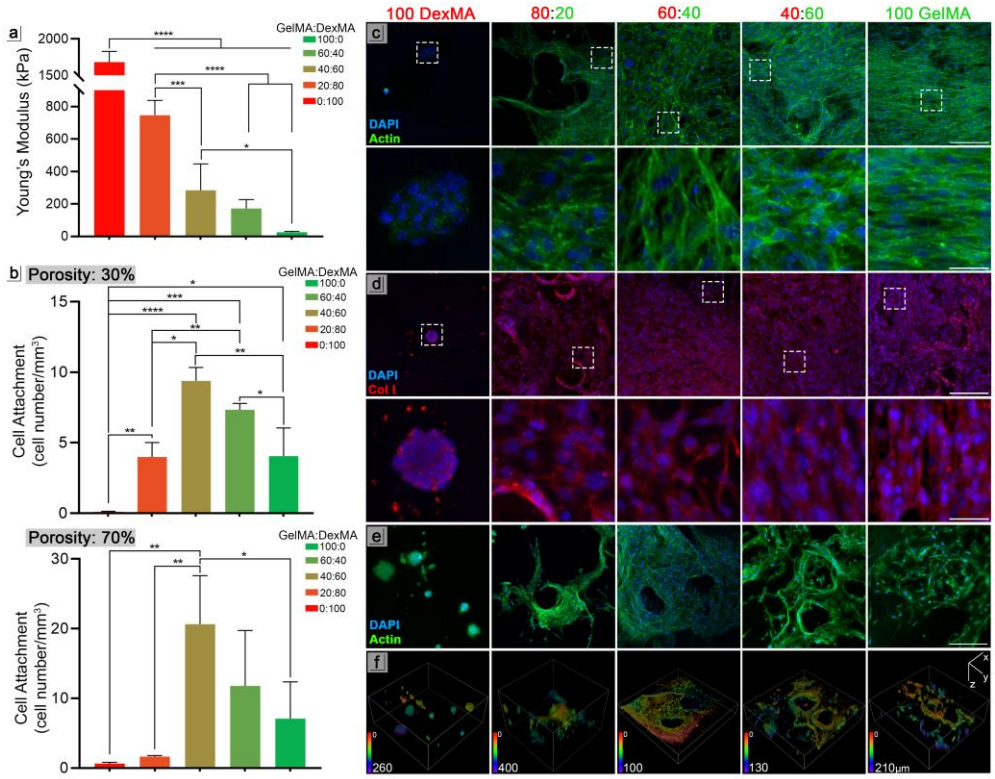

Figure 4.8 3T3-fibroblast cell adherence study on GelMA:DexMA scaffold. **a)** Morphological characterization of 3D printed porous FGHs: Variation of Young's moduli in samples characterized by DexMA – GelMA single and bi-composition. **b)** Cell attachment analysis on scaffolds on Day 7. Confocal laser microscopy images: **c)** Actin (green) and DAPI (blue) staining of 3T3-fibroblast on different scaffolds (30% porosity) on day 7. **d)** Collagen type I (red) and DAPI (blue) staining of 3T3-fibroblasts on different scaffolds (30% porosity) on day 7. **e)** The line shows Actin (green) and DAPI (blue) staining of 3T3-fibroblast on different scaffolds (70% porosity) on day 7. **f)** Z-stack imaging showing the depth-wise distribution of cells within the 3D scaffold. Scale bars c-d) 200 µm and 40 µm, e) 200 µm. Statistical significances were assessed by one-way ANOVA. Mean ± S.D. n=3, *p < 0.05, **p < 0.01, ***p < 0.001, ****p < 0.0001.

4.4. Conclusions

In this work, we developed and validated a microfluidic-assisted 3D printing platform, integrating a passive mix-ff-MPH, for the fabrication of pFGHs. The proposed architecture enables independent yet simultaneous control over two

critical scaffold parameters: matrix chemical composition and internal pore architecture.

Optimization of the micromixer geometry resulted in efficient blending of polymeric solutions, achieving a MI ≥ 0.8 across all tested compositional ratios. The integration of the mixing unit upstream of the flow-focusing junction allowed real-time modulation of the continuous-phase composition, while regulation of the dispersed-phase volume fraction enabled precise adjustment of scaffold porosity. This combined strategy transformed gradient fabrication into a dynamically programmable manufacturing process. The synchronization between microfluidic flow control and extrusion-based deposition permitted the fabrication of three-dimensional constructs with spatially defined variations in composition and density. Structural analyses, including FTIR and microCT, confirmed the presence of smooth compositional gradients and well-defined spherical porous architecture throughout the scaffold volume. Importantly, both 2-layer and continuous gradients can be generated within the same fabrication framework, demonstrating the system's versatility. Preliminary biological validation using 3T3 fibroblasts highlighted the functional relevance of the generated gradients. Regions enriched in GelMA promoted cell adhesion, spreading, and collagen type I deposition, whereas DexMA-dominant areas exhibited reduced cell–matrix interaction. The graded scaffolds enabled observation of cellular behavior across a continuous spectrum of mechanical and biochemical cues within a single construct, underscoring their potential as platforms for microenvironmental screening. Overall, the mix-ff-MPH represents a flexible and scalable tool for the manufacturing of multi-material porous hydrogels with programmable spatial properties. The ability to modulate composition

and porosity in a synchronized and controlled manner opens new opportunities for engineering complex tissue interfaces, such as the bone–cartilage interface.

Future developments may extend this approach to multicellular systems, incorporate bioactive molecules, or integrate it into perfused culture platforms. Moreover, further exploration of the combined influence of material gradients, pore architecture, and geometric features on cellular behavior may provide deeper insight into the design of next-generation biofabricated constructs.

Chapter 5 – Conclusions

This doctoral thesis investigated advanced manufacturing strategies for the fabrication of porous and graded biomaterial scaffolds through the integration of microfluidics and additive manufacturing. The central objective of this work was to establish a versatile technological platform capable of controlling pore architecture, material composition, and spatial distribution of structural features with high precision. Such control is essential for engineering materials that replicate the structural complexity of biological tissues and for producing scaffolds with tunable mechanical and physicochemical properties.

The first results of this work focused on the development of a microfluidic-assisted printing strategy for the controlled fabrication of porous materials. By integrating droplet microfluidics with extrusion-based 3D printing, it became possible to achieve deterministic control over pore formation directly during the manufacturing process. The flow-focusing microfluidic device enabled the generation of highly monodisperse droplets whose diameter could be precisely tuned by adjusting the flow rate ratio between the dispersed and continuous phases. When combined with extrusion-based printing within a support bath, this approach allowed the deposition of emulsion-based inks while preserving droplet integrity during the printing process. As a result, porous hydrogel scaffolds with highly uniform pore distributions and tunable porosity were successfully fabricated, with droplet-templated spherical pore architectures that can be interpreted as porous metamaterials, where structural properties are governed by the designed geometry rather than solely by the base material. These results collectively demonstrate a clear methodological advancement, establishing a reproducible and programmable printing framework that overcomes the inherent stochasticity of conventional porogenic techniques.

Building upon this strategy, the microfluidic printing approach was further extended to the fabrication of ceramic scaffolds for bone tissue engineering. In this case, emulsion-templated hydrogel constructs served as sacrificial templates that were subsequently converted into fully ceramic structures through thermal debinding and sintering. The results demonstrated that the printed droplet-templated spherical pore architecture could be successfully preserved during the thermal processing steps despite substantial volumetric shrinkage. MicroCT analysis confirmed homogeneous densification and isotropic shrinkage, indicating that the structural integrity of the scaffolds was maintained throughout processing. Preliminary biological evaluation using hMSC further confirmed that the fabricated ceramic scaffolds supported cell viability and metabolic activity. This extension to ceramic systems highlights the robustness and versatility of the proposed platform, demonstrating its applicability to load-bearing biomaterials and reinforcing its potential relevance for translational bone tissue engineering.

Further expanding the capabilities of the microfluidic printing platform, a custom microfluidic micromixer was developed to enable the controlled generation of compositional gradients during printing. The integration of this passive mixing element upstream of the droplet generation region allowed precise regulation of the composition of the continuous phase while maintaining stable droplet formation. By dynamically modulating the composition of the matrix during deposition, this system enabled the fabrication of functionally graded materials in which both spherical pore architecture and matrix composition could be spatially varied across the printed scaffold. This advancement represents a significant step toward the fabrication of biomaterials that more closely reproduce the hierarchical and gradient-based organization of native interface tissues, such as the osteochondral interface.

While the primary focus of this thesis was on the development and validation of the manufacturing platform, the resulting materials also show strong potential for future applications in tissue engineering and regenerative medicine. In particular, the ability to fabricate porous and functionally graded structures may enable the engineering of biomaterials that more closely mimic the structural organization of complex tissues such as the osteochondral interface.

Future work should therefore focus on expanding the material palette compatible with the microfluidic printing platform, improving the scalability of the process, and investigating the biological performance of the fabricated scaffolds *in vitro* and *in vivo*. Additional studies include the integration of bioactive molecules, cell-laden bioinks, and multi-material printing strategies to further enhance the functional potential of the system.

In conclusion, this doctoral thesis demonstrates that integrating microfluidics with additive manufacturing provides a powerful framework for the direct designing of material architecture, thus enabling the deterministic fabrication of porous and graded meta-biomaterials with controllable spherical pore architectures. By transitioning from stochastic to fully programmable pore formation, this work establishes a new paradigm for the design of complex porous biomaterials with predictable structure-function relationships, ultimately transforming the way such materials are conceived and fabricated for biomedical applications.

References

1. Liu, P. & Chen, G.-F. *Porous Materials: Processing and Applications*. (Elsevier Butterworth-Heinemann, Amsterdam Boston Paris, 2014).

2. Zhao, N. *et al.* Bioinspired Materials: from Low to High Dimensional Structure. *Advanced Materials* **26**, 6994–7017 (2014).

3. Li, S. *et al.* Advances in hierarchically porous materials: Fundamentals, preparation and applications. *Renewable and Sustainable Energy Reviews* **202**, 114641 (2024).

4. Wei, R. *et al.* Advances in porous materials for efficient separation and purification of flue gas. *Separation and Purification Technology* **352**, 128238 (2025).

5. Wegst, U. G. K., Bai, H., Saiz, E., Tomsia, A. P. & Ritchie, R. O. Bioinspired structural materials. *Nature Mater* **14**, 23–36 (2015).

6. Li, Y. *et al.* A Review on Functionally Graded Materials and Structures via Additive Manufacturing: From Multi-Scale Design to Versatile Functional Properties. *Adv Materials Technologies* **5**, 1900981 (2020).

7. Rho, J.-Y., Kuhn-Spearing, L. & Zioupos, P. Mechanical properties and the hierarchical structure of bone. *Med. Eng. Phys.* **20**, 92–102 (1998).

8. Deng, W., Kumar, S., Vallone, A., Kochmann, D. M. & Greer, J. R. AI-Enabled Materials Design of Non-Periodic 3D Architectures With Predictable Direction-Dependent Elastic Properties. *Advanced Materials* **36**, 2308149 (2024).

9. Fratzl, P. & Weinkamer, R. Nature's hierarchical materials. *Progress in Materials Science* **52**, 1263–1334 (2007).

10. Miyamoto, Y., Kaysser, W. A., Rabin, B. H., Kawasaki, A. & Ford, R. G. Processing and Fabrication. in *Functionally Graded Materials* (eds Miyamoto, Y., Kaysser, W. A., Rabin, B. H., Kawasaki, A. & Ford, R. G.) vol. 5 161–245 (Springer US, Boston, MA, 1999).

11. *Functionally Graded Materials: Design, Processing, and Applications*. (Kluwer Academic Publishers, Boston, 1999).

12. Bohidar, S. K., Sharma, R. & Mishra, P. R. Functionally Graded Materials: A Critical Review. **1**, (2014).

13. Mahamood, R. M. & Akinlabi, E. T. *Functionally Graded Materials*. (Springer International Publishing, Cham, 2017). doi:10.1007/978-3-319-53756-6.

14. Pasha, A. & Rajaprakash, B. M. Fabrication and mechanical properties of functionally graded materials: A review. *Materials Today: Proceedings* **52**, 379–387 (2022).

15. Zhang, C. *et al.* Additive manufacturing of functionally graded materials: A review. *Materials Science and Engineering: A* **764**, 138209 (2019).

16. Hao, M. *et al.* Functionally Graded Surfaces and Materials: From Fabrication to Biomedical Applications. *Chem. Rev.* **126**, 2143–2196 (2026).

17. Liu, J. *et al.* 3D printing of biomimetic multi-layered GelMA/nHA scaffold for osteochondral defect repair. *Materials & Design* **171**, 107708 (2019).

18. Costantini, M. *et al.* 3D-Printing of Functionally Graded Porous Materials Using On-Demand Reconfigurable Microfluidics. *Angew Chem Int Ed* **58**, 7620–7625 (2019).

19. Chen, D., Gao, K., Yang, J. & Kitipornchai, S. An introduction to functionally graded porous materials and composite structures. in *Machine Learning Aided Analysis, Design, and Additive Manufacturing of Functionally Graded Porous Composite Structures* 3–15 (Elsevier, 2024). doi:10.1016/B978-0-443-15425-6.00001-8.

20. Oliveira, J. M., Ribeiro, V. P. & Reis, R. L. Advances on gradient scaffolds for osteochondral tissue engineering. *Prog. Biomed. Eng.* **3**, 033001 (2021).

21. Pompe, W. *et al.* Functionally graded materials for biomedical applications. *Materials Science and Engineering: A* **362**, 40–60 (2003).

22. Kieback, B., Neubrand, A. & Riedel, H. Processing techniques for functionally graded materials. *Materials Science and Engineering: A* **362**, 81–106 (2003).

23. Pradeep, A. D. & Rameshkumar, T. Review on centrifugal casting of functionally graded materials. *Materials Today: Proceedings* **45**, 729–734 (2021).

24. Dudina, D. V., Bokhonov, B. B. & Olevsky, E. A. Fabrication of Porous Materials by Spark Plasma Sintering: A Review. *Materials* **12**, 541 (2019).

25. Saleh, B. *et al.* 30 Years of functionally graded materials: An overview of manufacturing methods, Applications and Future Challenges. *Composites Part B: Engineering* **201**, 108376 (2020).

26. Hubbell, J. A. Biomaterials in Tissue Engineering. *Nat Biotechnol* **13**, 565–576 (1995).

27. Stubenrauch, C., Menner, A., Bismarck, A. & Drenckhan, W. Emulsion and Foam Templating—Promising Routes to Tailor-Made Porous Polymers. *Angew Chem Int Ed* **57**, 10024–10032 (2018).

28. Kimmins, S. D. & Cameron, N. R. Functional Porous Polymers by Emulsion Templating: Recent Advances. *Adv Funct Materials* **21**, 211–225 (2011).

29. Zhang, H. & Cooper, A. I. Synthesis and applications of emulsion-templated porous materials. *Soft Matter* **1**, 107 (2005).

30. Barbetta, A., Dentini, M., Zannoni, E. M. & De Stefano, M. E. Tailoring the Porosity and Morphology of Gelatin-Methacrylate PolyHIPE Scaffolds for Tissue Engineering Applications. *Langmuir* **21**, 12333–12341 (2005).

31. Nam, Y. S., Yoon, J. J. & Park, T. G. A novel fabrication method of macroporous biodegradable polymer scaffolds using gas foaming salt as a porogen additive. *J. Biomed. Mater. Res.* **53**, 1–7 (2000).

32. Bibette, J., Calderon, F. L. & Poulin, P. Emulsions: basic principles. *Rep. Prog. Phys.* **62**, 969–1033 (1999).

33. Chu, L., Utada, A. S., Shah, R. K., Kim, J. & Weitz, D. A. Controllable Monodisperse Multiple Emulsions. *Angew Chem Int Ed* **46**, 8970–8974 (2007).

34. Loh, Q. L. & Choong, C. Three-Dimensional Scaffolds for Tissue Engineering Applications: Role of Porosity and Pore Size. *Tissue Engineering Part B: Reviews* **19**, 485–502 (2013).

35. Colosi, C. *et al.* Morphological Comparison of PVA Scaffolds Obtained by Gas Foaming and Microfluidic Foaming Techniques. *Langmuir* **29**, 82–91 (2013).

36. Whitesides, G. M. The origins and the future of microfluidics. *Nature* **442**, 368–373 (2006).

37. Cai, G., Xue, L., Zhang, H. & Lin, J. A Review on Micromixers. *Micromachines* **8**, 274 (2017).

38. Oevreeide, I. H., Zoellner, A., Mielnik, M. M. & Stokke, B. T. Curved passive mixing structures: a robust design to obtain efficient mixing and mass transfer in microfluidic channels. *J. Micromech. Microeng.* **31**, 015006 (2021).

39. Wang, X., Liu, Z., Wang, B., Cai, Y. & Song, Q. An overview on state-of-art of micromixer designs, characteristics and applications. *Analytica Chimica Acta* **1279**, 341685 (2023).

40. Garstecki, P. Formation of Droplets and Bubbles in Microfluidic Systems. in *Microfluidics Based Microsystems* (eds Kakaç, S., Kosoy, B., Li, D. & Pramuanjaroenkij, A.) 163–181 (Springer Netherlands, Dordrecht, 2010). doi:10.1007/978-90-481-9029-4_9.

41. Garstecki, P., Fuerstman, M. J., Stone, H. A. & Whitesides, G. M. Formation of droplets and bubbles in a microfluidic T-junction—scaling and mechanism of break-up. *Lab Chip* **6**, 437 (2006).

42. Anna, S. L. & Mayer, H. C. Microscale tipstreaming in a microfluidic flow focusing device. *Physics of Fluids* **18**, 121512 (2006).

43. Dewandre, A., Rivero-Rodriguez, J., Vitry, Y., Sobac, B. & Scheid, B. Microfluidic droplet generation based on non-embedded co-flow-focusing using 3D printed nozzle. *Sci Rep* **10**, 21616 (2020).

44. Christopher, G. F. & Anna, S. L. Microfluidic methods for generating continuous droplet streams. *J. Phys. D: Appl. Phys.* **40**, R319–R336 (2007).

45. Hales, T. C. *Dense Sphere Packings: A Blueprint for Formal Proofs*. (Cambridge University Press, Cambridge ; New York, 2012).

46. Christopher, G. F. *et al.* Coalescence and splitting of confined droplets at microfluidic junctions. *Lab Chip* **9**, 1102 (2009).

47. Costantini, M. *et al.* Highly ordered and tunable polyHIPEs by using microfluidics. *J. Mater. Chem. B* **2**, 2290 (2014).

48. Nalin, F., Tirelli, M. C., Garstecki, P., Postek, W. & Costantini, M. Tuna-step: tunable parallelized step emulsification for the generation of

droplets with dynamic volume control to 3D print functionally graded porous materials. *Lab Chip* 10.1039.D3LC00658A (2024) doi:10.1039/D3LC00658A.

49. Otsubo, Y. & Prud'Homme, R. K. Flow Behavior of Oil-in-Water Emulsions. *Nihon Reoroji Gakkaishi(Journal of the Society of Rheology, Japan)* **20**, 125–131 (1992).

50. Aldemir Dikici, B. & Claeyssens, F. Basic Principles of Emulsion Templating and Its Use as an Emerging Manufacturing Method of Tissue Engineering Scaffolds. *Front. Bioeng. Biotechnol.* **8**, 875 (2020).

51. Loh, G. H., Pei, E., Harrison, D. & Monzón, M. D. An overview of functionally graded additive manufacturing. *Additive Manufacturing* **23**, 34–44 (2018).

52. Gibson, I., Rosen, D., Stucker, B. & Khorasani, M. *Additive Manufacturing Technologies*. (Springer International Publishing, Cham, 2021). doi:10.1007/978-3-030-56127-7.

53. Reina-Romo, E., Papantoniou, I., Bloemen, V. & Geris, L. Computational design of tissue engineering scaffolds. in *Handbook of Tissue Engineering Scaffolds: Volume One* 73–92 (Elsevier, 2019). doi:10.1016/B978-0-08-102563-5.00004-6.

54. Foroughi, A. H., Valeri, C. & Razavi, M. J. A review of computational optimization of bone scaffold architecture: methods, challenges, and perspectives. *Prog. Biomed. Eng.* **7**, 012003 (2025).

55. Groover, M. P. *Fundamentals of Modern Manufacturing: Materials, Processes, and Systems*. (John Wiley & Sons, Inc, Hoboken, NJ, 2019).

56. Li, K. *et al.* High performance realization of functionally graded materials based on integrated optimal design and additive manufacturing: A review. *International Materials Reviews* **70**, 497–547 (2025).

57. Zhang, H., Duan, M., Qin, S. & Zhang, Z. Preparation and Modification of Porous Polyetheretherketone (PEEK) Cage Material Based on Fused Deposition Modeling (FDM). *Polymers* **14**, 5403 (2022).

58. Shor, L. *et al.* Precision extruding deposition (PED) fabrication of polycaprolactone (PCL) scaffolds for bone tissue engineering. *Biofabrication* **1**, 015003 (2009).

59. Fei, G. *et al.* Stereolithographic 3D printing of graded porous materials via an integrated digital exposure and selective dissolution strategy. *Cell Reports Physical Science* **4**, 101504 (2023).

60. Yan, M., Tian, X., Peng, G., Cao, Y. & Li, D. Hierarchically porous materials prepared by selective laser sintering. *Materials & Design* **135**, 62–68 (2017).

61. Alkunte, S. *et al.* Porosity in additive manufacturing: influence on mechanical, thermal, and electrical properties—a review. *Int J Adv Manuf Technol* **140**, 2397–2421 (2025).

62. Han, D. & Lee, H. Recent advances in multi-material additive manufacturing: methods and applications. *Current Opinion in Chemical Engineering* **28**, 158–166 (2020).

63. Bernal, P. N. *et al.* The road ahead in materials and technologies for volumetric 3D printing. *Nat Rev Mater* **10**, 826–841 (2025).

64. O'Halloran, S., Pandit, A., Heise, A. & Kellett, A. Two-Photon Polymerization: Fundamentals, Materials, and Chemical Modification Strategies. *Advanced Science* **10**, 2204072 (2023).

65. Dhand, A. P., Davidson, M. D. & Burdick, J. A. Lithography-based 3D printing of hydrogels. *Nat Rev Bioeng* **3**, 108–125 (2024).

66. Placone, J. K. & Engler, A. J. Recent Advances in Extrusion-Based 3D Printing for Biomedical Applications. *Adv Healthcare Materials* **7**, 1701161 (2018).

67. Brackett, J. *et al.* The impact of infill percentage and layer height in small-scale material extrusion on porosity and tensile properties. *Additive Manufacturing* **58**, 103063 (2022).

68. Alifui-Segbaya, F., Ituarte, I. F., Hasanov, S., Gupta, A. & Fidan, I. Opportunities and Limitations of Additive Manufacturing. in *Springer Handbook of Additive Manufacturing* (eds Pei, E. et al.) 125–143 (Springer International Publishing, Cham, 2023). doi:10.1007/978-3-031-20752-5_9.

69. Pérez, M., Carou, D., Rubio, E. M. & Teti, R. Current advances in additive manufacturing. *Procedia CIRP* **88**, 439–444 (2020).

70. Faes, M. *et al.* Process Monitoring of Extrusion Based 3D Printing via Laser Scanning. https://doi.org/10.13140/2.1.5175.0081 (2014) doi:10.13140/2.1.5175.0081.

71. Joseph, A. & Uthirapathy, V. A Systematic Review of the Contribution of Additive Manufacturing toward Orthopedic Applications. *ACS Omega* **9**, 44042–44075 (2024).

72. Hinton, T. J. *et al.* Three-dimensional printing of complex biological structures by freeform reversible embedding of suspended hydrogels. *Sci. Adv.* **1**, e1500758 (2015).

73. Zhou, K., Sun, Y., Yang, J., Mao, H. & Gu, Z. Hydrogels for 3D embedded bioprinting: a focused review on bioinks and support baths. *J. Mater. Chem. B* **10**, 1897–1907 (2022).

74. Ikada, Y. Challenges in tissue engineering. *J. R. Soc. Interface.* **3**, 589–601 (2006).

75. Shen, W., Zhang, P., Li, W. & Qin, H. Additive manufacturing for functional design: a review of capabilities, strategies and applications. *Rapid Prototyping Journal* **32**, 346–372 (2026).

76. Leong, K. F., Chua, C. K., Sudarmadji, N. & Yeong, W. Y. Engineering functionally graded tissue engineering scaffolds. *Journal of the Mechanical Behavior of Biomedical Materials* **1**, 140–152 (2008).

77. Nordberg, R. C., Wen, D. H., Wang, D., Hu, J. C. & Athanasiou, K. A. Challenges and recent advances in engineering the osteochondral interface. *Current Opinion in Biomedical Engineering* **31**, 100546 (2024).

78. *Tissue Engineering*. (Academic Press, an imprint of Elsevier, London, United Kingdom ; San Diego, CA, 2023).

79. Freed, L. E., Engelmayr, G. C., Borenstein, J. T., Moutos, F. T. & Guilak, F. Advanced Material Strategies for Tissue Engineering Scaffolds. *Advanced Materials* **21**, 3410–3418 (2009).

80. Chung, S. & King, M. W. Design concepts and strategies for tissue engineering scaffolds. *Biotech and App Biochem* **58**, 423–438 (2011).

81. Ozbolat, I. T. & Hospodiuk, M. Current advances and future perspectives in extrusion-based bioprinting. *Biomaterials* **76**, 321–343 (2016).

82. Boskey, A. L. & Robey, P. G. The Composition of Bone. in *Primer on the Metabolic Bone Diseases and Disorders of Mineral Metabolism* (eds Bilezikian, J. P. et al.) 84–92 (Wiley, 2018). doi:10.1002/9781119266594.ch11.

83. Lee, S. S., Du, X., Kim, I. & Ferguson, S. J. Scaffolds for bone-tissue engineering. *Matter* **5**, 2722–2759 (2022).

84. Woll, J. E. & Smith, D. M. Bone and Connective Tissue. *Clinics in Laboratory Medicine* **25**, 499–518 (2005).

85. Xu, C. *et al.* Bone tissue engineering scaffold materials: Fundamentals, advances, and challenges. *Chinese Chemical Letters* **35**, 109197 (2024).

86. Khajehmohammadi, M., Azizi Tafti, R. & Nikukar, H. Effect of porosity on mechanical and biological properties of bioprinted scaffolds. *J Biomedical Materials Res* **111**, 245–260 (2023).

87. Takaoka, Y. *et al.* Bone ingrowth into a porous structure is achieved by preceding fibrogenesis and vascularization. *Acta Biomaterialia* **177**, 243–252 (2024).

88. Dubey, A., Jaiswal, S. & Lahiri, D. Promises of Functionally Graded Material in Bone Regeneration: Current Trends, Properties, and Challenges. *ACS Biomater. Sci. Eng.* **8**, 1001–1027 (2022).

89. Yildirim, N., Amanzhanova, A., Kulzhanova, G., Mukasheva, F. & Erisken, C. Osteochondral Interface: Regenerative Engineering and Challenges. *ACS Biomater. Sci. Eng.* **9**, 1205–1223 (2023).

90. Nordberg, R. C. *et al.* Recent advancements in cartilage tissue engineering innovation and translation. *Nat Rev Rheumatol* **20**, 323–346 (2024).

91. Sangiorgio, A. *et al.* Subchondral bone: An emerging target for the treatment of articular surface lesions of the knee. *J. exp. orthop.* **11**, e12098 (2024).

92. Cai, J., Wang, J., Sun, C., Dai, J. & Zhang, C. Biomaterials with stiffness gradient for interface tissue engineering. *Biomed. Mater.* **17**, 064103 (2022).

93. Di Luca, A., Van Blitterswijk, C. & Moroni, L. The osteochondral interface as a gradient tissue: From development to the fabrication of gradient scaffolds for regenerative medicine. *Birth Defects Research Pt C* **105**, 34–52 (2015).

94. Liu, Z., Meyers, M. A., Zhang, Z. & Ritchie, R. O. Functional gradients and heterogeneities in biological materials: Design principles, functions, and bioinspired applications. *Progress in Materials Science* **88**, 467–498 (2017).

95. Fratzl, P. & Barth, F. G. Biomaterial systems for mechanosensing and actuation. *Nature* **462**, 442–448 (2009).

96. Werner, J., Linner-Krčmar, B., Friess, W. & Greil, P. Mechanical properties and in vitro cell compatibility of hydroxyapatite ceramics with graded pore structure. *Biomaterials* **23**, 4285–4294 (2002).

97. Oh, S. H., Park, I. K., Kim, J. M. & Lee, J. H. In vitro and in vivo characteristics of PCL scaffolds with pore size gradient fabricated by a centrifugation method. *Biomaterials* **28**, 1664–1671 (2007).

98. Ren, L. *et al.* 3D printing of materials with spatially non-linearly varying properties. *Materials & Design* **156**, 470–479 (2018).

99. Bakarich, S. E. *et al.* 3D printing of tough hydrogel composites with spatially varying materials properties. *Additive Manufacturing* **14**, 24–30 (2017).

100. Qian, T. T., Liu, D., Tian, X. J., Liu, C. M. & Wang, H. M. Microstructure of TA2/TA15 graded structural material by laser additive manufacturing process. *Transactions of Nonferrous Metals Society of China (English Edition)* **24**, 2729–2736 (2014).

101. Costantini, M. *et al.* 3D bioprinting of BM-MSCs-loaded ECM biomimetic hydrogels for *in vitro* neocartilage formation. *Biofabrication* **8**, 035002 (2016).

102. Senior, J. J., Cooke, M. E., Grover, L. M. & Smith, A. M. Fabrication of Complex Hydrogel Structures Using Suspended Layer Additive Manufacturing (SLAM). *Adv Funct Materials* **29**, 1904845 (2019).

103. Jankowski, P., Ogończyk, D., Derzsi, L., Lisowski, W. & Garstecki, P. Hydrophilic polycarbonate chips for generation of oil-in-water (O/W)

and water-in-oil-in-water (W/O/W) emulsions. *Microfluid Nanofluid* **14**, 767–774 (2013).

104. Karnowski, K. *et al.* Optical coherence microscopy as a novel, non-invasive method for the 4D live imaging of early mammalian embryos. *Sci Rep* **7**, 4165 (2017).

105. Cidonio, G. *et al.* Printing bone in a gel: using nanocomposite bioink to print functionalised bone scaffolds. *Materials Today Bio* **4**, 100028 (2019).

106. Cidonio, G. *et al.* 3D printing of biphasic inks: beyond single-scale architectural control. *J. Mater. Chem. C* **9**, 12489–12508 (2021).

107. Visser, C. W., Kamperman, T., Karbaat, L. P., Lohse, D. & Karperien, M. In-air microfluidics enables rapid fabrication of emulsions, suspensions, and 3D modular (bio)materials. *Sci. Adv.* **4**, eaao1175 (2018).

108. Otsubo, Y. & Prud'homme, R. K. Flow behavior of oil-in-water emulsions. *Journal of Rheology* **37**, 561–561 (1993).

109. Barbetta, A., Massimi, M., Conti Devirgiliis, L. & Dentini, M. Enzymatic Cross-Linking versus Radical Polymerization in the Preparation of Gelatin PolyHIPEs and Their Performance as Scaffolds in the Culture of Hepatocytes. *Biomacromolecules* **7**, 3059–3068 (2006).

110. Barbetta, A. *et al.* Emulsion Templated Scaffolds that Include Gelatin and Glycosaminoglycans. *Biomacromolecules* **9**, 2844–2856 (2008).

111. De Colli, M. *et al.* A biomimetic porous hydrogel of gelatin and glycosaminoglycans cross-linked with transglutaminase and its application in the culture of hepatocytes. *Biomed. Mater.* **7**, 055005 (2012).

112. Idaszek, J. *et al.* 3D bioprinting of hydrogel constructs with cell and material gradients for the regeneration of full-thickness chondral defect using a microfluidic printing head. *Biofabrication* **11**, 044101 (2019).

113. Zhang, K., Oldenhof, S., Wang, Y., Van Esch, J. H. & Mendes, E. Spatial Manipulation and Integration of Supramolecular Filaments on Hydrogel Substrates towards Advanced Soft Devices. *Angew Chem Int Ed* **59**, 8601–8607 (2020).

114. Wang, H. *et al.* Cell-laden photocrosslinked GelMA–DexMA copolymer hydrogels with tunable mechanical properties for tissue engineering. *J Mater Sci: Mater Med* **25**, 2173–2183 (2014).

115. Jin, Y., Compaan, A., Chai, W. & Huang, Y. Functional Nanoclay Suspension for Printing-Then-Solidification of Liquid Materials. *ACS Appl. Mater. Interfaces* **9**, 20057–20066 (2017).

116. Bjerregaard, S., Söderberg, I., Vermehren, C. & Frokjaer, S. Formulation and evaluation of release and swelling mechanism of a water-in-oil emulsion using factorial design. *International Journal of Pharmaceutics* **193**, 1–11 (1999).

117. Li, C., Ouyang, L., Armstrong, J. P. K. & Stevens, M. M. Advances in the Fabrication of Biomaterials for Gradient Tissue Engineering. *Trends in Biotechnology* **39**, 150–164 (2021).

118. Choi, W. S. *et al.* Development of a Multi-Layer Skin Substitute Using Human Hair Keratinic Extract-Based Hybrid 3D Printing. *Polymers* **13**, 2584 (2021).

119. Portan, D. V. *et al.* Gradient 3D Printed PLA Scaffolds on Biomedical Titanium: Mechanical Evaluation and Biocompatibility. *Polymers* **13**, 682 (2021).

120. Chen, X. *et al.* 3D printed porous PLA/nHA composite scaffolds with enhanced osteogenesis and osteoconductivity *in vivo* for bone regeneration. *Biomed. Mater.* **14**, 065003 (2019).

121. Xue, N. *et al.* Bone Tissue Engineering in the Treatment of Bone Defects. *Pharmaceuticals* **15**, 879 (2022).

122. Emami, I., Hassanzadeh Nemati, N. & Bahrami, N. Fabrication and Characterization of 3D Collagen/ Polycaprolactone/ Hydroxyapatite Nanoparticles Scaffold Using 3D Printing Method for Repairing Damaged Bone Tissue. *IJE* **38**, 2405–2413 (2025).

123. Boskey, A. L. & Robey, P. G. The Composition of Bone. in *Primer on the Metabolic Bone Diseases and Disorders of Mineral Metabolism* (ed. Rosen, C. J.) 49–58 (Wiley, 2013). doi:10.1002/9781118453926.ch6.

124. Rodriguez-Palomo, A., Østergaard, M. & Birkedal, H. Bone Hierarchical Structure: Heterogeneity and Uniformity. *Adv Funct Materials* **34**, 2307026 (2024).

125. Bal, Z., Kaito, T., Korkusuz, F. & Yoshikawa, H. Bone regeneration with hydroxyapatite-based biomaterials. *emergent mater.* **3**, 521–544 (2020).

126. Hashimoto, K. *et al.* Fabricating ordered porous β-tricalcium phosphate ceramics having specific structure via the replica method using 3D-CAD-designed polymeric templates. *Open Ceramics* **25**, 100928 (2026).

127. Resmi, V. G. *et al.* Processing of Porous SiC by Aluminum-Derived Binders and Sacrificial Porogen Leaching Method. *Int J Applied Ceramic Tech* **12**, 967–975 (2015).

128. Naebe, M. & Shirvanimoghaddam, K. Functionally graded materials: A review of fabrication and properties. *Applied Materials Today* **5**, 223–245 (2016).

129. Dadkhah, M., Tulliani, J.-M., Saboori, A. & Iuliano, L. Additive manufacturing of ceramics: Advances, challenges, and outlook. *Journal of the European Ceramic Society* **43**, 6635–6664 (2023).

130. Lewis, J. A. Direct Ink Writing of 3D Functional Materials. *Adv Funct Materials* **16**, 2193–2204 (2006).

131. Lamnini, S. *et al.* Robocasting of advanced ceramics: ink optimization and protocol to predict the printing parameters - A review. *Heliyon* **8**, e10651 (2022).

132. Travitzky, N. *et al.* Additive Manufacturing of Ceramic-Based Materials. *Adv Eng Mater* **16**, 729–754 (2014).

133. Zocca, A., Colombo, P., Gomes, C. M. & Günster, J. Additive Manufacturing of Ceramics: Issues, Potentialities, and Opportunities. *J. Am. Ceram. Soc.* **98**, 1983–2001 (2015).

134. Serpe, F. *et al.* Microfluidic 3D Bioprinting of Foamed Fibers with Controlled Micromorphology. *ACS Appl. Mater. Interfaces* acsami.4c22450 (2025) doi:10.1021/acsami.4c22450.

135. Ouyang, L. Pushing the rheological and mechanical boundaries of extrusion-based 3D bioprinting. *Trends in Biotechnology* **40**, 891–902 (2022).

136. Van Hoorick, J. *et al.* Cross-Linkable Gelatins with Superior Mechanical Properties Through Carboxylic Acid Modification: Increasing the Two-Photon Polymerization Potential. *Biomacromolecules* **18**, 3260–3272 (2017).

137. Costantini, M. *et al.* Microfluidic Foaming: A Powerful Tool for Tailoring the Morphological and Permeability Properties of *Sponge-like* Biopolymeric Scaffolds. *ACS Appl. Mater. Interfaces* **7**, 23660–23671 (2015).

138. Baroud, C. N., Gallaire, F. & Dangla, R. Dynamics of microfluidic droplets. *Lab Chip* **10**, 2032 (2010).

139. Squires, T. M. & Quake, S. R. Microfluidics: Fluid physics at the nanoliter scale. *Rev. Mod. Phys.* **77**, 977–1026 (2005).

140. Silverstein, M. S. PolyHIPEs: Recent advances in emulsion-templated porous polymers. *Progress in Polymer Science* **39**, 199–234 (2014).

141. Garstecki, P., Stone, H. A. & Whitesides, G. M. Mechanism for Flow-Rate Controlled Breakup in Confined Geometries: A Route to Monodisperse Emulsions. *Phys. Rev. Lett.* **94**, 164501 (2005).

142. Sadasivan, S., Pradeep, S., Ramachandran, J. C., Narayan, J. & Gęca, M. J. Advances in droplet microfluidics: a comprehensive review of innovations, morphology, dynamics, and applications. *Microfluid Nanofluid* **29**, 17 (2025).

143. Saadi, M. A. S. R. *et al.* Direct Ink Writing: A 3D Printing Technology for Diverse Materials. *Advanced Materials* **34**, 2108855 (2022).

144. German, R. M. *Sintering Theory and Practice*. (Wiley, New York, 1996).

145. Muralithran, G. & Ramesh, S. The effects of sintering temperature on the properties of hydroxyapatite. *Ceramics International* **26**, 221–230 (2000).

146. Ritchie, R. O. The conflicts between strength and toughness. *Nature Mater* **10**, 817–822 (2011).

147. Guo, W. *et al.* Direct ink writing of functionally graded bone scaffolds using ceramic foams to mimic natural bone hierarchical porosity and multiple gradients. *Composites Part B: Engineering* **300**, 112465 (2025).

148. Dellinger, J. G., Wojtowicz, A. M. & Jamison, R. D. Effects of degradation and porosity on the load bearing properties of model hydroxyapatite bone scaffolds. *J Biomedical Materials Res* **77A**, 563–571 (2006).

149. Ren, J. *et al.* Human bone marrow stromal cell confluence: effects on cell characteristics and methods of assessment. *Cytotherapy* **17**, 897–911 (2015).

150. Seidi, A., Ramalingam, M., Elloumi-Hannachi, I., Ostrovidov, S. & Khademhosseini, A. Gradient biomaterials for soft-to-hard interface tissue engineering. *Acta Biomaterialia* **7**, 1441–1451 (2011).

151. Jalandhra, G. K. & Kilian, K. A. Biofabrication approaches to fabricating gradients and interfaces in osteochondral tissue engineering. *Current Opinion in Biomedical Engineering* **31**, 100544 (2024).

152. Sartori, M. *et al.* A new bi-layered scaffold for osteochondral tissue regeneration: In vitro and in vivo preclinical investigations. *Materials Science and Engineering: C* **70**, 101–111 (2017).

153. Levingstone, T. J. *et al.* Multi-layered collagen-based scaffolds for osteochondral defect repair in rabbits. *Acta Biomaterialia* **32**, 149–160 (2016).

154. Prasad, A., Sankar, M. R. & Katiyar, V. State of Art on Solvent Casting Particulate Leaching Method for Orthopedic ScaffoldsFabrication. *Materials Today: Proceedings* **4**, 898–907 (2017).

155. Wang, S., Zhao, S., Yu, J., Gu, Z. & Zhang, Y. Advances in Translational 3D Printing for Cartilage, Bone, and Osteochondral Tissue Engineering. *Small* **18**, 2201869 (2022).

156. Marcotulli, M. *et al.* Microfluidic 3D Printing of Emulsion Ink for Engineering Porous Functionally Graded Materials. *Adv Materials Technologies* **8**, 2201244 (2023).

157. Dai, Q. *et al.* Microfluidic bubble-templating 3D printing of ordered macroporous hydrogels. *Composites Part B: Engineering* **284**, 111725 (2024).

158. Lamberger, Z., Zainuddin, S., Scheibel, T. & Lang, G. Polymeric Janus Fibers. *ChemPlusChem* **88**, e202200371 (2023).

159. J Biomedical Materials Res - 2024 - Nedrelow - Osteochondral Regeneration With Anatomical Scaffold 3D-Printing Design.pdf.

160. Colosi, C. *et al.* Microfluidic Bioprinting of Heterogeneous 3D Tissue Constructs Using Low-Viscosity Bioink. *Advanced Materials* **28**, 677–684 (2016).

161. Feng, X. *et al.* Tri-fluid mixing in a microchannel for nanoparticle synthesis. *Lab Chip* **19**, 2936–2946 (2019).

162. Santana, H. S., Tortola, D. S., Silva, J. L. & Taranto, O. P. Biodiesel synthesis in micromixer with static elements. *Energy Conversion and Management* **141**, 28–39 (2017).

163. Young, A. T., White, O. C. & Daniele, M. A. Rheological Properties of Coordinated Physical Gelation and Chemical Crosslinking in Gelatin Methacryloyl (GelMA) Hydrogels. *Macromolecular Bioscience* **20**, (2020).

164. Raza, W., Hossain, S. & Kim, K.-Y. A Review of Passive Micromixers with a Comparative Analysis. *Micromachines* **11**, 455 (2020).

165. Yue, K. *et al.* Synthesis, properties, and biomedical applications of gelatin methacryloyl (GelMA) hydrogels. *Biomaterials* **73**, 254–271 (2015).

166. Trapani, G., Weiß, M. S. & Trappmann, B. Tunable Synthetic Hydrogels to Study Angiogenic Sprouting. *Current Protocols* **3**, e859 (2023).